UNIVERSITY OF CALIFORNIA, IRVINE

Imaging Photodissociation: Molecules, Ions, and Clusters

DISSERTATION

submitted in partial satisfaction of the requirements for the degree of

DOCTOR OF PHILOSOPHY
in Chemistry

by

Kara Marie Kapnas

Dissertation Committee
Associate Professor Craig Murray, Chair
Professor Filipp Furche
Professor Sergey Nizkorodov

2019

DEDICATION

To

my parents and sister

"Little science takes you away from God but more of it takes you to Him."

–Louis Pasteur

TABLE OF CONTENTS

LIST OF FIGURES

LIST OF TABLES

ACKNOWLEDGEMENTS

There are many people to whom I owe a great deal of gratitude for all their help and support over the last five years.

My parents and sister for all their love and support. Mom, I owe you far more than I could ever write down. I hope I have made you all proud.

My advisor, Professor Craig Murray, for giving me the opportunity to work with you first as an undergraduate and then as a graduate student, for sharing your expansive knowledge and expertise, for always being there to talk to, for many laughs and interesting conversations, and most importantly, for putting up with my shenanigans. I am truly grateful for your mentorship.

Dr. Mickey Laux, for pushing me to reach my full potential, for being a constant mentor and friend, and for believing in me when I doubted my abilities. I can say I wouldn't have been a scientist if it weren't for your inspiring teaching and coaching.

Allison, Vero, Lisa, and Annie, for keeping me sane (most of the time), for providing me with constant laughs during lunch, and for being a never ending source of encouragement.

Professor Sergey Nizkorodov, for first encouraging me to pursue my Ph.D. and for always letting me borrow spare parts from your lab when things would inexplicably stop working. Your support throughout this long journey has been unmeasurable.

And last but not least, my beloved dog Dude, for always greeting me with a wagging tail and being my constant companion.

CURRICULUM VITAE

EDUCATION

University of California, Irvine
Ph.D. in Physical Chemistry 2014 – 2019

University of California, Irvine
Bachelor of Science, Chemistry 2012 – 2014
GPA: 3.82
Honors: *Magna Cum Laude*, Phi Lambda Upsilon Chemistry Honor Society

Orange Coast College
Associate of Arts, Liberal Arts 2009 – 2012
GPA: 3.88

RESEARCH EXPERIENCE

Department of Chemistry – University of California, Irvine
Graduate Researcher – Principal Adviser: Craig Murray 2014 – 2019
Applied velocity map ion imaging to study the gas-phase photodissociation dynamics of small molecules.
Studied the spectroscopy and reaction kinetics of CH_2OO using broadband transient absorption spectroscopy and ab initio calculations.

Department of Chemistry – University of California, Irvine
Undergraduate Researcher – Craig Murray Research Group 2013 – 2014
Constructed an LED-based broadband transient-absorption spectrometer used to study the spectroscopic properties of gas-phase molecules.

TEACHING EXPERIENCE

Department of Chemistry – University of California, Irvine
Graduate Teaching Assistant

AirUCI Summer Teacher Workshop	June 2014
Analytical Chemistry Laboratory M3LC	Fall 2014
General Chemistry Lecture 1B	Winter 2015, Winter 2016, Winter 2017
General Chemistry Laboratory 1LC, 1LD	Spring 2015, Summer 2016
Preparatory General Chemistry Lecture 1P	Fall 2015
Physical Chemistry Laboratory 153	Spring 2016

Fundamentals of Quantum Mechanics 231A Fall 2017

Orange Coast College, Costa Mesa, CA
Undergraduate Teaching Assistant
First Semester General Chemistry laboratory Fall 2011, Spring 2012, Spring 2013
Second Semester General Chemistry laboratory Fall 2012

AWARDS

UCI Regents' Dissertation Fellowship 2019
Outstanding Contributions to the Department of Chemistry – Continuing TA Award 2018
American Institute Chemistry Graduate Award Recipient 2016
NSF GRFP Honorable Mention Recipient 2015

PUBLICATIONS

Kapnas, K. M. and Murray, C. "Mode specific vibrational predissociation dynamics of $(HCl)_2$ via the first overtones of the donor and acceptor stretches." (in preparation).

Kapnas, K. M. and Murray, C. "Two-photon dissociation of SO_2 via the $\tilde{C}^1B_2$ state." (in preparation).

Kapnas, K. M., McCaslin, L., and Murray, C. "Photofragmentation dynamics of acetaldehyde cations prepared by single photon VUV ionization." *Phys. Chem. Chem. Phys.* (2019) doi: 10.1039/c8cp06640j

Kapnas, K. M., Toulson, B., Foreman, E. S., Block, S., Grant, J. G., and Murray, C. "UV Photodissociation dynamics of CHI_2Cl and its role as a photolytic precursor for chlorinated Criegee intermediates." *Phys. Chem. Chem. Phys.* **19** 31039 (2017) **"Hot Article"**

Toulson, B., **Kapnas, K. M.**, Fishman, D., and Murray, C. "Competing Pathways in the Near-UV Photochemistry of Acetaldehyde." *Phys. Chem. Chem. Phys.* **19** 14276 (2017) **"Hot Article"**

Foreman, E. S., **Kapnas, K. M.**, and Murray, C. **"**Reactions between Criegee Intermediates and the Inorganic Acids HCl and HNO_3: Kinetics and Atmospheric Implications." *Angew. Chem. Int. Ed.* **55** 10419 (2016) **"Hot Paper"**

Kalinowski, J., Foreman, E. S., **Kapnas, K. M.**, Räsänen, M., Gerber, R. B., and Murray, C. "Dynamics and spectroscopy of CH_2OO Excited Electronic States." *Phys. Chem. Chem. Phys.* **18** 10941 (2015)

Foreman, E. S., **Kapnas, K. M.**, Jou, Y., Kalinowski, J., Feng, D., Gerber, R. B., and Murray, C. "Spectroscopic Studies of the $\tilde{B}^1A'$–$\tilde{X}^1A'$ Transition of the CH_2OO Biradical." *Phys. Chem. Chem. Phys.* **17** 32539 (2015)

POSTER PRESENTATIONS

Kapnas, K. M. and Murray, C. "Photofragmentation Dynamics of Cold Acetaldehyde Cations Prepared by Single Photon VUV Ionization," Gordon Research Conference and Seminar: 2018 Molecular Interactions and Dynamics, Easton, MA (2018)

Kapnas, K. M., Toulson, B., Foreman, E. S., and Murray, C. "Photodissociation Dynamics of $CHClI_2$: A Photolytic Precursor for Chlorinated Criegee Intermediates," 64th Pacific Conference on Spectroscopy and Dynamics, Pacific Grove, CA (2017) and the 33rd Informal Symposium on Kinetics and Photochemical Processes in the Atmosphere, Irvine, CA (2016)

Foreman, E. S., **Kapnas, K. M.,** Feng, D., and Craig Murray "Spectroscopic Study of the Simplest Criegee Intermediate CH_2OO" 32nd Informal Symposium on Kinetics and Photochemical Processes in the Atmosphere, Northridge, CA (2015)

ORAL PRESENTATIONS

Kapnas, K. M. and Murray, C. "Photofragmentation Dynamics of Acetaldehyde Cations Prepared by Single Photon VUV Ionization," AirUCI Research Workshop, Lake Arrowhead, CA (2018)

Kapnas, K. M. and Saswata, R. "Lights, Camera, Action: Picturing Photochemistry" AirUCI Climate Symposium, Irvine, CA (2017)

ABSTRACT OF THE DISSERTATION

Imaging Photodissociation: Molecules, Cations, and Clusters

By

Kara Marie Kapnas

Doctor of Philosophy in Chemistry

University of California, Irvine, 2019

Professor Craig Murray, Chair

Velocity map ion imaging (VMI) is a powerful experimental technique used to investigate the photodissociation dynamics of molecules following the absorption of light. This technique provides details on photofragment speed and angular distributions, giving insight into complex photochemical dynamics. This thesis will focus on three distinct cases: **Chapter 2**) UV dissociation of a neutral molecule, CHI_2Cl, **Chapter 3**) UV dissociation of an ion, CH_3CHO^+, and **Chapter 4**) IR vibrational overtone predissociation of a van der Waals complex, $(HCl)_2$.

The near-UV photochemistry of CHI_2Cl has been explored over a range of wavelengths. Results show that photolysis of CHI_2Cl forms CHICl + I with the majority of available energy being partitioned into the CHICl internal degrees of freedom. Complementary high-level MRCI calculations, including spin-orbit coupling, were performed to characterize the electronically excited states, confirming that repulsive states of A″ symmetry with highly mixed singlet/triplet character are responsible for the CHI_2Cl absorption spectrum and dynamics. The reaction between the photoproduct CHICl with O_2 was also investigated using

broadband transient absorption spectroscopy, with results demonstrating the production of chlorinated formaldehyde oxide, CHClOO, also known as a chlorinated Criegee intermediate.

To produce CH_3CHO^+, single-photon vacuum ultraviolet (VUV) light was used to ionize the neutral molecule. Four major photofragments were observed following the UV dissociation of CH_3CHO^+: CH_3^+, CH_4^+, HCO^+, CH_3CO^+. Photofragment yield spectroscopy was used to determine branching fractions, with HCO^+ found to be the dominant fragment. All four photofragments are formed with distinct dynamics. The most surprising result is perhaps formation of fast-moving CH_4^+ with a distinctly anisotropic angular distribution that is indicative of prompt dissociation. CH_3^+ appears to originate from secondary fragmentation of CH_3CO^+ (triple fragmentation) at longer wavelengths, but is attenuated at higher energy as isomers of CH_3CHO^+ become energetically accessible.

Vibrational predissociation of $(HCl)_2$ following excitation of both the free (ν_1) and bound (ν_2) HCl stretches *via* the first overtone have been investigated using velocity map imaging and IR action spectroscopy. Predissociation products have been identified in high-J levels of both ν=2 and ν=1. Ion imaging measurements of the HCl predissociation product reveal a weaker HCl–HCl bond dissociation energy than previously suggested. Correlated product pair distributions indicate the dynamics are dependent on the vibrational mode excited. Excitation of the $2\nu_1$ mode results in HCl fragments formed with a wider range of J-levels populated compared to the more tightly localized rotational distribution observed following $2\nu_2$ excitation.

1 Overview of Experimental Methods

Velocity map ion imaging (VMI) has been revolutionary in the field of molecular photodissociation and reaction dynamics. It has enabled new approaches to photoelectron spectroscopy,[1–5] crossed-beam scattering,[6–12] and photodissociation experiments.[10,13–15] This technique allows for measurement of speed and angular distributions of fragments, product branching ratios, recoil anisotropy parameters, and pair-correlated energy distributions, providing extensive information about the underlying dynamics. VMI has been extensively reviewed[6,10,16–18] in the literature over the years and has most recently been summarized by A. G. Suits.[19] Application of VMI to the study of gas-phase molecular photodissociation dynamics is presented in this thesis.

This chapter is arranged as follows. A brief historical overview of the VMI technique is presented in **Section 1.1.** Next, computational and experimental techniques used in VMI image analysis are outlined in **Sections 1.3** and **1.4**, respectively, and advances in time-resolved detectors are presented in **Section 1.5**. Finally, a description of the VMI apparatus utilized in the experimental work presented in this thesis can be found in **Section 1.6.**

1.1 Historical overview of VMI

An introduction to the velocity map ion imaging technique and its evolution from the time-of-flight mass spectrometer is presented in this section.

1.1.1 Time-of-flight mass spectrometry

Simultaneous detection of molecular masses was made possible with the time-of-flight mass

spectrometer (TOF-MS), which was first introduced in the 1940s.[20] In TOF-MS, ions are initially created at a known time, t_0, and assumed to have the same starting position and initial kinetic energy. A homogeneous electric field, V, imparts a known amount of kinetic energy, qV, to the ions and the accelerated ions are then allowed to fly some distance, D, down a field free region until reaching a time-sensitive detector. The resulting time-of-flight, t_{TOF}, of an ion is given by

$$t_{\mathrm{TOF}} = D\sqrt{\frac{m}{qV}}$$

with typical flight times for fragments ranging from hundreds of nanoseconds to microseconds. This concept is illustrated in Figure 1-1(a), where an ion is formed at t_0 in region s of an electric field formed between the repeller potential V_{r} and ground electrodes. Parallel (flat) electric field lines are produced by placing wire grids over the orifices on the electrodes, which eliminate unwanted lensing effects such as curvature of the field lines at the electrode edges. A spread in the initial position and kinetic energy of the ions can occur, reducing mass resolution in this system, with early TOF-MS measurements limited to low masses of up to 20 amu. Wiley and McLaren later greatly improved the resolution of the TOF-MS by introducing a second acceleration region, shown in Figure 1-1(b), and masses of up to 300 amu were detected and resolved.[21] The electric field formed between V_{r} and the new extractor electrode V_{e}, allows ions starting closer to the repeller (further from the detector) or moving more slowing to stay in this region longer. These ions can then be accelerated more than the ions residing closer to the extractor plate and the spread in initial starting position and kinetic energy converges at some distance.[21] Focusing conditions are

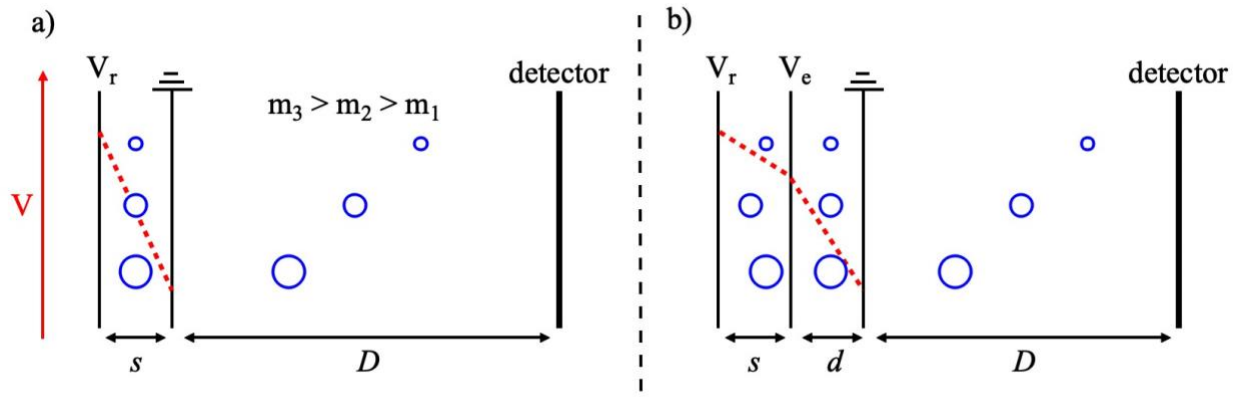

Figure 1-1 Schematic of the time-of-flight mass spectrometer. (a) One acceleration region, (b) improved Wiley-McLaren version with two acceleration regions. The red dashed lines represent the potential gradient.

mass-independent, so the entire mass spectrum can be collected in a single measurement without having to adjust the accelerating potentials, hence, avoiding any experimental drift and reducing acquisition time.

1.1.2 Ion imaging

Ion imaging was first introduced in 1987 by Chandler and Houston,[22] who combined TOF-MS with a two-dimensional (2-D) position sensitive charge detector to explore the molecular photodissociation dynamics of CH_3I. This pioneering investigation involved pulsed laser photolysis of CH_3I at 266 nm, with the resulting CH_3 photofragments state-selectively ionized using 2+1 resonance-enhanced multiphoton ionization (see Section 1.5.2.2). The authors demonstrated that the three-dimensional (3-D) spatial distribution of the nascent $CH_3(v = 0)$ photofragment velocities could be projected onto two-dimensions by accelerating the ionized fragments down a TOF tube towards a 2-D detector, comprised of a microchannel plate (MCP) coupled to a phosphor screen. As is the case for many molecular

photodissociation events, the angular distributions of the departing fragments possess cylindrical symmetry about polarization axis of the dissociating light; therefore, the 2-D detector surface was placed parallel to this symmetry axis to capture the full 3-D velocity distribution. Finally, when the ionized $CH_3(v = 0)$ fragments hit the surface of the phosphor screen, the resulting phosphorescence was recorded using a charge-coupled device (CCD) camera. Fragment recoil velocities were obtained through measurement of the image radius, which scales linearly with speed. Analysis of the $CH_3(v = 0)$ 2-D images showed that the I atom co-fragments were formed promptly and primarily in their spin-orbit excited state.

In the initial experiments, spatial resolution was limited due to the use of conventional grid extractor and repeller electrodes for ion acceleration, causing image blurring and distortion from trajectory deflections. A decade later, Eppink and Parker introduced the improved high-resolution velocity mapping variant of ion imaging and demonstrated its application in photoelectron and fragment ion imaging of O_2.[23] Open electrodes were used, which introduced curved electric field lines and allowed for complete transmission of the ions, thus eliminating any distortion. The new electrode configuration, acting as an electrostatic lens, was able to focus or "map" ions with the same velocity onto the same point on the detector, regardless of their initial spatial position. Equipotential surfaces of the ion lenses are shown in Figure 1-2 along with simulated ion trajectories reported by Eppink and Parker.[23] The photolysis and ionization lasers beams, having a finite width, propagate along the *y* direction and intersect photofragments traveling in the *x* direction (TOF path), forming ions in multiple (*x*,*y*) positions. At the focal plane, ions ejected at the same initial angle, but different starting points converge. This development led to the *velocity map imaging* spectrometer.

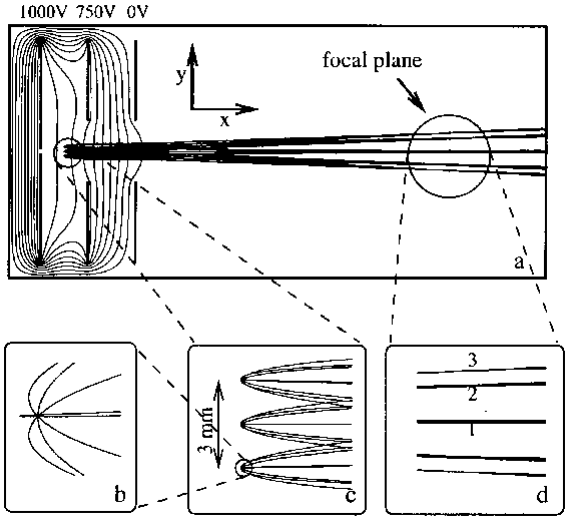

Figure 1-2 Simulated ion trajectories and equipotential surfaces for velocity mapping electrodes. Reproduced from A. Eppink and D. Parker, Rev. Sci. Instrum. 68 (9) 3477, **1997** with permission from AIP publishing. https://doi.org/10.1063/1.1148310

1.2 Ion image reconstruction methods

Each photodissociation event produces two or multiple partner fragments with equal magnitude of momentum flying in opposite directions in the center-of-mass frame. These events will occur many times over the course of an experiment as many randomly oriented molecules interact with the light. This produces a 3-D "cloud" of fragment ions known as a Newton sphere. The radius of the Newton sphere expands over time, r_t, according to

$$r_t = \sqrt{\frac{2E_0}{m}}t$$

where E_0 is the kinetic energy of the fragment of mass m at r = 0 and t = 0. The full 3-D Newton sphere is then 'pancaked' onto the 2-D detector. All velocity and angular information needed to understand the dynamics governing the dissociation event is contained in a thin

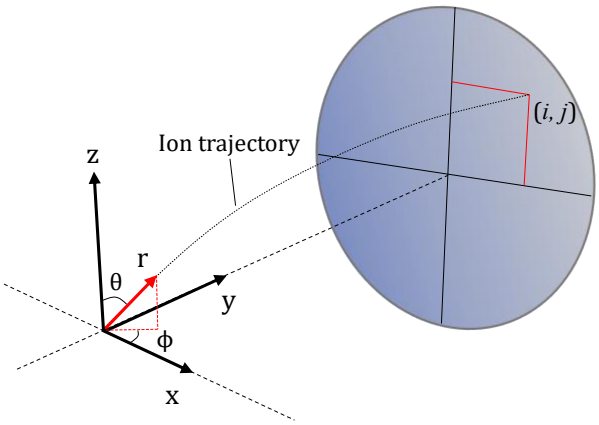

Figure 1-3 Coordinate system used for image reconstruction methods. The Newton sphere axis of symmetry lies in the *z*-direction, which is the same as the direction of the laser polarization. The angle θ is the angle between the ion velocity vector and the *z*-direction. The laser polarization dictates that the Newton sphere is symmetric with respect to rotation about the *z*-axis at an angle ϕ.

2-D slice through the center of the Newton sphere. Experiments produce the full 3-D Newton Sphere of the nascent photofragments, however, so various image reconstruction algorithms must be employed to capture the central slice of the 2-D ion image. These algorithms require that the Newton sphere possess cylindrical symmetry, which is achieved by ensuring that the laser polarization vector is parallel to the detector plane. The following subsections provide a brief overview of common image reconstruction methods that are used to extract physical information from the 2-D ion images. An illustration of the coordinate system used to describe the image reconstruction methods is shown in Figure 1-3.

1.2.1 Abel inversion

The most common approach to image reconstruction is the inverse Abel transform, a computationally fast and reliable method for recovering a slice through the symmetry axis

of the original 3-D velocity distribution.[24] Mathematically, the Abel transform of a 3-D velocity distribution, $F(z, r)$, can be calculated by the following equation:[24]

$$A(z,x) = 2\int_{x}^{\infty} F(z,r)\frac{1}{\sqrt{r^2 - x^2}}dr$$

where z is the polarization axis and $r^2 = x^2 + y^2$, the radius of the Newton sphere (refer to Figure 1-3). However, the equation of interest is the inverse of the Abel transform because what is obtained experimentally is the projection of the full ion cloud onto the 2-D detector in Cartesian coordinates. The inverse transform can be found by applying the Fourier transform convolution theorem:

$$F(z,r) = -\frac{1}{\pi}\int_{r}^{\infty} \frac{dA(z,x)}{dx}\frac{1}{\sqrt{x^2 - r^2}}dr$$

However, a solution to this equation is not trivial due to its singularity at $x = r$. A Fourier–Hankel reformulation can be used to solve the inverse Abel transform, but this method is extremely sensitive to noise present in the image and can produce false negative values in the inverted image. New approaches to image reconstruction have attempted to combat these challenges.

1.2.2 BASEX/ pBASEX

Arguably the most successful image inversion method is the polar basis set expansion Abel transform (pBASEX). Dribinski's original Cartesian BASEX algorithm reconstructs the original 3-D Newton sphere by solving the inverse Abel integral using a set of radial forward basis set functions with analytically known inverse Abel transforms.[25] Subsequently, Garcia

et al.[26] reformulated the algorithm into polar coordinates (pBASEX) using two-dimensional polar basis set functions. The pBASEX algorithm relies on fitting the kinetic energy distributions to a discrete number of Gaussian functions, with the original distribution being expressed as a linear combination

$$F(r,\theta) = \sum_{k=0}^{k=k_{\max}} \sum_{l=0}^{l=l_{\max}} c_{kl}\, e^{\frac{-(r-r_k)^2}{\sigma}} P_l(\cos\theta)$$

where θ is measured relative to the axis of cylindrical symmetry, P_l is the Legendre polynomial of order l, and r_n (the radius) is the center of the nth Gaussian center. However, Abel integrated versions of these basis functions are used to model the experimental distributions in the laboratory frame. An advantage of using polar coordinates is that the radial and angular distributions can easily be extracted from the inverted image. Furthermore, noise only accumulates at the center point, allowing for smooth high-resolution images to be obtained. The pBASEX method is somewhat computationally expensive. Most recently, Laurent and co-workers[27] greatly improved the computational speed of the pBASEX method by analyzing the 2-D projection function analytically rather than using numerically integrated functions. The new direct algorithm for the velocity map imaging system, referred to as DAVIS, is also less sensitive to noise and is well suited for image analysis in real time.

1.2.3 Onion peeling inversion

The onion peeling inversion method works by treating the photofragment velocity distribution as a series of concentric spheres, subtracting the contribution from the outer

sphere from the entire image until the center is reached. This method is attractive because it does not require a basis set selection. The inversion algorithm is based on the idea that pixel intensities in row j of the image array are comprised of contributions from ions with kinetic energies less than the maximum occurring value (E_{max}). This means that the inversion process must proceed from outside to inside along the decreasing x-direction. The outermost pixel (i_{max}, j_{max}) can only be reached by ions with E_{max} and the pixel intensity, corresponding to the number of ions contributing to the signal, can be calculated using the projection operator developed by Bordas *et al.*[28] Starting with the most energetic ion in the image, the pixel intensity is calculated and added to the back-projection slice that is being created. The back-projected slice is then subtracted from the measured projection for $i < i_{max}$ and the procedure is repeated until the center of the image is reached. This iterative algorithm "peels" back the original velocity distribution, layer by layer, until all speeds have been accounted for.

Although this method is computationally cheap, substantial error accumulation (but less than the inverse Abel transform) is introduced due to the outermost points having low signal intensity in Cartesian coordinates. To counteract this problem, onion peeling in polar coordinates was introduced.[29] Polar onion peeling (POP) can be computationally expensive but recent advancements in POP have substantially decreased the computational time by utilizing polar basis functions to fit experimental 2-D data, similar to the pBASEX method.[30]

1.3 Slice imaging

Ideally, one would obtain the narrow central slice of the ion image experimentally,

circumventing the need for computationally expensive image reconstructions methods that add/enhance image noise and require cylindrically symmetric data. An important innovation in VMI, known as time slicing, was first introduced by Gebhardt and co-workers in 2001.[31] Pulsed electric fields were used to accelerate photofragments to the detector a short time delay after dissociation and ionization, creating an enhanced spread (temporal stretching) in the arrival time of the ions compared to conventional imaging. By narrowly gating the active time of the detector, the central slice of the Newton sphere could be isolated, resulting in a sliced image equivalent to the outcome of the reconstruction methods. However, the drawback of this approach was the use of grid electrodes for uniform acceleration, which sacrificed velocity resolution.

An alternative approach to pulsed slice imaging, termed direct current (DC) slicing, has successfully achieved sufficient temporal expansion using low DC extraction fields while still preserving high-resolution velocity mapping.[7,32] Typically, a VMI setup consists of three open electrodes: repeller, extractor, and a ground electrode. With the DC slicing variant, two or more electrodes are added to the assembly. When more than three electrodes are used, the repeller and extractor regions are spread over the multi-electrode setup. Applying low voltages to the multi-electrode assembly increases the spread in arrival time to several hundred nanoseconds by extending the time the ions are influenced by the electric fields. If the spread in ion arrival time is great enough so that the gated detector (typically a 20–40 ns pulse width) captures only a narrow slice of the ion cloud (~15% or less), slicing of the image is achieved.

The speed and angular distributions can easily be extracted from the sliced image by direct

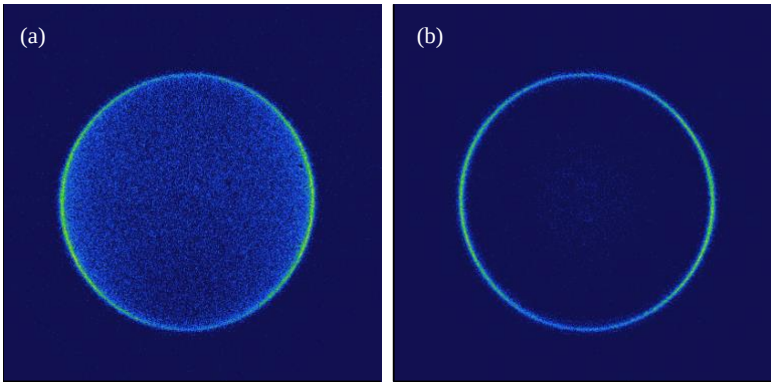

Figure 1-4 Ion images of Cl ($^2P_{3/2}$) from Cl_2 photodissociation at 355 nm. (a) Unsliced image and (b) DC sliced image.

integration. Figure 1-4 demonstrates the difference between an unsliced (a) and DC sliced (b) image of Cl ($^2P_{3/2}$) from the photodissociation of Cl_2 at 355 nm. Compressing or 'pancaking' the full Newton sphere results in a less clean center compared to DC slicing. However, DC slicing often cannot be utilized for low mass, fast moving fragments such as photoelectrons and H atoms, where there is little temporal spread and the detector can't be gated on a fast-enough time scale. Image reconstruction methods must be employed in this case to obtain the central slice.

1.4 Advances in time-resolved detectors

Advanced progress in sensor technology has led to the development of time-resolved cameras capable of simultaneous imaging of multiple fragments in a single time-of-flight spectrum.[33] This is unlike typical CCD cameras used in velocity map imaging experiments, which can only capture a single frame per time-of-flight cycle. Time-resolved cameras include the Timepix camera[34,35] and the Pixel Imaging Mass Spectrometer (PImMS) camera,[36–38] which are based on the complimentary metal-oxide-semiconductor (CMOS)

sensor. The unique capability of these cameras also allows for simultaneous imaging of the Newton Sphere at different arrival times, resulting in a 3-D slice image of the photofragment of interest. Further applications include exploring the photochemistry of larger molecules with numerous dissociation pathways where it would be time prohibitive to acquire consecutive images of every ion fragment.

1.5 Experimental apparatus

The velocity map ion imaging apparatus, a variant of the Wiley-McLaren TOF-MS, consists of three distinct regions: source, ionization, and drift/detection. A schematic of the apparatus used in the proceeding chapters of this thesis is shown in Figure 1-5. Each region is evacuated by turbomolecular pumps backed by oil-free Scroll and Roots pumps, resulting in a base pressure of ~10^{-8} torr in all regions.

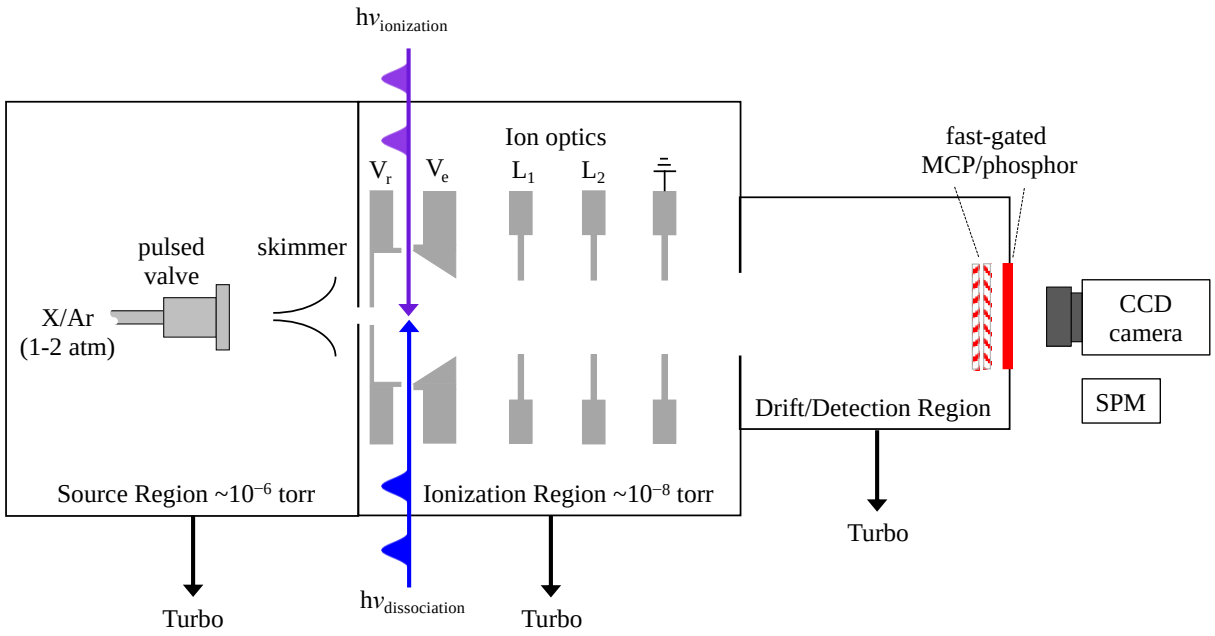

Figure 1-5 Schematic of the velocity map ion imaging spectrometer.

1.5.1 Source region: Molecular beam

In the source region, a target species (X) is seeded in an inert gas and a pulsed solenoid valve supersonically expands the gas from a high-pressure reservoir (backing pressure behind the valve) to a low-pressure region (source chamber). The gas valve operates with an opening time of 400 μs, increasing the operating pressure in the source chamber to $\sim 10^{-6}$ torr. During the expansion, the target molecules undergo several collisions with the seed gas, causing rapid collisional cooling through transfer of internal energy to translation. As the molecules accelerate away from the high-pressure reservoir, some will exceed the speed of sound and form a cold molecular beam. The coldest part of the beam is found at the center of the gas expansion directed along the TOF-axis and is preferentially selected using a pinhole orifice (skimmer) located downstream from the valve nozzle. The maximum terminal velocity of the gas can be described by the following expression:[39,40]

$$v = \sqrt{\frac{2k_B T}{m} \frac{\gamma}{\gamma - 1}}$$

where m is the mass of the seed gas, k_B is the Boltzmann constant, T is the temperature of the gas prior to expansion, and γ is the heat capacity ratio. For an ideal, monoatomic gas, the equation simplifies:[39,40]

$$v = \sqrt{\frac{5k_B T}{m}}$$

The experiments described in this thesis utilize room temperature argon as the seed gas and application of the above equation results in a beam terminal velocity of ~ 550 m s^{-1}. Typical

cooled gas temperatures are ~12 K. The properties of the molecular beam can be manipulated by changing the seed gas, pulse valve nozzle diameter, or backing pressure. For example, a heavier seed gas is more effective at collisional cooling and can result in increased cluster formation, which may or may not be desirable depending on the experiment.

1.5.2 Ionization region: Photofragment ionization

The cold molecular beam passes into a differentially pumped ionization region and is intersected by two counterpropagating photolysis and ionization lasers, illustrated in Figure 1-5. Ionization methods are essential to the VMI technique and a myriad of laser-based methods have been developed over the years, including quantum-state selective schemes. Two ionization methods extensively utilized in the experimental work of this thesis are described in the following subsections.

1.5.2.1 'Universal' ionization

Fragments with sufficiently low ionization potentials can be ionized and detected using a 'universal' ionization scheme with no quantum state specificity. Single-photon vacuum ultraviolet (VUV) ionization at 118.2 nm is commonly used in photodissociation experiments and can 'universally' ionize all photolysis products with ionization potentials less than 10.49 eV. Coherent VUV radiation at 118.2 nm is readily generated through frequency tripling the third harmonic of an Nd:YAG laser (355 nm) in a phase-matched noble gas mixture of xenon and argon, acting as the non-linear medium.[41] A schematic of the VUV static gas cell utilized in this thesis is shown in Figure 1-6. The static cell contains a phase-matched Xe/Ar mixture in a 1:10 ratio at a pressure of ~70 torr. An attenuated 355 nm beam (15 mJ) is gently

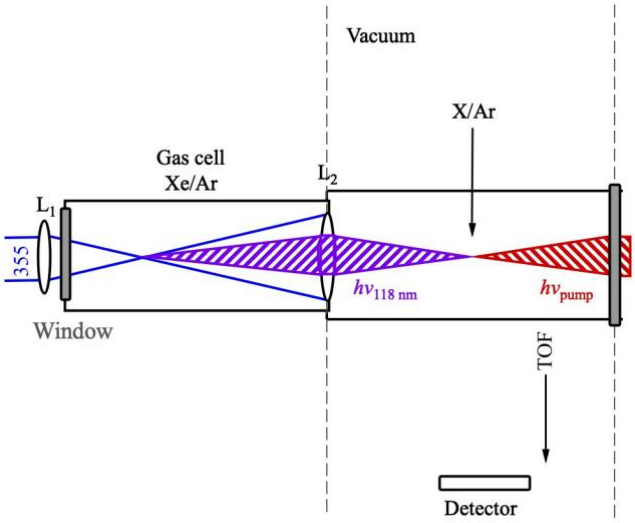

Figure 1-6 Schematic of a static gas cell used for generation of 118 nm light.

focused into the cell using a fused silica lens (L_1, f = 50 cm). A dual purpose internal MgF_2 lens (L_2, f = 20 cm) is used to both separate the gas cell from the high-vacuum ionization region and focus the 118 nm light into the molecular beam.

Advancements in VUV generation have given way to tunable VUV radiation using resonant third-order sum-difference frequency four wave mixing in a noble gas.[42,43] Generation of high energy VUV photons is challenging however, and they are less readily available than longer wavelength photons (λ > 200 nm), which are easily produced using frequency-doubled dye laser and optical parametric oscillator systems. A common technique that utilizes longer wavelengths for ionization is known as multiphoton ionization.

1.5.2.2 Multiphoton ionization

Ionization of an atom or molecule can be achieved through either resonant or non-resonant multiphoton ionization (MPI) processes. Non-resonant ionization requires multiple photons

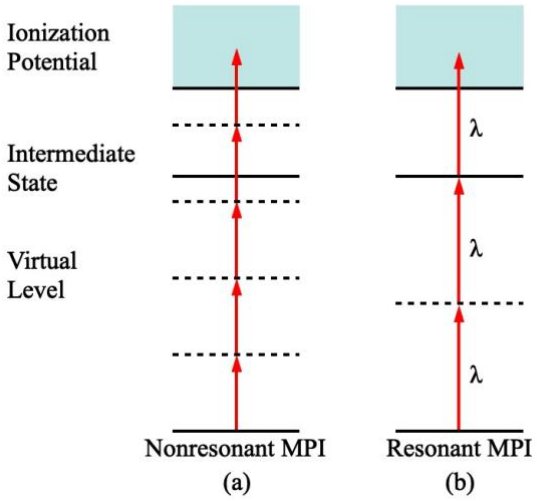

Figure 1-7 The principle of the multiphoton ionization (MPI) technique. (a) Nonresonant MPI: several photons interact to promote the system above the ionization potential. (b) 2+1 REMPI: two photons excite the system to some intermediate state and a third photon promotes the system above the ionization potential.

of light to interact on a time-scale shorter than the laser pulse. This results in direct ionization of the atom or molecule from its ground state and is illustrated in Figure 1-7(a). Non-resonant ionization has low probability and requires high photon density (intense laser light) in order to drive the processes.

Alternatively, resonance-enhanced multiphoton ionization (REMPI) is a sensitive laser-based technique used to probe specific molecular quantum states.[44] State-selective detection involves either one or multi photon absorption to a resonant intermediate state of the atom or molecule *via* a virtual state and is depicted in Figure 1-7(b). Following excitation, one or more photons are then absorbed to promote the electron out of the intermediate state and above the vertical ionization threshold. Resonance with an intermediate state enhances the probability of absorption and therefore enhances ionization. REMPI schemes are

commonly written as (m+n), with m representing the number of photons required to reach the resonant state and n being the number of photons needed for ionization. If the wavelength of the photon is not the same for both m and n, the notation (m+n') is used.

In this thesis, tunable UV light for REMPI detection is generated by frequency doubling the output of a dye laser (Quanta-Ray PDL 3, ~2 cm^{-1} bandwidth). A mid-band optical parametric oscillator (Continuum Horizon II) is also used to generate broad bandwidth UV light (~7 cm^{-1}) for both REMPI and MPI detection.

1.5.3 Ionization region: Velocity mapping electrodes

The ionization chamber houses a VMI stack comprised of five electrodes (Figure 1-5) and their design follows that of Livingstone *et al.*[45] The multi-lens assembly includes a repeller (V_r), extractor (V_e), two additional ion lenses (L_1 and L_2), and a ground (0 V) electrode. The critical parameter for effective velocity mapping (focusing), and therefore velocity resolution, is the voltage or 'gradient' ratio between the repeller and extractor potentials. The ratio is dependent on the spacings between the electrodes, the size of the opening, and length of flight path. For the apparatus described here, which has an elongated TOF path of 62 cm, velocity mapping conditions are achieved using a repeller-extractor voltage ratio of V_r:V_e = 0.87.

1.5.4 Detection region

The position sensitive detector consists of a pair of 40 mm diameter stacked microchannel plates (MCPs) arranged in a "chevron" configuration and backed to a P46 phosphor screen (Photonis) (refer to Figure 1-5). Experiments typically use a potential of 1.3–1.4 kV across

the MCPs, depending on signal intensity, and 4.0 kV on the phosphor screen. A fast-gated high voltage switch (Photek GM-MCP-2) is applied to the back MCP for DC slicing, limiting the time the detector is operating at normal voltages to only 22 ns. Finally, the ion strikes on the phosphor screen produce bright spots, which are captured using a CCD camera (Basler a312f, 782 × 582), yielding an ion image. To differentiate between ion strikes and background counts, spot size and intensities below a preset threshold are rejected using event counting software. For events above threshold, the 'centroid' of the ion strike is calculated by finding the pixel with the maximum intensity in the *x* and *y* directions. Centroid event counting greatly reduces the spot size of the ion strike and essentially eliminates noise events.[46] This method achieves sub-pixel resolution, increasing a 512 × 512 pixel region of interest to 1064 × 1064.

The total phosphorescence emitted from ions striking the detector is also captured using a silicon photomultiplier (SPM, SenSL MicroSL 10020-X18) and digitized using an oscilloscope (Teledyne Lecroy, HDO4054). Fragment identities are determined based on their t_{TOF}. All timings between the gas valve, laser beams, and gated detector are controlled and synchronized using a multi-channel digital delay generator (Quantum Composers 9528) running at 10 Hz.

1.6 References

1 A. Sanov and R. Mabbs, Photoelectron imaging of negative ions, *International Reviews in Physical Chemistry*, 2008, **27**, 53–85.

2 T. Suzuki, Femtosecond time-resolved photoelectron imaging, *Annu. Rev. Phys. Chem.*, 2006, **57**, 555–592.

3 D. M. Neumark, Slow Electron Velocity-Map Imaging of Negative Ions: Applications to Spectroscopy and Dynamics, *J. Phys. Chem. A*, 2008, **112**, 13287–13301.

4 D. A. Horke, G. M. Roberts, J. Lecointre and J. R. R. Verlet, Velocity-map imaging at low extraction fields, *Review of Scientific Instruments*, 2012, **83**, 063101.

5 I. León, Z. Yang, H.-T. Liu and L.-S. Wang, The design and construction of a high-resolution velocity-map imaging apparatus for photoelectron spectroscopy studies of size-selected clusters, *Review of Scientific Instruments*, 2014, **85**, 083106.

6 R. Wester, Velocity map imaging of ion–molecule reactions, *Phys. Chem. Chem. Phys.*, 2014, **16**, 396–405.

7 J. J. Lin, J. Zhou, W. Shiu and K. Liu, Application of time-sliced ion velocity imaging to crossed molecular beam experiments, *Review of Scientific Instruments*, 2003, **74**, 2495–2500.

8 A. von Zastrow, J. Onvlee, D. H. Parker and S. Y. T. van de Meerakker, Analysis of velocity-mapped ion images from high-resolution crossed-beam scattering experiments: a tutorial review, *EPJ Techniques and Instrumentation*, 2015, **2**, 11.

9 S. J. Greaves, R. A. Rose and A. J. Orr-Ewing, Velocity map imaging of the dynamics of bimolecular chemical reactions, *Physical Chemistry Chemical Physics*, 2010, **12**, 9129–9143.

10 M. N. R. Ashfold, N. H. Nahler, A. J. Orr-Ewing, O. P. J. Vieuxmaire, R. L. Toomes, T. N. Kitsopoulos, I. A. Garcia, D. A. Chestakov, S.-M. Wu and D. H. Parker, Imaging the dynamics of gas phase reactions, *Phys. Chem. Chem. Phys.*, 2006, **8**, 26–53.

11 G. Wu, W. Zhang, H. Pan, Q. Shuai, B. Jiang, D. Dai and X. Yang, A new crossed molecular beam apparatus using time-sliced ion velocity imaging technique, *Review of Scientific Instruments*, 2008, **79**, 094104.

12 J. Meyer and R. Wester, Ion–Molecule Reaction Dynamics, *Annu. Rev. Phys. Chem.*, 2017, **68**, 333–353.

13 C. Y. Ng, Ed., *Photoionization and photodetachment*, World Scientific, Singapore ; River Edge, NJ, 2000.

14 A. Vredenborg, C. S. Lehmann, D. Irimia, W. G. Roeterdink and M. H. M. Janssen, The Reaction Microscope: Imaging and Pulse Shaping Control in Photodynamics, *ChemPhysChem*, 2011, **12**, 1459–1473.

15 A. Schmaunz, U. Kensy, A. Slenczka and B. Dick, Velocity resolved REMPI spectroscopy : a new approach to the study of photodissociation dynamics, *Physical Chemistry Chemical Physics*, 2009, **11**, 7115–7119.

16 M. Brouard, E. K. Campbell, A. J. Johnsen, C. Vallance, W. H. Yuen and A. Nomerotski, Velocity map imaging in time of flight mass spectrometry, *Review of Scientific Instruments*, 2008, **79**, 123115.

17 C. Vallance, 'Molecular photography': velocity–map imaging of chemical events, *Philosophical Transactions of the Royal Society of London. Series A: Mathematical, Physical and Engineering Sciences*, 2004, **362**, 2591–2609.
18 B. J. Whitaker, Ed., *Imaging in Molecular Dynamics: Technology and Applications (A User's Guide)*, Cambridge University Press, Cambridge, 2003.
19 A. G. Suits, Invited Review Article: Photofragment imaging, *Review of Scientific Instruments*, 2018, **89**, 111101.
20 M. M. Wolff and W. E. Stephens, A Pulsed Mass Spectrometer with Time Dispersion, *Review of Scientific Instruments*, 1953, **24**, 616–617.
21 W. C. Wiley and I. H. McLaren, Time-of-Flight Mass Spectrometer with Improved Resolution, *Review of Scientific Instruments*, 1955, **26**, 1150–1157.
22 D. W. Chandler and P. L. Houston, Two-dimensional imaging of state-selected photodissociation products detected by multiphoton ionization, *J. Chem. Phys.*, 1987, **87**, 1445–1447.
23 A. T. J. B. Eppink and D. H. Parker, Velocity map imaging of ions and electrons using electrostatic lenses: Application in photoelectron and photofragment ion imaging of molecular oxygen, *Review of Scientific Instruments*, 1997, **68**, 3477–3484.
24 B. Dick, Inverting ion images without Abel inversion: maximum entropy reconstruction of velocity maps, *Phys. Chem. Chem. Phys.*, 2013, **16**, 570–580.
25 V. Dribinski, A. Ossadtchi, V. A. Mandelshtam and H. Reisler, Reconstruction of Abel-transformable images: The Gaussian basis-set expansion Abel transform method, *Review of Scientific Instruments*, 2002, **73**, 2634–2642.
26 G. A. Garcia, L. Nahon and I. Powis, Two-dimensional charged particle image inversion using a polar basis function expansion, *Review of Scientific Instruments*, 2004, **75**, 4989–4996.
27 DAVIS: A direct algorithm for velocity-map imaging system: The Journal of Chemical Physics: Vol 148, No 19, https://aip.scitation.org/doi/10.1063/1.5025057, (accessed May 14, 2019).
28 C. Bordas, F. Paulig, H. Helm and D. L. Huestis, Photoelectron imaging spectrometry: Principle and inversion method, *Review of Scientific Instruments*, 1996, **67**, 2257–2268.
29 K. Zhao, T. Colvin, W. T. Hill and G. Zhang, Deconvolving two-dimensional images of three-dimensional momentum trajectories, *Review of Scientific Instruments*, 2002, **73**, 3044–3050.
30 G. M. Roberts, J. L. Nixon, J. Lecointre, E. Wrede and J. R. R. Verlet, Toward real-time charged-particle image reconstruction using polar onion-peeling, *Review of Scientific Instruments*, 2009, **80**, 053104.
31 C. R. Gebhardt, T. P. Rakitzis, P. C. Samartzis, V. Ladopoulos and T. N. Kitsopoulos, Slice imaging: A new approach to ion imaging and velocity mapping, *Review of Scientific Instruments*, 2001, **72**, 3848–3853.
32 D. Townsend, M. P. Minitti and A. G. Suits, Direct current slice imaging, *Review of Scientific Instruments*, 2003, **74**, 2530.
33 C. Vallance, M. Brouard, A. Lauer, C. S. Slater, E. Halford, B. Winter, S. J. King, J. W. L. Lee, D. E. Pooley, I. Sedgwick, R. Turchetta, A. Nomerotski, J. John John and L. Hill,

Fast sensors for time-of-flight imaging applications, *Physical Chemistry Chemical Physics*, 2014, **16**, 383–395.

34 X. Llopart, R. Ballabriga, M. Campbell, L. Tlustos and W. Wong, Timepix, a 65k programmable pixel readout chip for arrival time, energy and/or photon counting measurements, *Nuclear Instruments and Methods in Physics Research Section A: Accelerators, Spectrometers, Detectors and Associated Equipment*, 2007, **581**, 485–494.

35 M. Fisher-Levine and A. Nomerotski, TimepixCam: a fast optical imager with time-stamping, *J. Inst.*, 2016, **11**, C03016–C03016.

36 J. J. John, M. Brouard, A. Clark, J. Crooks, E. Halford, L. Hill, J. W. L. Lee, A. Nomerotski, R. Pisarczyk, I. Sedgwick, C. S. Slater, R. Turchetta, C. Vallance, E. Wilman, B. Winter and W. H. Yuen, PImMS, a fast event-triggered monolithic pixel detector with storage of multiple timestamps, *J. Inst.*, 2012, **7**, C08001–C08001.

37 A. T. Clark, J. P. Crooks, I. Sedgwick, R. Turchetta, J. W. L. Lee, J. J. John, E. S. Wilman, L. Hill, E. Halford, C. S. Slater, B. Winter, W. H. Yuen, S. H. Gardiner, M. L. Lipciuc, M. Brouard, A. Nomerotski and C. Vallance, Multimass Velocity-Map Imaging with the Pixel Imaging Mass Spectrometry (PImMS) Sensor: An Ultra-Fast Event-Triggered Camera for Particle Imaging, *J. Phys. Chem. A*, 2012, **116**, 10897–10903.

38 I. Sedgwick, A. Clark, J. Crooks, R. Turchetta, L. Hill, J. John, A. Nomerotski, R. Pisarczyk, M. Brouard, S. Gardiner, E. Halford, J. Lee, M. Lipciuc, C. Slater, C. Vallance, E. Wilman, B. Winter and W. Yuen, in *10th IEEE International NEWCAS Conference*, 2012, pp. 497–500.

39 W. Christen, K. Rademann and U. Even, Supersonic Beams at High Particle Densities: Model Description beyond the Ideal Gas Approximation, *J. Phys. Chem. A*, 2010, **114**, 11189–11201.

40 G. Scoles, Ed., *Atomic and molecular beam methods*, Oxford University Press, New York, 1988.

41 A. h. Kung, J. f. Young and S. e. Harris, Generation of 1182-Å radiation in phase-matched mixtures of inert gases, *Appl. Phys. Lett.*, 1973, **22**, 301–302.

42 J. P. Marangos, N. Shen, H. Ma, M. H. R. Hutchinson and J. P. Connerade, Broadly tunable vacuum-ultraviolet radiation source employing resonant enhanced sum–difference frequency mixing in krypton, *J. Opt. Soc. Am. B, JOSAB*, 1990, **7**, 1254–1259.

43 I. Strashnov, D. J. Blagburn, N. Thonnard and J. D. Gilmour, Tunable VUV light generation for resonance ionization mass spectrometry of Krypton, *Optics Communications*, 2009, **282**, 966–969.

44 M. N. R. Ashfold and J. D. Howe, Multiphoton Spectroscopy of Molecular Species, *Annual Review of Physical Chemistry*, 1994, **45**, 57–82.

45 R. A. Livingstone, J. O. F. Thompson, M. Iljina, R. J. Donaldson, B. J. Sussman, M. J. Paterson and D. Townsend, Time-resolved photoelectron imaging of excited state relaxation dynamics in phenol, catechol, resorcinol, and hydroquinone, *J. Chem. Phys.*, 2012, **137**, 184304.

46 B.-Y. Chang, R. C. Hoetzlein, J. A. Mueller, J. D. Geiser and P. L. Houston, Improved two-dimensional product imaging: The real-time ion-counting method, *Review of Scientific Instruments*, 1998, **69**, 1665–1670.

2 UV Photodissociation Dynamics of CHI_2Cl and its Role as a Photolytic Precursor for a Chlorinated Criegee Intermediate

This work is reproduced from Kapnas, K. M., Toulson, B. W., Foreman, E. S., Block, S. A., & Murray, C. *Phys. Chem. Chem. Phys.* **2017**, ***19***(46), 31039-31053, with permission from the Royal Society of Chemistry.

2.1 Abstract

Photolysis of geminal diiodoalkanes in the presence of molecular oxygen has become an established route to the laboratory production of several Criegee intermediates, and such compounds also have marine sources. Here, we explore the role that the trihaloalkane, chlorodiiodomethane (CHI_2Cl), may play as a photolytic precursor for the chlorinated Criegee intermediate ClCHOO. CHI_2Cl has been synthesized and its UV absorption spectrum measured; relative to that of CH_2I_2 the spectrum is shifted to longer wavelength and the photolysis lifetime is calculated to be less than two minutes. The photodissociation dynamics have been investigated using DC slice imaging, probing ground state I and spin-orbit excited I* atoms with 2+1 REMPI and single-photon VUV ionization. Total translational energy distributions are bimodal for I atoms and unimodal for I*, with around 72% of the available energy partitioned in to the internal degrees of freedom of the CHICl radical product, independent of photolysis wavelength. A bond dissociation energy of D_0 = 1.73±0.11 eV is inferred from the wavelength dependence of the translational energy release, which is slightly weaker than typical C–I bonds. Analysis of the photofragment

angular distributions indicate dissociation is prompt and occurs primarily via transitions to states of A″ symmetry. Complementary high-level MRCI calculations, including spin-orbit coupling, have been performed to characterize the excited states and confirm that states of A″ symmetry with highly mixed singlet and triplet character are predominantly responsible for the absorption spectrum. Transient absorption spectroscopy has been used to measure the absorption spectrum of ClCHOO produced from the reaction of CHICl with O_2 over the range 345–440 nm. The absorption spectrum, tentatively assigned to the *syn* conformer, is at shorter wavelengths relative to that of CH_2OO and shows far weaker vibrational structure.

2.2 Introduction

Organoiodine compounds are photochemical precursors for iodine atoms in the atmosphere and oxides of iodine play an important role in catalytic depletion of tropospheric ozone and new particle formation.[1,2] Oceans are the major source of organoiodine compounds, which are particularly important species in the marine boundary layer (MBL)[3,4]. Methyl iodide (CH_3I) is the most prevalent organoiodine compound in the MBL, although some dihalomethanes such as diiodomethane (CH_2I_2), which have absorption spectra that extend to longer wavelengths and shorter photolysis lifetimes, are larger contributors to the marine I atom flux.[5] Recent work has suggested that trihalomethanes could also be I atom precursors in the marine atmosphere. Liss and coworkers found chlorodiiodomethane (CHI_2Cl) and dibromoiodomethane ($CHIBr_2$) were present after several species of macroalgae in coastal seawater obtained around Mace Head, Ireland were incubated for several hours.[4] More recently, reactions of dissolved organic matter with HOI and/or I_2, generated at the ocean surface through the oxidation of iodide by ozone, has been suggested

as a ubiquitous sea-surface source of the trihalomethanes chlorodiiodomethane and iodoform (CHI_3).[6]

The gas-phase photodissociation dynamics of organoiodine compounds has a long history. CH_3I in particular is well studied, and a good summary can be found in a recent article by Gardiner *et al*.[7] The A band of CH_3I peaks near 257 nm and results from $\sigma^* \leftarrow n$ excitation. Absorption at wavelengths near the band maximum occurs primarily via a parallel transition to the repulsive $^3Q_1$ state which correlates with spin-orbit excited $I^*(^2P_{1/2})$ atoms. The small fraction of ground state $I(^2P_{3/2})$ atoms result from surface-hopping via an exit channel conical intersection. The fraction of the available energy partitioned into relative translation, f_T, of the CH_3 and I products is around 0.7–0.8. The subset of iodine-containing dihalomethanes CH_2XY (X = I, Y = Cl, Br, I) present different photochemistry, although the long-wavelength absorption bands still arise from $\sigma^* \leftarrow n$ excitations localized on the C–I chromophore and lead predominantly to cleavage of the C–I bond.[8]

$$CH_2IY + h\nu \rightarrow CH_2Y + I(^2P_{3/2}) \quad \text{(R1a)}$$

$$\rightarrow CH_2Y + I^*(^2P_{1/2}) \quad \text{(R1b)}$$

For the mixed dihalomethanes, CH_2ICl and CH_2IBr, the long wavelength absorption spectra are like that of CH_3I but the absorption maxima at ~270 nm lies to longer wavelength. Excitation in the A bands is due to transitions that are localized on the C–I bond and lead predominantly to formation of I atoms. For CH_2ICl the transitions localized on the C–Cl chromophore that lead to C-Cl bond cleavage lie significantly higher in energy and dissociation proceeds exclusively by C–I bond cleavage.[9–13] In contrast, Br atoms are also

formed as a minor channel following photolysis of CH_2IBr in the A band, an observation primarily attributed to simultaneous weak excitation of the partially overlapped higher lying transition that is localized on the C–Br bond.[14,15] In both CH_2ICl and CH_2IBr, dissociation occurs via strongly parallel transitions, with a reduced propensity for I* and a smaller fraction of the available energy partitioned into translation (f_T ~0.4) than for CH_3I. The addition of a second C–I chromophore and reduction in symmetry leads to the appearance of additional bands in the near-UV absorption spectrum of CH_2I_2, which extends to longer wavelengths.[16,17] The electronic structure of CH_2I_2 has been described qualitatively using an exciton model[8] as well as theoretically using *ab initio* calculations that include effects of spin-orbit coupling and show that excited states with heavily mixed singlet and triplet character are responsible for the absorption spectrum.[18,19] Photolysis of gas phase CH_2I_2 in the near-UV leads to energy being partitioned predominantly into internal excitation of the iodomethyl (CH_2I) radical rather than translation, with f_T reduced to ~0.2.[8,18,20–25] The I* yield is effectively zero following excitation at longer wavelengths, but steadily increases to almost 0.5 at 248 nm.[21,22] The photochemistry of dihalomethanes has also been studied in condensed phases using ultrashort laser pulses, with transient absorption measurements leading to the suggestion that the CH_2I–Y isomer is formed on short timescales.[26–30] In contrast to the dihalomethanes, little work has been done on trihalomethanes.

Interest in the photochemistry of CH_2I_2 has been re-invigorated recently by its use as a precursor for the laboratory synthesis of the Criegee intermediate formaldehyde oxide, CH_2OO. Criegee intermediates, R_1R_2COO, are important reactive species in the troposphere formed by alkene ozonolysis; the energized intermediates can decompose to form hydroxyl

radicals, while those that are stabilized by collisions react with trace species, in some cases leading to particle formation.[31–35] Photolysis of CH_2I_2 in the presence of O_2 was first demonstrated by Welz *et al.*[36] to be an efficient route to generate CH_2OO in sufficient concentration for kinetics studies at low pressure, following initial work by Eskola *et al*. who had identified I atom formation in the $CH_2I + O_2$ reaction.[37] The CH_2OO yield in the $CH_2I + O_2$ reaction approaches unity at low pressure, decreasing to ~30% at atmospheric pressure.[38–40] The UV absorption spectrum of CH_2OO has been measured using several spectroscopic techniques.[41–44] Photolysis of larger geminal diiodoalkanes to produce iodoalkyl radicals which can subsequently react with O_2 has been used successfully to produce larger Criegee intermediates.[45,46] While the major source of most Criegee intermediates in the atmosphere is alkene ozonolysis, the photolytic production of iodoalkyl radicals could also contribute in regions such as the MBL where precursor concentrations are elevated. Halogen-substituted alkenes react extremely slowly with ozone, with rate constants typically $<10^{-19}$ cm^3 s^{-1}.[47,48] Iodoalkyl radicals with additional halogen substituents may be an alternative source of halogenated Criegee intermediates.

In this paper, we report the UV absorption spectrum and near-UV photochemistry of the trihalomethane CHI_2Cl, which we hypothesize could act as a photolytic precursor for the chlorinated Criegee intermediate ClCHOO by way of chemistry analogous to that of CH_2I:

$$CHICl + O_2 \rightarrow ClCHOO + I \qquad (R2)$$

Recently, Cabezas *et al.* have produced ClCHOO in a pulsed electrical discharge and measured the rotational spectra of both *anti* and *syn* conformers using Fourier-transform microwave

spectroscopy.[49] Calculations suggest that *syn*-ClCHOO is more stable by 1088 cm^{-1} (0.1349 eV) without zero-point corrections. The photodissociation dynamics of CHI_2Cl in the wavelength range 355–266 nm has been studied using DC slice velocity-map ion imaging, probing I and I* atoms using 2+1 resonance-enhanced multiphoton ionization and single-photon vacuum ultraviolet (VUV) ionization. The experimental measurements are complemented by high-level multi-reference electronic structure calculations, including effects of spin-orbit coupling, that characterize the excited electronic states of CHI_2Cl responsible for the absorption spectrum and the dissociation dynamics. Broadband transient absorption spectroscopy experiments demonstrate that the reaction of the CHICl radical photoproduct with molecular oxygen leads to formation of the ClCHOO Criegee intermediate. The absorption spectrum of ClCHOO in the wavelength range 345–440 nm is also reported and tentatively assigned as being predominantly due to the *syn* conformer.

2.3 Experimental and theoretical methods

2.3.1 CHI_2Cl synthesis and characterization

CHI_2Cl, commonly used as a precursor for forming halogenated cyclo-propanes,[50,51] is not commercially available and was therefore synthesized using the procedure described by Li *et al*.[52] Chloroform (223 mL, 1.25 mol), triethylbenzylammonium chloride (TEBA) (5.0 g, 21.9 mol), a 50% NaOH solution (110 g, 2.75 mol) in water (220 mL), and a solution of NaI (500 g, 3.34 mol) in water (490 mL) were added to a round bottom flask. The reaction mixture was then heated to 65 °C for 24 h. After cooling, the mixture was poured into water (3 L) and extracted with CH_2Cl_2 (1 L × 4). The organic layer was washed with saturated

Na_2SO_3 solution, dried over Na_2SO_4, and concentrated. The crude reaction mixture was redistilled to provide the product as a light sensitive red liquid (136.5 g, 16%). ^1H and ^{13}C NMR spectra were consistent with those previously reported for this compound. The vapor pressure of CHI_2Cl at 294 K was determined by connecting an airtight glass vessel containing CHI_2Cl to a static cell and monitoring the pressure increase. To obtain the gas phase absorption spectrum, a small sample of CHI_2Cl was added to a sealed quartz cuvette and allowed to equilibrate. The UV absorption spectrum was measured from 190–400 nm at 294 K using a UV-visible spectrometer (Cary 50).

2.3.2 DC slice velocity-map slice ion imaging

Photodissociation experiments were performed in a DC slice velocity-map imaging (VMI) spectrometer. The main characteristics of the setup have been described previously.[18] A liquid sample of CHI_2Cl stored in a stainless steel bubbler was seeded in argon (approximately 1% CHI_2Cl) at 1 atm backing pressure and was supersonically expanded using a pulsed nozzle (General Valve Series 9) and skimmed (Beam Dynamics Inc.) to form a molecular beam. The molecular beam is directed along the time-of-flight axis into the ionization chamber and intersected perpendicularly by counter-propagating photolysis and probe laser beams in the center of velocity-mapping electrodes, optimized for DC slicing. A tunable mid-band optical parametric oscillator pumped by a Nd:YAG laser (Continuum Horizon II and Surelite EX) was used to generate the photolysis beam in the wavelength range 266–355 nm. The photolysis beam was focused using a fused silica lens (f = 300 mm). Nascent I and I* photofragments were probed approximately 30 ns after photolysis via single-photon VUV ionization or 2+1 REMPI using a Nd:YAG pumped frequency doubled dye

laser (Lambda Physik Scanmate II and Continuum Surelite II-10). VUV radiation at 118.2 nm was generated by frequency tripling the 3rd harmonic of a Nd:YAG laser in a gas mixture of Xe and Ar. The REMPI probe beam was generated by frequency doubling the fundamental output of a Nd:YAG-pumped dye laser. To avoid non-resonant multi-photon dissociation induced by the probe laser, the pulse energy did not exceed ~0.5 mJ. The ions were accelerated towards a detector comprising microchannel plates and a phosphor screen (Photonis). A fast, high voltage pulser (Photek GM-MCP-2) allows imaging of only the narrow central slice of the ion Newton sphere. Detector phosphorescence was captured using a CCD camera (Basler a312f) interfaced to a PC running custom data acquisition software (National Instruments LabVIEW) that performs centroiding and ion-counting.

2.3.3 Broadband Transient Absorption Spectroscopy

Experiments were performed in a flash photolysis, single-pass transient absorption flow cell apparatus that has been described in detail previously.[44,53] A pulsed Nd:YAG laser was used to photodissociate CHI_2Cl in the presence of excess O_2 at 355 nm and 266 nm (7±1 mJ pulse^{-1}). Spectra were recorded at 15 Torr total pressure with the gas mixture comprising 0.02% CHI_2Cl, 10% O_2 and N_2 balance. All gas flows were regulated by calibrated mass flow controllers (Alicat). Absorption spectra were measured over the range of 345–440 nm using probe LEDs nominally centered at 345 nm, 365 nm and 405 nm, each spanning 20–30 nm. The LEDs were pulsed at maximum brightness for up to 6 μs using a high-current driver (LightSpeed Technologies, HPLS-36). The broadband LED output was coupled into a fiber optic and collimated using an achromatic doublet. The photolysis laser and probe LED beams were overlapped along the complete 50 cm length of the flow cell using dichroic

mirrors chosen to transmit probe light to the red of the photolysis laser wavelength. The transmitted probe light was dispersed in a spectrometer operated with a resolution 2.2 nm and coupled to a low-noise, cooled CCD detector (Andor SR303i and iDus 420). Spectra were collected at a 10 Hz repetition rate with a 30 μs delay between photolysis and LED pulses.

2.3.4 *Ab initio* calculations

The geometry of CHI_2Cl was optimized for the ground electronic state using the explicitly correlated coupled cluster with single, double and perturbative triple excitations [CCSD(T)-F12b] method.[54,55] The cc-pVTZ-F12 basis set was used for hydrogen, carbon and chlorine,[56] with the cc-pVTZ-PP-F12 basis set and ECP28MDF small-core relativistic pseudopotential for iodine.[57,58] The MP2Fit and OptRI auxiliary basis sets specifically matched to these orbital basis sets were utilized in the density fitting of most of the two-electron integrals and in the resolution-of-the-identity, respectively.[57,59,60] Density fitting of the Fock and exchange matrices used the cc-pVTZ/JKFit and def2-QZVPP/JKFit auxiliary sets.[61,62] The geminal Slater exponent was set to 1.0 a_0^{-1} throughout, and the complementary auxiliary basis set (CABS) singles correction was computed and added to the reference energy.[61,62] The absorption spectrum of CHI_2Cl and potential energy curves along the C–I bond coordinate were calculated using the explicitly correlated multi-reference configuration interaction method with the Davidson correction (MRCI-F12+Q),[63–65] along with the double-zeta variants of the orbital and auxiliary basis sets detailed above. The complete-active-space self-consistent field (CASSCF) reference for these calculations consisted of 12 electrons in 10 orbitals (6 A′ and 4 A″ in C_s symmetry), which was determined by inspecting the natural orbitals from full-valence CASSCF calculations and removing any orbitals from the active

space that had occupations greater than 1.95 for both the equilibrium geometry and a geometry where the C–I distance had been elongated to 4.2 Å. The vertical excitation energies of the first 11 excited states (3 × ^{1}A′, 2 × ^{1}A″, 3 × ^{3}A′, and 2 × ^{3}A″) were calculated. Spin-orbit coupling calculations were conducted on these 11 spin-free states using two different methodologies: (i) The calculated absorption spectrum at the equilibrium geometry was produced at the spin-orbit MRCI level (MRCI-SO herein) using the CASSCF reference outlined above, with the cc-pVDZ basis set for hydrogen and carbon,[66] the cc-pV(D+d)Z basis for chlorine,[67] and the cc-pVDZ-PP basis and associated pseudopotential for iodine.[58] (ii) Potential energy curves were computed by scanning along a C–I bond distance (keeping all other internal coordinates fixed at the equilibrium geometry) with spin-orbit coupling calculated at the CASSCF level (CAS-SO) using analogous triple-zeta quality basis sets. In all spin-orbit coupling calculations the energy eigenvalues obtained in the preceding MRCI or CASSCF calculations were replaced by those precomputed at the MRCI-F12+Q/cc-pVDZ-F12 level, meaning only the spin-orbit matrix elements were calculated at the lower level of theory. The spin-orbit operator defined in the pseudopotential was used for iodine, with the Breit-Pauli operator used for lighter atoms. All calculations were carried out using the MOLPRO 2015.1 package of *ab initio* programs.[68,69]

2.4 Results and Discussion

2.4.1 CHI_2Cl absorption spectrum

The gas-phase UV absorption spectrum of CHI_2Cl from 220–400 nm at 294 K is shown in Figure 2-1. A vapor pressure of 0.58 torr at 294 K for CHI_2Cl was measured in a static gas

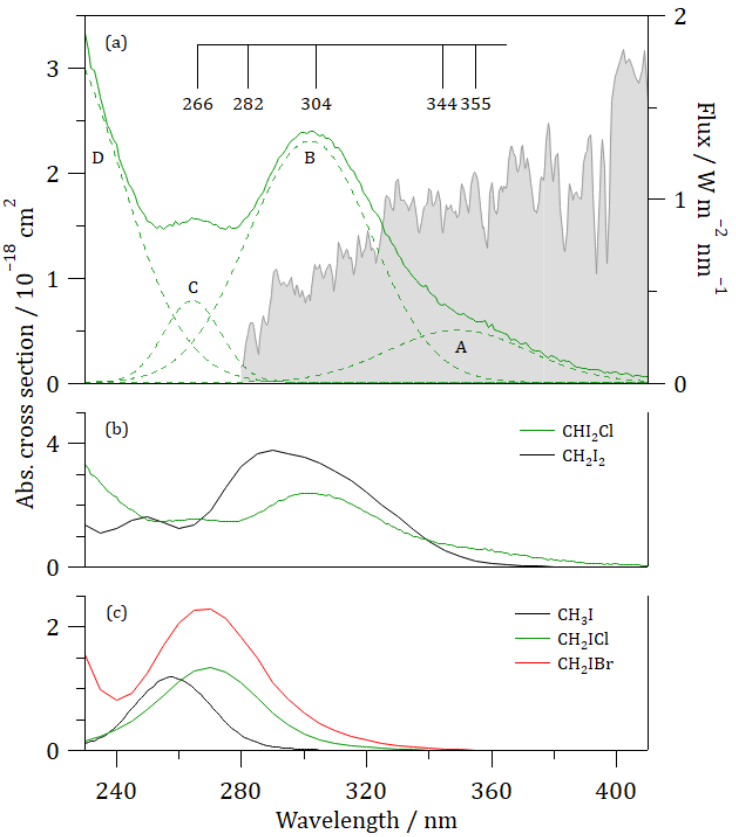

Figure 2-1 (a) Absorption spectrum for CHI_2Cl (green) at 295 K overlaid with individual Gaussian components (dashed) and AM1.5 solar irradiance spectrum (gray, shaded). The comb indicates the photolysis wavelengths used for ion imaging experiments. (b) Absorption spectra for CH_2I_2 (black, Mössinger et al.) and CHI_2Cl (this study). (c) Absorption spectra for CH_3I (black, Man et al.), CH_2ICl (green, Roehl et al.) and CH_2IBr (Mössinger et al.).

cell, and used to determine the absolute absorption cross section by means of a simple Beer-Lambert analysis. Analogous measurements of the absorption spectrum of CH_2I_2 vapor resulted in cross sections that were in excellent agreement with previously reported values in this wavelength range.[16,17] The absorption spectrum comprises five Gaussian bands, with maxima at 349 nm, 302 nm, 264 nm, 220 nm, and 209 nm, subsequently labeled A–E, respectively. Band E, which is not shown in Figure 2-1 has a peak absorption cross section of 2×10^{-17} cm^2 and is the most strongly absorbing feature in the spectrum. The absorption

spectrum of CHI_2Cl is similar to that of CH_2I_2, as shown in Figure 2-1(b) which is consistent with photoelectron spectroscopy measurements that have indicated that Cl–I interactions are relatively weak and has no effect on the bonding orbitals.[70]

However, the absorption bands of CHI_2Cl are slightly shifted to longer wavelength. Band A, which appears as a shoulder in the CH_2I_2 spectrum, is distinct in the CHI_2Cl spectrum and has the largest shift of ~31 nm. In contrast, bands B–D are shifted by only ~15 nm. The same behavior is observed in the spectra of CH_3I, CH_2ICl, and CH_2IBr where addition of a Cl or Br atom causes a similar shift of ~13 nm, as shown in Figure 2-1(c). The red shift is likely due to stabilization of the σ* antibonding orbital, as noted by Lee and Bersohn.[14] Photoelectron spectroscopy measurements on various halomethanes have suggested that the interactions between Cl or Br atoms with I are relatively weak.[70,71] Excitation of transitions involving orbitals localized on the C–Cl chromophores are expected to lie at wavelengths significantly shorter than 190 nm.

2.4.2 CHI_2Cl photodissociation dynamics

The photodissociation dynamics of CHI_2Cl has been studied using DC slice imaging of ground state I and spin-orbit excited I* atoms. I atoms were detected using single-photon VUV ionization at 118.2 nm following photolysis at 266 nm, 282 nm, 304 nm, 344 nm, and 355 nm. Ionization at 118.2 nm provides a high degree of specificity for I atoms over I* due to a resonance with an auto-ionizing Rydberg state, which results in a detection sensitivity that is 19.2 times greater.[72,73] I* atoms were detected using 2+1 REMPI transitions near 282 nm, 304 nm, and 344 nm in one-color experiments where the probe also acts as the photolysis

beam. Direct integration (and appropriate Jacobian transformation) of the sliced images represented in polar coordinates $I(r, \theta)$, yielded the photofragment radial $I(r)$ and angular distributions $I(\theta)$. The pixel-to-speed conversion factor was determined using S(^{1}D) calibration images obtained following photolysis of OCS at 235 nm. I (or I*) atom speeds were subsequently converted into total translational energy E_T using

$$E_T = \frac{1}{2} m_I (1 + \frac{m_I}{m_{CHICl}}) v_I^2$$

where it is assumed that the co-fragment is CHICl. The angular distributions were fit to the usual expression

$$I(\theta) \propto 1 + \beta P_2(\cos\theta)$$

where θ is the angle between the recoil velocity and the polarization of the photolysis laser and P_2 is the second Legendre polynomial. The angular distribution is characterized by the speed-dependent (or E_T-dependent) anisotropy parameter, β, which takes limiting values of +2 for a parallel dissociation and –1 for a perpendicular dissociation. The available energy E_{AVL} is the difference between the photon energy and the C–I bond dissociation energy, D_0, and is partitioned into internal excitation of the CHICl radical fragment, E_{INT}, spin-orbit excitation of the iodine atom (E_{SO} = 0 for I and 0.9426 eV for I*), and the translational energy associated with photofragment recoil, E_T:

$$E_{AVL} = h\nu - D_0 = E_{INT} + E_{SO} + E_T$$

The internal energy of the parent CHI_2Cl is assumed to be zero due to cooling in the supersonic expansion, and is omitted from the energy balance equation.

Overall, the results are remarkably similar to those obtained previously for CH_2I_2.[18] Figure 2-2 shows I atom images, total translational energy distributions, and E_T-dependent anisotropy parameters. The images comprise overlapping pairs of diffuse anisotropic rings, with radii that correspond to speeds of around 600–900 m s^{-1}. The maximum intensity for

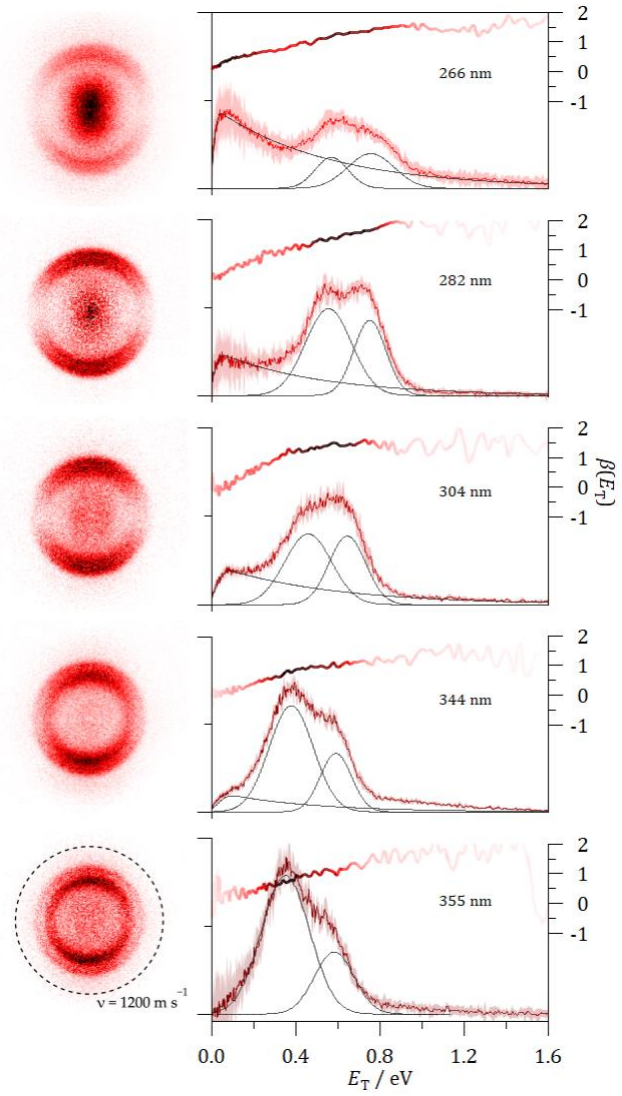

Figure 2-2 Ion images of I atom products following the photodissociation of CHI_2Cl at the indicated wavelengths and normalized translational energy distributions, $P(E_T)$. The individual components of the E_T distribution fits are shown as thin gray lines. E_T dependent anisotropy parameters, $\beta(E_T)$ are also shown, with the color scales weighted by the $P(E_T)$ distributions.

the fast-moving I atoms is found at the poles, parallel to the laser polarization axis, leading to near-limiting positive β parameters. An isotropic slow component grows in at the image centers at shorter wavelengths. The bimodal fast components of the $P(E_T)$ distributions in Figure 2-2 show a shift to greater E_T as the available energy increases. The equivalent data for I* atoms are shown in Figure 2-3.

The images are dominated by a single diffuse anisotropic ring, corresponding to I* speeds in the range 500–700 m s^{-1}. At a given photolysis wavelength, I* speeds are less than those of I. For example, excitation in the B band at 304 nm results in a most probable speed for I* of 610 m s^{-1} while for I the most probable speeds are 690 m s^{-1} and 790 m s^{-1}. That I* atoms

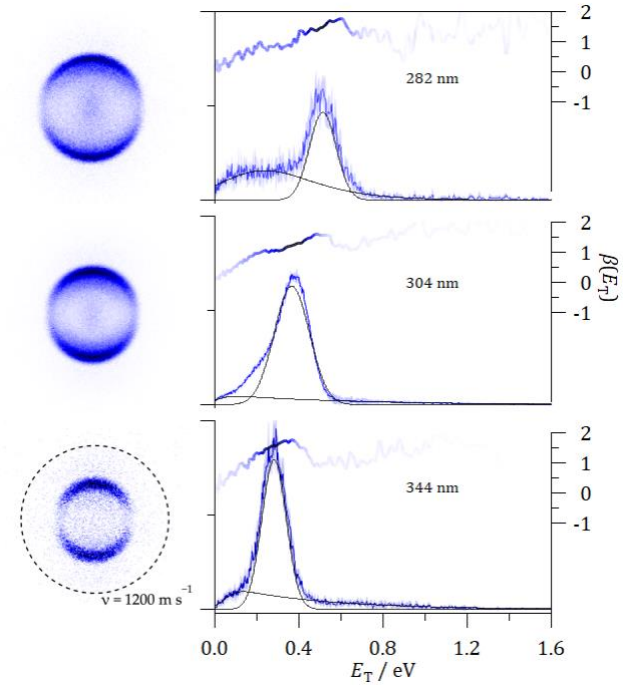

Figure 2-3 Ion images of I* atom products following the photodissociation of CHI_2Cl at the indicated wavelengths and normalized translational energy distributions, $P(E_T)$. The individual components of the E_T distribution fits are shown as thin gray lines. E_T dependent anisotropy parameters, $\beta(E_T)$ are also shown, with the color scales weighted by the $P(E_T)$ distributions.

are formed with lower speeds is unsurprising, since spin-orbit excitation reduces the available energy by almost 1 eV. We note that the most probable I* speeds do not correspond directly to either of the two fast components identified using VUV ionization. The angular distributions are again characterized by near-limiting positive β parameters. No two-color I* signal could be reliably distinguished above the large one-color I* signal induced by the REMPI laser alone at photolysis wavelengths of 355 nm.

Both I and I* atoms are formed with speeds that are significantly slower than the maximum allowed by energy conservation. Over the photolysis wavelength ranges used and based on typical C–I bond dissociation energies of ~2.2 eV,[74] the maximum speeds for I atoms span 1100–1500 m s^{-1} while the equivalent range for I* is only 600–1000 m s^{-1}. At all photolysis wavelengths, the I and I* atom speeds are smaller than v_{max}, and the total translational energy is substantially less than E_{AVL}. As with CH_2I_2 photolysis, internal excitation of the radical is significant. The $P(E_T)$ distributions obtained are decomposed by fitting the fast components to Gaussian functions. The translationally slow component that appears at short wavelength is fit to an exponentially-modified Gaussian; the origin of this component will be discussed later. The average total translational energy $\langle E_T \rangle$ associated with production of I atoms increases steadily with excitation energy from 0.41 eV to 0.68 eV; the separation between the two fast components remains fixed at around 0.20 eV. The unimodal distributions obtained detecting I* are in general slightly narrower than those obtained for I atoms with a FWHM of 0.16±0.3 eV rather than the values of 0.24±0.04 eV and 0.21±0.03 eV found for each component of the bimodal I atom E_T distributions. The trend in $\langle E_T \rangle$ is maintained

however, increasing from 0.28–0.51 eV as the photolysis wavelength is decreased from 344 nm to 282 nm. Energy partitioning data is summarized in Table 2.1

Table 2.1. Experimental energy partioning for I and I* channels of CHI_2Cl photodissociation. $\langle E_{INT} \rangle$ is partitioned into $\langle E_R \rangle$ and $\langle E_V \rangle$ using the Butler and co-workers impulsive model described in the text. Anisotropy parameters are averaged over the E_T distributions.

	λ / nm	E_{AVL} / eV	$\langle E_T \rangle$ / eV	$\langle E_R \rangle$ / eV	$\langle E_V \rangle$ / eV	$\langle \beta \rangle$
	355.0	1.76	0.41	0.56	0.80	+0.79
	344.5	1.87	0.44	0.59	0.84	+0.82
I	304.3	2.34	0.54	0.73	1.07	+1.32
	281.7	2.67	0.63	0.86	1.18	+1.47
	266.0	2.93	0.68	0.93	1.31	+1.32
	344.6	0.93	0.28	0.39	0.26	+1.56
I*	304.0	1.41	0.38	0.53	0.49	+1.27
	281.8	1.73	0.51	0.70	0.51	+1.49

Determination of the C–I bond dissociation energy. As shown in Figure 2-4, $\langle E_T \rangle$ increases linearly with the photolysis photon energy. If the fraction of the available energy partitioned into translation, f_T, is assumed to be constant, consistent with impulsive dissociation, the energy balance equation can be re-cast as

$$\langle E_T \rangle = f_T(h\nu - E_{SO}) - f_T D_0$$

where the slope is f_T and the x-intercept is D_0. For the I atom data, a linear fit yields a slope of 0.23±0.01 and a bond dissociation energy of 1.73±0.11 eV, where the uncertainties are derived from the fit. I* measurements were made at fewer photolysis wavelengths, but result in a consistent value for the D_0 of 1.70±0.63 eV, although with significantly larger uncertainty. The fraction of energy partitioned into translation for I* production is slightly larger at 0.28±0.05. We adopt the more precisely determined value of 1.73±0.11 eV for D_0 in CHI_2Cl. A similar analysis of the E_T distributions resulting from photolysis of CH_2I_2 resulted in a C–I bond dissociation energy of 2.16±0.01 eV,[18] a result that was in reasonably good agreement with earlier experimental measurements of 2.25±0.08 eV.[74] Weakening of the C–I bond is also predicted by theory. UCCSD calculations, using the cc-pVDZ-PP basis set for I atoms and cc-pVDZ for all others, predict C–I bond dissociation energies of 1.97 eV for CH_2I_2 and 1.71 eV for CHI_2Cl. The calculations neglect spin-orbit coupling and the quality of the agreement with experiment for CHI_2Cl is likely fortuitous. The observation of a weaker

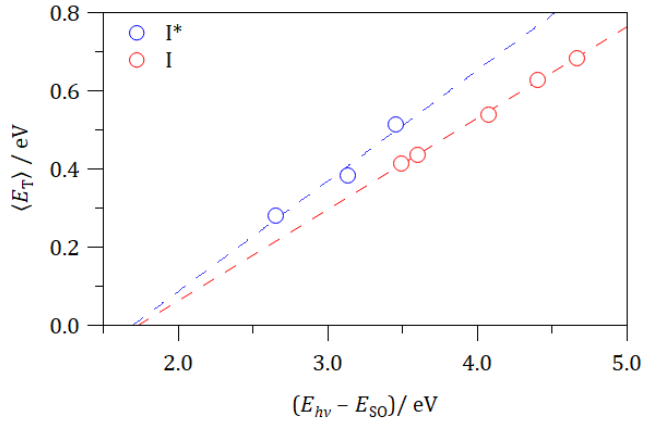

Figure 2-4 Average translational energies, $\langle E_T \rangle$, plotted as function of the difference between the photolysis photon energy, $E_{h\nu}$, and spin-orbit energy, E_{SO}, of the probed I/I* atoms. The x-intercept defines the bond dissociation energy.

C–I bond upon Cl atom addition appears to be at odds with photoelectron spectroscopy measurements on dihalomethanes, from which it had been inferred that interactions between the Cl and I atoms were weak. However, a weaker C–I bond is consistent with the chlorine atom having a stabilizing effect on the σ* antibonding orbital, which manifests in the absorption spectrum as a shift to longer wavelengths.

Using the experimental value of D_0, of 1.73 eV, the fraction of the available energy partitioned into translation $f_T = \langle E_T \rangle / E_{AVL}$ is independent of wavelength; f_T is 0.23 and 0.29 for I and I* atoms, respectively. This constancy occurs even though the excitation wavelengths span three distinct absorption bands and involve excitation to several electronic surfaces. The similarity of the total translational energy release suggests that the underlying electronic surfaces are topographically similar. The average internal energy of the CHICl radicals $\langle E_{INT} \rangle$ formed in conjunction with I* spans the range 0.64–1.23 eV following photolysis in the wavelength range 344–282 nm. $\langle E_{INT} \rangle$ for CHICl formed in conjunction with ground state I is even greater, varying from 1.35–2.25 eV as the photolysis wavelength is decreased from 355 nm to 266 nm. The formation of highly internally excited CHICl suggests a possible origin for the isotropic slow component that appears in the I atom images at shorter wavelengths. At 266 nm, where the slow component is most pronounced and accounts for around 70% of the I atoms detected, $\langle E_{INT} \rangle$ for CHICl radicals formed in conjunction with I atoms is 2.25 eV, which is close to typical values of D_0 for iodine-containing dihalomethanes, and significantly greater than that for CHI_2Cl. The typical FWHM of the Gaussian functions used to fit the E_T, or E_{INT}, distributions is ~0.2 eV. A fraction of the hot CHICl radicals will likely have sufficient energy to undergo unimolecular dissociation to form CHCl + I even at longer photolysis

wavelengths, consistent with the onset of the isotropic slow component. A slow component was also observed at shorter wavelengths in our earlier work on CH_2I_2 photolysis.[18] For CH_2I_2 photolysis, f_T was reported as decreasing from 0.24 to 0.15 for I atoms and from 0.23 to 0.19 for I* atoms following photolysis in the wavelength range 355 nm to 248 nm. However, these values were based upon the complete E_T distributions, which include significant slow components at shorter wavelengths that are likely due to secondary decomposition of hot CH_2I radicals. Including only the fast components of the E_T distributions eliminates the wavelength dependence and results in revised f_T values of 0.20±0.02 and 0.21±0.03 for I and I*, respectively. Among the dihaloalkanes, CH_2IX (X = Cl, Br, I), f_T is smallest for CH_2I_2; previous studies of the photolysis of CH_2IBr found f_T = 0.31,[15] while f_T values in the range 0.39–0.48 were measured for CH_2ICl.[12,13] The measured f_T for the trihaloalkane CHI_2Cl falls between those previously reported for CH_2I_2 and CH_2IBr.

The trend in f_T following C–I bond cleavage in the dihaloalkanes approximately follows the predictions of the impulsive model described by Busch and Wilson,[75] in which the CH_2X radical is treated as a pseudo-diatomic molecule, (CH_2)–X. The fractions of the available energy partitioned into translation, rotation and vibration are given by

$$f_T = \frac{\mu_a}{\mu_f}$$

$$f_R = (1 - f_T)\sin^2\theta$$

$$f_V = (1 - f_T)\cos^2\theta$$

where μ_a is reduced mass of the atoms involved in the breaking bond, μ_f is that of the

fragments, and θ is the I(CH_2)X angle, taken from *ab initio* optimized geometries. The model predicts f_T values of 0.36, 0.23 and 0.19 for CH_2ICl, CH_2IBr and CH_2I_2, respectively, which are in reasonably good agreement with the experimental measurements. According to the model, the remaining energy is partitioned primarily into haloalkyl radical rotation. The results of the impulsive model calculations are summarized in Table 2.2.

Table 2.2 Fractional energy partitioning into translation, rotation and vibration for CHI_2Cl photodissociation as predicted by the soft impulsive model of Busch and Wilson, or the modified impulsive model of Butler and co-workers (in parentheses), as discussed in the text.

	$f_{T,exp}$	f_T	f_R	f_v	$\mu b^2/I$
CH_2ICl	0.44	0.36	0.56 (0.48)	0.09 (0.16)	1.36
CH_2IBr	0.31	0.23	0.66 (0.59)	0.11 (0.18)	2.51
CH_2I_2	0.21	0.19	0.68 (0.62)	0.13 (0.19)	3.28
CHI_2Cl	0.26	0.15	(0.06)	(0.79)	0.38

The pseudo-diatomic approximation breaks down for CHI_2Cl and cannot be used to predict energy partitioning into rotation or vibration. The predicted value of f_T = 0.15 is however in reasonably good agreement with the experimental measurements. To estimate f_R and f_V, we turn to the modified impulsive model that has been developed by Butler and co-workers, which uses the measured recoil speeds to predict the rotational energy partitioning.[76,77] Recoil is assumed to be along the direction of the breaking bond, generating orbital angular momentum, $\boldsymbol{L}$

$$\boldsymbol{L} = \boldsymbol{r} \times \mu \boldsymbol{v}_{\text{recoil}}$$

where $\boldsymbol{r}$ is the vector between the centers of mass of the photofragments, and μ is the reduced mass. Angular momentum conservation requires that the angular momentum of the radical fragment is $\boldsymbol{J} = -\boldsymbol{L}$, if the initial angular momentum of the parent molecule is zero. Treating the radical rotation classically leads to

$$f_{\mathrm{R}} = \frac{\mu b^2}{I} f_{\mathrm{T}}$$

where b is the impact parameter and I is the scalar moment of inertia. Values of $\mu b^2/I$ are also collected in Table 2.2. For the dihalolkanes, where the heavy atoms lie in a plane, the implicit assumption that rotation is about one of the radical principal axes is holds true and I_{B} can be used. This model leads to f_{R} values that are slightly smaller than those predicted by the soft impulsive model for the dihaloalkanes when using f_{T}, as shown in Table 2.2. However, using experimental $f_{\mathrm{T,exp}}$ values for the dihaloalkanes results in unphysical results with $f_{\mathrm{T,exp}} + f_{\mathrm{R}} > 1$. For CHI_2Cl, the decrease in the impact parameter and increase in the radical moment of inertia dramatically reduces $\mu b^2/I$, leading to a small value of f_{R} and consequently, preferential partitioning into radical vibration (see Table 2.2). We note that the impulse is not perpendicular to one of the radical principal axes for CHI_2Cl and the classical rotational energy must instead be calculated using

$$E_R = \frac{1}{2}\boldsymbol{J}^T \mathbf{I}^{-1} \boldsymbol{J}$$

where $\boldsymbol{J}$ is the rotational angular momentum vector and $\mathbf{I}^{-1}$ is the inverse of the inertia tensor for the CHICl radical, evaluated at the geometry of the parent molecule, and is not diagonal. In practice, we use the PMIFST program[78] to rotate the CHICl radical into its principal axis

system and use the rotation matrix to apply the same transformation to the $\boldsymbol{r}$ and $\boldsymbol{v}_{\text{recoil}}$ vectors. Using average recoil speeds measured experimentally, E_R is calculated to range from 0.56–0.93 eV for I atoms and 0.39–0.70 eV for I* atoms, with larger values corresponding to photolysis at shorter wavelengths. On average, f_R is found to be 0.32 (0.40) and f_V is 0.45 (0.31) for I (I*) atoms.

Spin-orbit branching. Additional I atom images were acquired in one-color measurements using a 2+1 REMPI transition at 304.67 nm, near the 304.02 nm transition used to probe I*. These wavelengths correspond to excitation near the absorption maximum of the B band, as shown in Figure 2-1. The $P(E_T)$ distribution obtained probing I atoms state-selectively using REMPI is subtly different from that measured using single-photon VUV ionization following photolysis at 304.3 nm. The normalized $P(E_T)$ distributions obtained using REMPI detection of I and I* were used as basis functions to fit the VUV data.

$$P\left(E_{T,VUV}\right) = c_1 P\left(E_{T,I}\right) + c_2 P\left(E_{T,I^*}\right)$$

The photolysis wavelengths in the one-color measurements are constrained by the two-photon atomic resonances and differ in energy by only 9 meV. Figure 2-5 shows the results of the fit, which allows the coefficients c_1 and c_2 to vary, subject to the constraints that they are positive and sum to unity.

The best fit of the total translational energy distribution at 304 nm obtained using VUV ionization returns c_1 = 0.91 and c_2 = 0.09. After accounting for the relative photoionization cross sections, which strongly favor detection of I atoms, the yield of spin-orbit excited I* atoms is 0.65. The yield of spin-orbit excited iodine appears to be significantly larger than

in the dissociation of CH_2I_2, where yields of 0.26–0.35 have been reported following excitation to the B band maximum at 290 nm.[21,22]

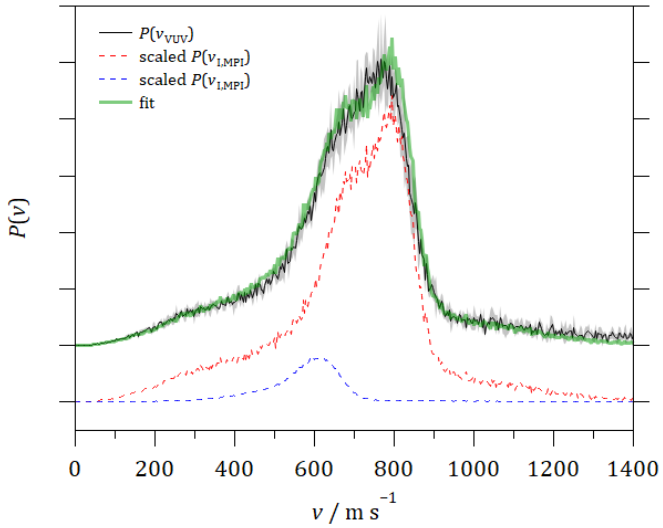

Figure 2-5 Decomposition of the iodine atom speed distribution obtained at a photolysis wavelength of 304 nm using VUV ionization (black). The best-fit fit linear combination of scaled state-selective I and I* speed distributions obtained using REMPI (dashed red and blue) is shown in green.

Angular distributions. E_T-dependent anisotropy parameters derived from fitting the I and I* angular distributions are shown in Figure 2-2 and Figure 2-3, respectively. The fast components are characterized by positive β at all photolysis wavelengths for both I and I*, confirming prompt dissociation and photofragment velocities that are preferentially parallel to the photolysis laser polarization. The component peaking near zero translational energy evident in the I atom data at shorter photolysis wavelengths, earlier attributed to secondary dissociation of CHICl radicals, has $\beta \approx 0$. The anisotropy parameters for the fast components of the E_T distributions are summarized in Table 2.1. For ground state I atoms, the E_T distributions are bimodal; the faster of the two components has a larger value of β, which also generally increases as the photolysis wavelength is decreased. The apparent turnover

at 266 nm is likely due to contributions from the underlying anisotropic component of the speed distribution. The MPI measurement at 304 nm gives results that agree with the VUV measurement for ground state I atoms. The anisotropy parameters for I* atoms fall between the values for I atoms at 304 nm and 282 nm (and agree with the average), but the value is significantly larger at 344 nm.

The β parameter can give insight into the symmetry of the electronically excited states involved in the dissociation. In the axial recoil approximation, the β parameter for a prompt dissociation is given by

$$\beta = 2P_2(\cos\chi)$$

where χ is defined as the angle between the transition dipole moment, $\hat{\boldsymbol{\mu}}$, and the Jacobi vector between the departing I atom and the center of mass of the CHICl radical, $\hat{\boldsymbol{R}}$.[79] CHI_2Cl

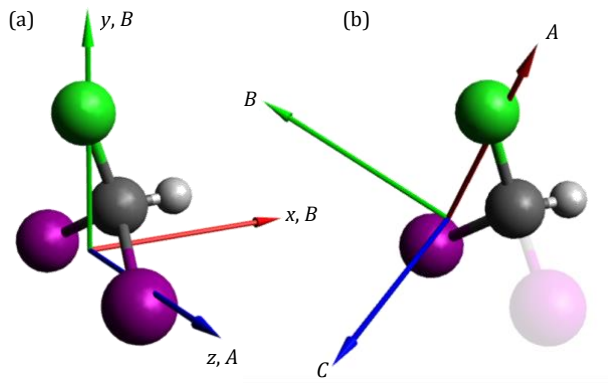

Figure 2-6 CHI_2Cl optimized geometry calculated at the CCSD(T)-F12b level. Principal inertial axes are indicated for the parent molecule and for the CHICl radical at the initial geometry, as used for the impulsive model calculations described in the text.

belongs to the C_s point group; the plane of symmetry is defined as the *x*–*y* plane, as depicted in Figure 2-6.

The transition dipole moments lie within the x–y plane for excitation to A′ states and along the *z*-axis for excitation to A″ states. Using the geometry for $\tilde{X}^1{}'$ CHI_2Cl obtained from the *ab initio* calculations, excitation to A″ states is predicted to lead to fragments with a limiting value for β of +1.87, while excitation to A′ states will result in anisotropy parameters in the range –0.99 to –0.87, for transition dipole moments aligned along the *x* or *y* axes. Positive values of β are observed at all photolysis wavelengths for both I and I* atoms, indicating that the photochemistry is dominated by excitation to repulsive states of A″ symmetry. The *ab initio* absorption spectrum calculated at the MRCI-SO level and shown in Figure 2-7 supports the experimental inference, showing the long wavelength absorption to be dominated by

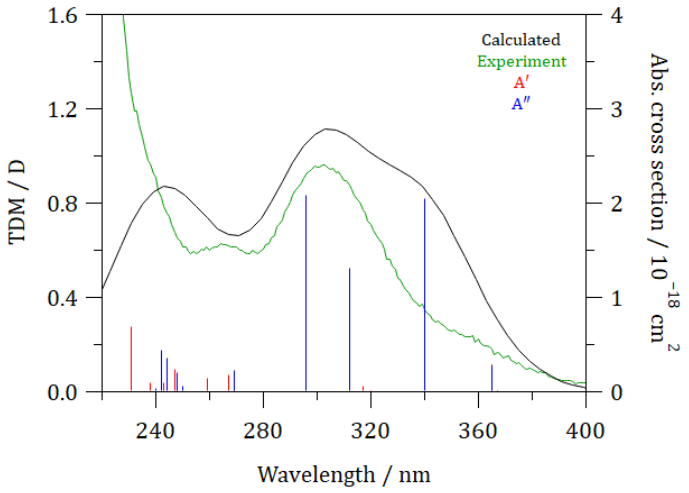

Figure 2-7 MRCI-F12+Q calculated (black) and experimental (green) absorption spectra for CHI_2Cl. The stick spectrum shows transition dipole moments plotted against vertical excitation energies for A′ (red) and A″ (blue) states. The vertical transitions have been broadened by a 20 nm FWHM Gaussian function and shifted 31 nm to longer wavelengths.

absorption to the 2A″, 3A″ and 4A″ states (see also Table 2.3).

Potential energy curves. Extension of a C–I bond reduces the point group symmetry to C_1, allowing all states to mix and making MRCI calculations including spin-orbit coupling (MRCI-SO) unaffordable for calculating the potential energy curves along the dissociation coordinate. Figure 2-8 shows potential energy curves calculated spin-free (at the MRCI-F12+Q level), and with spin-orbit coupling at the CASSCF level (CAS-SO, see the theoretical methods section for full details). CAS-SO calculations at the equilibrium geometry provided a qualitatively similar picture to the MRCI-SO calculations, predicting that three A″ states were primarily responsible for the absorption, albeit with different transition dipole

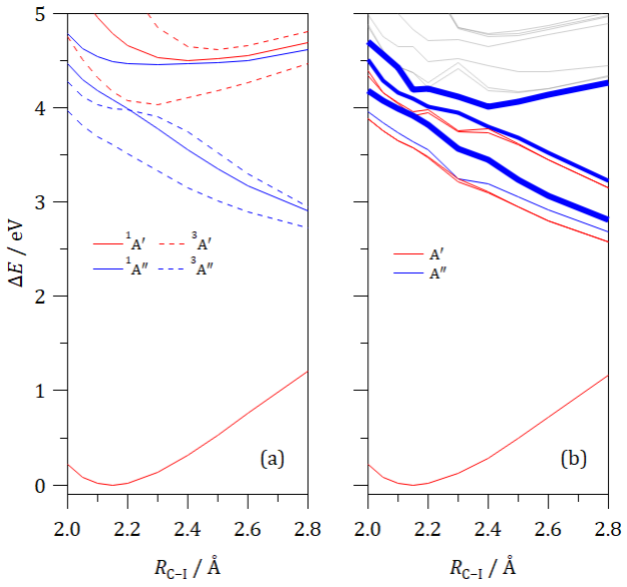

Figure 2-8 *Ab initio* potential energy curves (PECs) along the C–I bond coordinate for CHI_2Cl. (a) MRCI-F12+Q spin-free PECs, (b) CASSCF spin-orbit coupled PECs. Red curves are states with A′ symmetry at the C_s equilibrium geometry and blue curves are A″ symmetry. In panel (a) solid lines indicate singlet states, while dashed curves indicate triplet states. In panel (b), the states primarily responsible for the absorption spectrum are emboldened.

moments. The spin-free MRCI-F12+Q potential energy curves are shown in Figure 2-8(a), with symmetry labels assigned based on the energy ordering of the electronically excited states at the C_s equilibrium geometry. The lower energy states that correlate with CHICl + I products have A″ symmetry exclusively and are repulsive, although for the 2^3A″ state this results from a conical intersection with the 1^3A′ state at slightly extended C–I bond lengths. The higher energy states are bound along the C–I coordinate and correlate with electronically excited CHICl radicals.

The CAS-SO potential energy curves are shown in Figure 2-8(b). For clarity, the higher energy states that do not influence the photochemistry in the range of experimental excitation energies are grayed out. The three CAS-SO states equivalent to those carrying the greatest oscillator strengths in the MRCI-SO calculations are emboldened. The 2A″ and 3A″ states are repulsive and correlate with CHICl + I and CHICl + I*, respectively, while the 4A″ state is bound and correlates with electronically excited radicals. The 2A″ state has predominantly singlet character and is equivalent to the 1^1A″ state in the spin-free calculations. The higher energy 3A″ and 4A″ states, however, contain significant triplet character, as indicated in Table 2.3.

Table 2.3. Spin-orbit coupled MRCI-F12+Q electronically excited state energies, transtion dipole moments and percentage triplet character calcaulted at the CCSD(T)-F12 equilibrium geometry.

State	E–E_1 / eV	TDM / D	% triplet
1 A′	0.000		99%
1 A″	3.768	0.116	16%
2 A″	4.066	0.819	96%
3 A″	4.466	0.526	46%
4 A″	4.734	0.835	55%
6 A″	5.262	0.092	100%
6 A'	5.293	0.083	99%
7 A'	5.489	0.067	94%

Bimodal and unimodal E_T distributions for I and I* atoms, respectively have also been observed in the near-UV photochemistry of CH_2I_2.[18,24] One possible explanation for this bimodality is the splitting of spin-orbit excited CHICl*, although no theoretical evidence was seen to confirm formation of CHIClI*. Toulson *et al.* did not observe spin-orbit splitting for the CH_2I radical after photodissociation of CH_2I_2. They suggested that either the spin-orbit coupling is much smaller than predicted or no spin-orbit excited CH_2I was produced.[18] Spin-orbit coupling constants (A_{SO}) in the CH_2I and CH_2Cl radicals have previously been derived from spectroscopic data and found to be 1392 cm^{-1} (0.17 eV)[80] and 116 cm^{-1} (0.014 eV),[81] respectively. The coupling constant in CH_2Cl is 12 times smaller than for CH_2I, suggesting that the addition of a chlorine atom would have a minor effect on the spin-orbit coupling in

CHClI. It is unlikely that spin-orbit splitting of the radical accounts for the bimodal distributions. Xu *et al*. suggested that the slower components of the E_T distributions obtained probing I atoms arose from direct excitation to a repulsive surface while the faster component resulted from a curve crossing mechanism following initial excitation to a state that correlated with I* prodcuts.[24] This interpretation was based on the faster I atoms and the I* atoms having the same $\langle\beta\rangle$, while the slower I atoms had a smaller $\langle\beta\rangle$. The E_T-dependent anisotropy parameters obtained for CHI_2Cl photolysis show a similar trend, although the distinction between the faster and slower components for I atoms is less clear. In the context of the CAS-SO curves for CHI_2Cl, the equivalent mechanism would involve I* atoms being formed after direct excitation to the 3A″ surface, with a subset undergoing a surface hop to a lower lying surface correlating to ground state I atoms. The slower component in the I atom E_T distribution would then result from direct excitation to and dissociation on the 2A″ surface. We note that the faster component of the I atom E_T distributions and the I* E_T distributions also result in the same fraction of E_{AVL} being partitioned into translation, $f_T \approx 0.29$. The absence of any measurable I* signal, yet still a bimodal E_T distribution for I atoms at longer photolysis wavelengths, would suggest that the probability of surface hopping from the 3A″ state is near unity at lower excitation energies and decreases as the excitation energy is increased. The slight increase in the fractional contribution of the faster component at shorter photolysis wavelengths, could be explained by preferential excitation to the 3A″ state over the 2A″ state, even as the hopping probability decreases.

In opposition to this mechanism, we note that the CAS-SO potential energy curves do not

show any obvious crossings between the 3A″ surface and lower energy states correlating with CHICl + I products. Furthermore, as noted by Merrill *et al*. discussing $CHBrCl_2$ photochemistry,[82] the curve crossing mechanism might be expected to enhance vibrational excitation of the radical leading to slower fragments, while the angular anisotropies for CHI_2Cl imply that the faster I fragments results from trajectories that began on the 3A″ surface. However, the CAS-SO curves are one-dimensional cuts through the multidimensional potential energy surface, which dictates the energy disposal while the lack of symmetry resulting from any deviation from the equilibrium geometry will allow nonadiabatic interactions between the electronically excited states. Multidimensional curves would be needed to further understand the origin of this crossing and ultimately the energy disposal.

2.4.3 ClCHOO absorption spectrum

Single pass transient absorption spectroscopy was used to measure the absorption spectrum of ClCHOO in the 345–440 nm wavelength range using the same approach as our previous work on CH_2OO.[44] Photolysis of CHI_2Cl at 355 nm and 266 nm was used to generate CHICl radicals in a 50 cm flow cell. Photolysis at 266 nm required different beam steering dichroic mirrors and allowed measurements to be extended slightly further to the blue, although the measurements are limited by the availability of sufficiently bright LEDs in the UV. Strong time-dependent absorbance of the LED probe light was observed only with the photolysis laser on and with O_2 present in flow cell. Significant absorbance due to IO was observed at longer (~100 μs) photolysis–probe delays while the non-IO absorbance reached a maximum after around 30 μs. The relative appearance times are similar to those in the $CH_2I + O_2$

reaction, where maximum concentrations of IO and CH_2OO were reached after approximately 100 μs and 10 μs, respectively. IO is known to be a minor product of the $CH_2I + O_2$ reaction at low pressure, and is formed both directly and as a result of the secondary reaction between CH_2OO and I atoms.[40,83] For the $CHICl + O_2$ reaction, formation of the Criegee intermediate appears to be somewhat slower and the appearance of IO at longer times is consistent with it being formed primarily by secondary reactions (e.g. $ClCHOO + I \rightarrow ClCHO + IO$). Figure 2-9 shows the resulting absorption spectrum, attributed to ClCHOO, alongside that of CH_2OO after subtraction of the IO contribution.

Conversion of the measured absorbance to an absolute absorption cross section for ClCHOO as shown in Figure 2-9 requires an estimate of the number density present in the flow cell. The same approach used previously to determine the wavelength-dependent absorption cross section for CH_2OO,[44] which gave results in excellent agreement with independently calibrated measurements.[43] First, the initial CHICl number density is determined from that of the precursor CHI_2Cl, measured directly by single-pass absorption, and the photolysis laser fluence, assuming a unit quantum yield. Two estimates are required to obtain the concentration of ClCHOO: the yield for this product from the $CHICl + O_2$ reaction and a correction factor to account for the time dependence. We determine the latter empirically from transient absorption measurements, and assume the former is the same as that determined previously for the pressure-dependent CH_2OO yield of the $CH_2I + O_2$ reaction. The estimated ClCHOO yield is the most important approximation and could lead to a (readily corrected) systematic error in the reported absorption cross section. With this caveat, it appears that the magnitude of the ClCHOO absorption cross section is comparable

to that of CH_2OO in the wavelength region studied. It is clear from Figure 2-9, however, that the band maximum lies to wavelengths shorter than 345 nm.

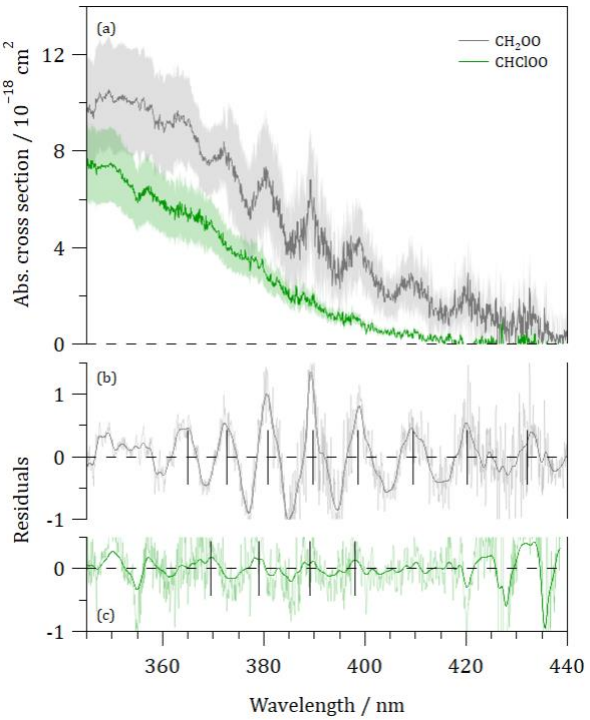

Figure 2-9 (a) UV absorption spectrum of ClCHOO (green) and CH_2OO (gray). (b) and (c) show the residuals after subtraction of a smoothed spectrum. The vertical lines indicate the positions of vibrational bands. The oscillations at $\lambda > 420$ nm in panel (c) arise from over-subtraction of the background IO absorbance.

The absorption spectrum of CH_2OO shows distinctive vibrational structure, with a clear progression of diffuse bands separated by 610±40 cm^{-1}. The first band at ~432 nm was tentatively assigned as the origin.[44] Recently, Ting and Lin have reported the absorption spectrum of the deuterated Criegee intermediate, CD_2OO, finding significant isotope shifts.[84] Calculations suggest that CH_2OO maintains its planar structure following excitation to the $\tilde{B}^1A'$ state, with the major geometric changes being contraction of the CO bond, extension of

the OO bond and a decrease in the COO bond angle.[85,86] However, projections of the ground state vibrational wavefunctions, calculated at the MR-PT2 level, onto the $\tilde{B}$ state surface, suggested that three modes comprising the out-of-plane CH_2 wag, CH_2 scissors + CO stretch, and OO stretch are Franck-Condon active and are largely responsible for the structure in the absorption spectrum, in agreement with experiment.[86] In contrast, the absorption spectrum of ClCHOO shows far weaker structure. Following Ting and Lin, the absorption spectra are heavily smoothed and subtracted from the higher resolution data; the residuals are shown in Figure 2-9. The CH_2OO residual shows highly oscillatory structure resulting from the vibrational progression. Weaker oscillations are observed in the ClCHOO residual. The first band appears at ~398 nm and the average peak-to-peak separation is 640±60 cm^{-1}. The absorption spectra of the methyl-substituted Criegee intermediates CH_3CHOO and $(CH_3)_2COO$ are also largely featureless.[87,88]

ClCHOO can exist as two conformers, which can be labelled *syn* and *anti*, following the notation established for CH_3CHOO according to the OOCCl torsion angle. Single point EOM-CCSD/aug-cc-pVTZ calculations have been performed at the ground state geometry to explore the effect of the Cl atom on the low-lying electronically excited states of both conformers relative to those of CH_2OO. Table 2.4 summarizes the results. The presence of the Cl atom has a marked effect on the vertical excitation energy, increasing that of the *syn*-ClCHOO conformer by 0.21 eV and decreasing that of *anti*-ClCHOO by 0.25 eV, with respect to CH_2OO. The oscillator strengths are the same for all three. The absorption maximum for the $\tilde{B}$–$\tilde{X}$ transition of CH_2OO is ~343 nm, and via the reflection principle can be considered to approximate the vertical excitation energy (3.61 eV). The EOM-CCSD calculations predict

Table 2.4 EOM-CCSD/aug-cc-pVTZ calculations characterizing the $\tilde{B}^1A'$–$\tilde{X}^1A'$ transitions of the Criegee intermediates CH_2OO and CHClOO. Calculated (observed) wavelengths of the origin, λ_{origin}, the band maximum, λ_{max}, based on vertical excitation energies, and the oscillator strengths, *f*, are shown.

	λ_{origin} / nm	λ_{max} / nm	*f*
CH_2OO	343 (431)	314 (~343)	0.153
syn-ClCHOO	324 (<420 nm)	298 (<345)	0.159
anti-ClCHOO	368	335	0.158

a vertical excitation energy that is around a third of an eV too high for CH_2OO. Assuming the same offset for ClCHOO, we predict respective absorption maxima of 324 nm and 368 nm for the *syn*-ClCHOO and *anti*-ClCHOO conformers. While the band maximum is not directly observed in our measurements, it clearly must lie at $\lambda < 345$ nm, implying that the spectrum is predominantly that of the *syn*-ClCHOO conformer. The wavelength for the band maximum predicted for *anti*-ClCHOO lies within the spectral range examined, but the band appears not to extend far enough to the red. *syn*-ClCHOO is predicted to be lower in energy by 0.07 eV at the CCSD/aug-cc-pVTZ level (including zero-point corrections), consistent with the value obtained by Cabezas *et al*. at the CCSD(T)-F12/aug-cc-PVTZ level.[49] It is not clear why such a small energy difference would lead to formation of the *syn* conformer being favored in a room temperature sample.

2.5 Atmospheric implications

The CHI_2Cl absorption spectrum overlaps significantly with the solar spectrum. The photolysis rate has been calculated using the equation:

$$J = \int F(\lambda)\sigma(\lambda)\phi(\lambda)d\lambda$$

where $F(\lambda)$ is the actinic flux at sea-level, $\sigma(\lambda)$ is the absorption cross section of CHI_2Cl. The photolysis quantum yield $\phi(\lambda)$ is assumed to be unity at all wavelengths. The actinic flux at a solar zenith angle of 0° is shown alongside the CHI_2Cl spectrum in Figure 2-1. The photolysis rate has been calculated at the seawater surface for solar zenith angles between 0° and 60°, assuming an 80% albedo.[89] The values range from $(1.6–0.8)\times10^{-2}$ s^{-1} yielding lifetimes of 1–2 minutes. These values are around half of that calculated for CH_2I_2,[16] and are primarily due to the absorption spectrum extending to longer wavelengths and overlapping better with the solar spectrum, which compensates for the apparent decrease in the maximum absorption cross section of the A and B bands. Reactive sinks in the marine boundary layer are likely to be Cl and OH radicals. The lifetime of CH_2I_2 due to reaction with either Cl and OH radicals is estimated to be 46 and 62 hours, respectively.[90,91] If the reactivity for CHI_2Cl is similar to that of CH_2I_2, photolysis is likely to be the major gas-phase sink for CHI_2Cl produced in surface seawater.

Photolysis of CHI_2Cl leads to the formation of internally excited CHICl radicals and I/I* atom products. The role of I atom chemistry in the troposphere has been investigated extensively.[2,3] Haloalkyl fragments also play a role in atmospheric chemistry as they are

generally thought to form peroxy radicals after reacting with O_2.[37] As with the CH_2I radical, reaction of the CHICl radical with O_2 appears to forms a carbonyl oxide or Criegee intermediate in comparably high yield. Pressure-dependent measurements of the $CH_2I + O_2$ reaction indicate a CH_2OO yield of 77% at 15 Torr (the pressure used in the measurement of the ClCHOO absorption cross section), decreasing to around 30% at atmospheric pressure.[40] It is difficult to estimate how much CHI_2Cl is present in the MBL due to its incredibly short lifetime and lack of field measurements. Carpenter *et al.* found that of the haloalkanes released by brown algae from Mace Head, Ireland, a maximum of 14% was CHI_2Cl compared to 35% CH_2I_2 and 51% CH_3I.[4] Additional measurements based on flux rates from the reactions between iodide, dissolved organic matter, and ozone, show that CHI_2Cl reaches a maximum of 6% of total haloalkane, when the production of CH_2I_2 and CH_3I are minimal.[6] Although only a small amount of CHI_2Cl is likely to be present in the MBL, the most probable removal mechanism is photolysis.

2.6 Conclusions

CHI_2Cl has been synthesized and the UV absorption spectrum measured. The spectrum is qualitatively like that of CH_2I_2, but is shifted to longer wavelengths and it is likely that photolysis will be the dominant removal mechanism during daylight hours in the MBL. The photodissociation dynamics of CHI_2Cl has been investigated in detail at several wavelengths spanning the first three absorption bands using DC slice velocity-map imaging. Images of I and I* atoms, detected using single-photon VUV ionization and 2+1 REMPI, show that the available energy is mainly partitioned into internal excitation of the CHICl radical co-fragment. Analysis of the wavelength dependence of the total translational energy release

results in a bond dissociation energy of 1.73 eV, which is weaker than typical C–I bond strengths. Anisotropy parameters extracted from the angular distributions approach the limiting value of +2 for a parallel transition, indicating prompt dissociation via excited states of A″ symmetry. High-level *ab initio* calculations support the assertion that transitions to states of A″ symmetry are primarily responsible for the features seen in the absorption spectrum. Reaction between CHICl and O_2 leads to the formation of a species that absorbs in the 345–440 nm wavelength range, that is assigned to the ClCHOO Criegee intermediate. Compared to CH_2OO, the presence of a chlorine atom shifts the peak of the absorption spectrum from ~343 nm to a predicted peak absorption of 324 nm for the *syn*-ClCHOO conformer.

2.7 Acknowledgements

We are grateful for support from AirUCI and the Laser Spectroscopy Facility, and to Scott Rychnovsky for allowing his laboratory to be used for synthesis of CHI_2Cl.

2.8 References

1 C. D. O'Dowd, J. L. Jimenez, R. Bahreini, R. C. Flagan, J. H. Seinfeld, K. Hämeri, L. Pirjola, M. Kulmala, S. G. Jennings and T. Hoffmann, Marine aerosol formation from biogenic iodine emissions, *Nature*, 2002, **417**, 632–636.

2 A. Saiz-Lopez, J. M. C. Plane, A. R. Baker, L. J. Carpenter, R. von Glasow, J. C. Gómez Martín, G. McFiggans and R. W. Saunders, Atmospheric Chemistry of Iodine, *Chem. Rev.*, 2012, **112**, 1773–1804.

3 L. J. Carpenter, Iodine in the Marine Boundary Layer, *Chem. Rev.*, 2003, **103**, 4953–4962.

4 L. J. Carpenter, G. Malin, P. S. Liss and F. C. Küpper, Novel biogenic iodine-containing trihalomethanes and other short-lived halocarbons in the coastal east Atlantic, *Global Biogeochem. Cy.*, 2000, **14**, 1191–1204.

5 A. R. Baker, C. Tunnicliffe and T. D. Jickells, Iodine speciation and deposition fluxes from the marine atmosphere, *J. Geophys. Res. Atmos.*, 2001, **106**, 28743–28749.

6 M. Martino, G. P. Mills, J. Woeltjen and P. S. Liss, A new source of volatile organoiodine compounds in surface seawater, *Geophys. Res. Lett.*, , DOI:10.1029/2008GL036334.

7 S. H. Gardiner, M. L. Lipciuc, T. N. V. Karsili, M. N. R. Ashfold and C. Vallance, Dynamics of the A-band ultraviolet photodissociation of methyl iodide and ethyl iodide via velocity-map imaging with 'universal' detection, *Phys. Chem. Chem. Phys.*, 2015, **17**, 4096–4106.

8 M. Kawasaki, S. J. Lee and R. Bersohn, Photodissociation of molecular beams of methylene iodide and iodoform, *J. Chem. Phys.*, 1975, **63**, 809–814.

9 G. Schmitt and F. J. Comes, Photolysis of CH_2I_2 and 1,1-$C_2H_4I_2$ at 300 nm, *J. Photochem.*, 1980, **14**, 107–123.

10 D. Senapati, K. Kavita and P. K. Das, Photodissociation Dynamics of CH_2ICl at 222, 236, 266, 280, and ~304 nm, *J. Phys. Chem. A*, 2002, **106**, 8479–8482.

11 D. Senapati and P. K. Das, $Cl^*(^2P_{1/2})$ production dynamics from chloroiodomethane (CH_2ICl) in the ultraviolet, *Chem. Phys. Lett.*, 2004, **393**, 535–538.

12 C.-H. Zhang, Y. Zhang, S. Zhang and B. Zhang, Photodissociation Dynamics of Chloroiodomethane in the A-Band, *Acta Physico-Chimica Sinica*, 2009, **25**, 1708–1712.

13 M. Cheng, D. Lin, L. Hu, Y. Du and Q. Zhu, Photodissociation dynamics of $ICH_2Cl \rightarrow CH_2Cl + I^*/I$: photofragment translational spectroscopy at 304 and 277 nm, *Phys. Chem. Chem. Phys.*, 2016, **18**, 3165–3172.

14 S. J. Lee and R. Bersohn, Photodissociation of a molecule with two chromophores. Bromoiodomethane, *J. Phys. Chem.*, 1982, **86**, 728–730.

15 L. J. Butler, E. J. Hintsa, S. F. Shane and Y. T. Lee, The electronic state-selective photodissociation of CH_2BrI at 248, 210, and 193 nm, *J. Chem. Phys.*, 1987, **86**, 2051–2074.

16 J. C. Mössinger, D. E. Shallcross and R. A. Cox, UV-VIS absorption cross-sections and atmospheric lifetimes of CH_2Br_2, CH_2I_2 and CH_2BrI, *J. Chem. Soc., Faraday Trans.*, 1998, **94**, 1391–1396.

17 C. M. Roehl, J. B. Burkholder, G. K. Moortgat, A. R. Ravishankara and P. J. Crutzen, Temperature dependence of UV absorption cross sections and atmospheric implications of several alkyl iodides, *J. Geophys. Res.*, 1997, **102**, 12819–12829.
18 B. W. Toulson, J. P. Alaniz, J. G. Hill and C. Murray, Near-UV photodissociation dynamics of CH_2I_2, *Phys. Chem. Chem. Phys.*, 2016, **18**, 11091–11103.
19 Y.-J. Liu, L. De Vico, R. Lindh and W.-H. Fang, Spin-Orbit Ab Initio Investigation of the Ultraviolet Photolysis of Diiodomethane, *ChemPhysChem*, 2007, **8**, 890–898.
20 S. L. Baughcum and S. R. Leone, Photofragmentation infrared emission studies of vibrationally excited free radicals CH_3 and CH_2I, *J. Chem. Phys.*, 1980, **72**, 6531–6545.
21 J. B. Koffend and S. R. Leone, Tunable laser photodissociation: quantum yield of $I^*(^2P_{1/2})$ from CH_2I_2, *Chem. Phys. Lett.*, 1981, **81**, 136–141.
22 T. F. Hunter and K. S. Kristjansson, Yield of $I(^2P_{1/2})$ in the photodissociation of CH_2I_2, *Chem. Phys. Lett.*, 1982, **90**, 35–40.
23 K.-W. Jung, T. S. Ahmadi and M. A. El-Sayed, Photofragment Translational Spectroscopy of CH_2I_2 at 304 nm: Polarization Dependence and Energy Partitioning, *B. Korean Chem. Soc.*, 1997, **18**, 1274–1280.
24 H. Xu, Y. Guo, S. Liu, X. Ma, D. Dai and G. Sha, Photodissociation dynamics of CH_2I_2 molecules in the ultraviolet range studied by ion imaging, *J. Chem. Phys.*, 2002, **117**, 5722–5729.
25 J. H. Lehman, H. Li and M. I. Lester, Ion imaging studies of the photodissociation dynamics of CH_2I_2 at 248 nm, *Chem. Phys. Lett.*, 2013, **590**, 16–21.
26 A. N. Tarnovsky, J.-L. Alvarez, A. P. Yartsev, V. Sundström and E. Åkesson, Photodissociation dynamics of diiodomethane in solution, *Chem. Phys. Lett.*, 1999, **312**, 121–130.
27 X. Zheng and D. L. Phillips, Photoisomerization reaction of CH_2BrI following *A*-band and *B*-band photoexcitation in the solution phase: Transient resonance Raman observation of the iso-CH_2I–Br photoproduct, *J. Chem. Phys.*, 2000, **113**, 3194–3203.
28 W. M. Kwok, C. Ma, A. W. Parker, D. Phillips, M. Towrie, P. Matousek, X. Zheng and D. L. Phillips, Picosecond time-resolved resonance Raman observation of the iso-CH_2Cl–I and iso-CH_2I–Cl photoproducts from the "photoisomerization" reactions of CH_2ICl in the solution phase, *J. Chem. Phys.*, 2001, **114**, 7536–7543.
29 A. N. Tarnovsky, V. Sundström, E. Åkesson and T. Pascher, Photochemistry of Diiodomethane in Solution Studied by Femtosecond and Nanosecond Laser Photolysis. Formation and Dark Reactions of the CH_2I–I Isomer Photoproduct and Its Role in Cyclopropanation of Olefins, *J. Phys. Chem. A*, 2004, **108**, 237–249.
30 K. Saitow, Y. Naitoh, K. Tominaga and K. Yoshihara, Photodissociation of CH_2I_2 and Subsequent Electron Transfer in Solution, *Chem. Asian J.*, 2008, **3**, 696–709.
31 R. Criegee, Mechanism of Ozonolysis, *Angew. Chem. Int. Ed.*, 1975, **14**, 745–752.
32 S. Hatakeyama and H. Akimoto, Reactions of criegee intermediates in the gas phase, *Res. Chem. Intermediat.*, 1994, **20**, 503–524.
33 D. Johnson and G. Marston, The gas-phase ozonolysis of unsaturated volatile organic compounds in the troposphere, *Chem. Soc. Rev.*, 2008, **37**, 699–716.

34 C. A. Taatjes, D. E. Shallcross and C. J. Percival, Research frontiers in the chemistry of Criegee intermediates and tropospheric ozonolysis, *Phys. Chem. Chem. Phys.*, 2014, **16**, 1704–1718.
35 D. L. Osborn and C. A. Taatjes, The physical chemistry of Criegee intermediates in the gas phase, *Int. Rev. Phys. Chem.*, 2015, **34**, 309–360.
36 O. Welz, J. D. Savee, D. L. Osborn, S. S. Vasu, C. J. Percival, D. E. Shallcross and C. A. Taatjes, Direct Kinetic Measurements of Criegee Intermediate (CH_2OO) Formed by Reaction of CH_2I with O_2, *Science*, 2012, **335**, 204–207.
37 A. J. Eskola, D. Wojcik-Pastuszka, E. Ratajczak and R. S. Timonen, Kinetics of the reactions of CH_2Br and CH_2I radicals with molecular oxygen at atmospheric temperatures, *Phys. Chem. Chem. Phys.*, 2006, **8**, 1416–1424.
38 H. Huang, A. J. Eskola and C. A. Taatjes, Pressure-Dependent I-Atom Yield in the Reaction of CH_2I with O_2 Shows a Remarkable Apparent Third-Body Efficiency for O_2, *J. Phys. Chem. Lett.*, 2012, **3**, 3399–3403.
39 D. Stone, M. Blitz, L. Daubney, T. Ingham and P. Seakins, CH_2OO Criegee biradical yields following photolysis of CH_2I_2 in O_2, *Phys. Chem. Chem. Phys.*, 2013, **15**, 19119.
40 W.-L. Ting, C.-H. Chang, Y.-F. Lee, H. Matsui, Y.-P. Lee and J. J.-M. Lin, Detailed mechanism of the $CH_2I + O_2$ reaction: Yield and self-reaction of the simplest Criegee intermediate CH_2OO, *J. Chem. Phys.*, 2014, **141**, 104308.
41 J. M. Beames, F. Liu, L. Lu and M. I. Lester, Ultraviolet Spectrum and Photochemistry of the Simplest Criegee Intermediate CH_2OO, *J. Am. Chem. Soc.*, 2012, **134**, 20045–20048.
42 L. Sheps, Absolute Ultraviolet Absorption Spectrum of a Criegee Intermediate CH_2OO, *J. Phys. Chem. Lett.*, 2013, **4**, 4201–4205.
43 W.-L. Ting, Y.-H. Chen, W. Chao, M. C. Smith and J. J.-M. Lin, The UV absorption spectrum of the simplest Criegee intermediate CH_2OO, *Phys. Chem. Chem. Phys.*, 2014, **16**, 10438–10443.
44 E. S. Foreman, K. M. Kapnas, Y. Jou, J. Kalinowski, D. Feng, R. B. Gerber and C. Murray, High resolution absolute absorption cross sections of the $\tilde{B}^1A'$–$\tilde{X}^1A'$ transition of the CH_2OO biradical, *Phys. Chem. Chem. Phys.*, 2015, **17**, 32539–32546.
45 J. M. Beames, F. Liu, L. Lu and M. I. Lester, UV spectroscopic characterization of an alkyl substituted Criegee intermediate CH_3CHOO, *J. Chem. Phys.*, 2013, **138**, 244307-244307–9.
46 F. Liu, J. M. Beames, A. M. Green and M. I. Lester, UV Spectroscopic Characterization of Dimethyl- and Ethyl-Substituted Carbonyl Oxides, *J. Phys. Chem. A*, 2014, **118**, 2298–2306.
47 H. Niki, P. D. Maker, C. M. Savage and L. P. Breitenbach, Atmospheric ozone-olefin reactions, *Environ. Sci. Technol.*, 1983, **17**, 312A-322A.
48 J. B. Burkholder, R. A. Cox and A. R. Ravishankara, Atmospheric Degradation of Ozone Depleting Substances, Their Substitutes, and Related Species, *Chem. Rev.*, 2015, **115**, 3704–3759.
49 C. Cabezas, J.-C. Guillemin and Y. Endo, Fourier-transform microwave spectroscopy of a halogen substituted Criegee intermediate ClCHOO, *J. Chem. Phys.*, 2016, **145**, 184304.

50 N. Kawabata, M. Tanimoto and S. Fujiwara, Synthesis of monohalocyclopropane derivatives from olefins by the reaction with trihalomethanes and copper, *Tetrahedron*, 1979, **35**, 1919–1923.
51 G. B. Jones and B. J. Chapman, in *Encyclopedia of Reagents for Organic Synthesis*, John Wiley & Sons, Ltd, 2001.
52 D. B. Li, S.-C. Ng and I. Novak, Novel synthetic approaches to CHBrFI, CHClFI and CHBrClI, *Tetrahedron*, 2002, **58**, 5923–5926.
53 E. S. Foreman, K. M. Kapnas and C. Murray, Reactions between Criegee Intermediates and the Inorganic Acids HCl and HNO_3 : Kinetics and Atmospheric Implications, *Angew. Chem. Int. Ed.*, 2016, **55**, 10419–10422.
54 T. B. Adler, G. Knizia and H.-J. Werner, A simple and efficient CCSD(T)-F12 approximation, *J. Chem. Phys.*, 2007, **127**, 221106.
55 G. Knizia, T. B. Adler and H.-J. Werner, Simplified CCSD(T)-F12 methods: Theory and benchmarks, *J. Chem. Phys.*, 2009, **130**, 054104.
56 K. A. Peterson, T. B. Adler and H.-J. Werner, Systematically convergent basis sets for explicitly correlated wavefunctions: The atoms H, He, B–Ne, and Al–Ar, *J. Chem. Phys.*, 2008, **128**, 084102.
57 J. G. Hill and K. A. Peterson, Correlation consistent basis sets for explicitly correlated wavefunctions: Pseudopotential-based basis sets for the post-d main group elements Ga–Rn, *J. Chem. Phys.*, 2014, **141**, 094106.
58 K. A. Peterson, B. C. Shepler, D. Figgen and H. Stoll, On the Spectroscopic and Thermochemical Properties of ClO, BrO, IO, and Their Anions, *J. Phys. Chem. A*, 2006, **110**, 13877–13883.
59 S. Kritikou and J. G. Hill, Auxiliary Basis Sets for Density Fitting in Explicitly Correlated Calculations: The Atoms H–Ar, *J. Chem. Theory Comput.*, 2015, **11**, 5269–5276.
60 K. E. Yousaf and K. A. Peterson, Optimized auxiliary basis sets for explicitly correlated methods, *J. Chem. Phys.*, 2008, **129**, 184108.
61 E. F. Valeev, Improving on the resolution of the identity in linear R12 ab initio theories, *Chem. Phys. Lett.*, 2004, **395**, 190–195.
62 T. Shiozaki and H.-J. Werner, Communication: Second-order multireference perturbation theory with explicit correlation: CASPT2-F12, *J. Chem. Phys.*, 2010, **133**, 141103.
63 T. Shiozaki, G. Knizia and H.-J. Werner, Explicitly correlated multireference configuration interaction: MRCI-F12, *J. Chem. Phys.*, 2011, **134**, 034113.
64 T. Shiozaki and H.-J. Werner, Explicitly correlated multireference configuration interaction with multiple reference functions: Avoided crossings and conical intersections, *J. Chem. Phys.*, 2011, **134**, 184104.
65 E. R. Davidson and D. W. Silver, Size consistency in the dilute helium gas electronic structure, *Chem. Phys. Lett.*, 1977, **52**, 403–406.
66 T. H. Dunning Jr., Gaussian basis sets for use in correlated molecular calculations. I. The atoms boron through neon and hydrogen, *J. Chem. Phys.*, 1989, **90**, 1007–1023.
67 T. H. Dunning, K. A. Peterson and A. K. Wilson, Gaussian basis sets for use in correlated molecular calculations. X. The atoms aluminum through argon revisited, *J. Chem. Phys.*, 2001, **114**, 9244–9253.

68 H.-J. Werner, P. J. Knowles, G. Knizia, F. R. Manby and M. Schütz, Molpro: a general-purpose quantum chemistry program package, *Comput. Mol. Sci.*, 2012, **2**, 242–253.
69 *MOLPRO, version 2015.1, a package of ab initio programs, H.-J. Werner, P. J. Knowles, G. Knizia, F. R. Manby, M. Schütz, P. Celani, W. Györffy, D. Kats, T. Korona, R. Lindh, A. Mitrushenkov, G. Rauhut, K. R. Shamasundar, T. B. Adler, R. D. Amos, A. Bernhardsson, A. Berning, D. L. Cooper, M. J. O. Deegan, A. J. Dobbyn, F. Eckert, E. Goll, C. Hampel, A. Hesselmann, G. Hetzer, T. Hrenar, G. Jansen, C. Köppl, Y. Liu, A. W. Lloyd, R. A. Mata, A. J. May, S. J. McNicholas, W. Meyer, M. E. Mura, A. Nicklass, D. P. O'Neill, P. Palmieri, D. Peng, K. Pflüger, R. Pitzer, M. Reiher, T. Shiozaki, H. Stoll, A. J. Stone, R. Tarroni, T. Thorsteinsson, and M. Wang, see http://www.molpro.net.*, .
70 I. Novak, D. B. Li, A. W. Potts, A. Shareef and B. Kovač, Halogen−Halogen Interactions in Halomethanes, *J. Org. Chem.*, 2002, **67**, 3510–3513.
71 W. von Niessen, L. Åsbrink and G. Bieri, 30.4 nm He (II) photoelectron spectra of organic molecules Part VI. Halogeno-compounds (C, H, X; X = Cl, Br, I), *J. Electron. Spectrosc.*, 1982, **26**, 173–201.
72 H. Fan and S. T. Pratt, Determination of Spin−Orbit Branching Fractions in the Photodissociation of Halogenated Hydrocarbons, *J. Phys. Chem. A*, 2007, **111**, 3901–3906.
73 S. H. Gardiner, M. L. Lipciuc, T. N. V. Karsili, M. N. R. Ashfold and C. Vallance, Dynamics of the A-band ultraviolet photodissociation of methyl iodide and ethyl iodide via velocity-map imaging with 'universal' detection, *Phys. Chem. Chem. Phys.*, 2015, **17**, 4096–4106.
74 A. F. Lago, J. P. Kercher, A. Bödi, B. Sztáray, B. Miller, D. Wurzelmann and T. Baer, Dissociative Photoionization and Thermochemistry of Dihalomethane Compounds Studied by Threshold Photoelectron Photoion Coincidence Spectroscopy, *J. Phys. Chem. A*, 2005, **109**, 1802–1809.
75 G. E. Busch and K. R. Wilson, Triatomic Photofragment Spectra. I. Energy Partitioning in NO_2 Photodissociation, *J. Chem. Phys.*, 1972, **56**, 3626–3638.
76 B. J. Ratliff, C. C. Womack, X. N. Tang, W. M. Landau, L. J. Butler and D. E. Szpunar, Modeling the Rovibrationally Excited C_2H_4OH Radicals from the Photodissociation of 2-Bromoethanol at 193 nm, *J. Phys. Chem. A*, 2010, **114**, 4934–4945.
77 B. G. McKown, M. Ceriotti, C. C. Womack, E. Kamarchik, L. J. Butler and J. M. Bowman, Effects of High Angular Momentum on the Unimolecular Dissociation of CD_2CD_2OH: Theory and Comparisons with Experiment, *J. Phys. Chem. A*, 2013, **117**, 10951–10963.
78 Z. Kisiel, *Principal Moments of Inertia From STructure*, .
79 A. V. Demyanenko, V. Dribinski, H. Reisler, H. Meyer and C. X. W. Qian, Product quantum-state-dependent anisotropies in photoinitiated unimolecular decomposition, *J. Chem. Phys.*, 1999, **111**, 7383.
80 S. Bailleux, P. Kania, J. Skřínský, T. Okabayashi, M. Tanimoto, S. Matsumoto and H. Ozeki, Hyperfine Resolved Fourier Transform Microwave and Millimeter-Wave Spectroscopy of the Iodomethyl Radical, CH_2I ($\tilde{X}^2B_1$), *J. Phys. Chem. A*, 2010, **114**, 4776–4784.
81 Y. Endo, S. Saito and E. Hirota, The microwave spectrum of the chloromethyl radical, CH_2Cl, *Can. J. Phys.*, 1984, **62**, 1347–1360.

82 W. G. Merrill, F. F. Crim and A. S. Case, Dynamics and yields for $CHBrCl_2$ photodissociation from 215–265 nm, *Phys. Chem. Chem. Phys.*, 2016, **18**, 32999–33008.
83 E. S. Foreman and C. Murray, Kinetics of IO Production in the $CH_2I + O_2$ Reaction Studied by Cavity Ring-Down Spectroscopy, *J. Phys. Chem. A*, 2015, **119**, 8981–8990.
84 A. W.-L. Ting and J. J.-M. Lin, UV Spectrum of the Simplest Deuterated Criegee Intermediate CD_2OO, *J. Chin. Chem. Soc.*, 2017, **64**, 360–368.
85 R. Dawes, B. Jiang and H. Guo, UV Absorption Spectrum and Photodissociation Channels of the Simplest Criegee Intermediate (CH_2OO), *J. Am. Chem. Soc.*, 2015, **137**, 50–53.
86 J. Kalinowski, E. S. Foreman, K. M. Kapnas, C. Murray, M. Räsänen and R. B. Gerber, Dynamics and spectroscopy of CH_2OO excited electronic states, *Phys. Chem. Chem. Phys.*, 2016, **18**, 10941–10946.
87 M. C. Smith, W.-L. Ting, C.-H. Chang, K. Takahashi, K. A. Boering and J. J.-M. Lin, UV absorption spectrum of the C2 Criegee intermediate CH_3CHOO, *J. Chem. Phys.*, 2014, **141**, 074302.
88 Y.-P. Chang, C.-H. Chang, K. Takahashi and J. J.-M. Lin, Absolute UV absorption cross sections of dimethyl substituted Criegee intermediate $(CH_3)_2COO$, *Chem. Phys. Lett.*, 2016, **653**, 155–160.
89 B. J. Finlayson-Pitts and J. N. Pitts, *Chemistry of the upper and lower atmosphere: theory, experiments, and applications*, Academic Press, San Diego, 2000.
90 S. Zhang, R. Strekowski, L. Bosland, A. Monod and C. Zetzsch, Kinetic study of the reaction of OH with CH_2I_2, *Phys. Chem. Chem. Phys.*, 2011, **13**, 11671.
91 S. Enami, S. Hashimoto, M. Kawasaki, Y. Nakano, T. Ishiwata, K. Tonokura and T. J. Wallington, Observation of Adducts in the Reaction of Cl Atoms with XCH_2I (X = H, CH_3, Cl, Br, I) Using Cavity Ring-Down Spectroscopy, *J. Phys. Chem. A*, 2005, **109**, 1587–1593.

3 UV Photofragmentation Dynamics of Acetaldehyde Cations Prepared by Single-Photon VUV Ionization

This work is reproduced from Kapnas, K. M., McCaslin, L. M., & Murray, C. *Phys. Chem. Chem. Phys.* **2019**, DOI: 10.1039/C8CP06640J, Advance Article by permission from the Royal Society of Chemistry.

3.1 Abstract

Acetaldehyde cations (CH_3CHO^+) were prepared using single-photon vacuum ultraviolet ionization of CH_3CHO in a molecular beam and the fragmentation dynamics explored over the photolysis wavelength range 390–210 nm using velocity-map ion imaging and photofragment yield (PHOFY) spectroscopy. Four fragmentation channels are characterized:

$$CH_3CHO^+ \rightarrow C_2H_3O^+ + H \quad \text{I}$$

$$CH_3CHO^+ \rightarrow HCO^+ + CH_3 \quad \text{II}$$

$$CH_3CHO^+ \rightarrow CH_3^+ + HCO \quad \text{III}$$

$$CH_3CHO^+ \rightarrow CH_4^+ + CO \quad \text{IV}$$

Channels I, II, and IV are observed across the full photolysis wavelength range while channel III is observed only at $\lambda < 317$ nm. Maximum fragment ion yields are obtained at ~250 nm. Ion images were recorded over the range 316–228 nm, which corresponds to initial

excitation to the $\tilde{B}^2A'$ and $\tilde{C}^2A'$ states of CH_3CHO^+. The speed and angular distributions are distinctly different for each detected ion and show evidence of both statistical and dynamical fragmentation pathways. At longer wavelengths, fragmentation via channel I leads to modest translational energies (E_T), consistent with dissociation over a small barrier and production of highly internally excited CH_3CO^+. Additional components with E_{INT} greater than the CH_3CO^+ secondary dissociation threshold appear at shorter wavelengths and are assigned to fragmentation products of vinyl alcohol cation or oxirane cation formed by isomerization of energized CH_3CHO^+. The E_T distribution observed for channel III products peaks at zero but is notably colder than that predicted by phase space theory, particularly at longer photolysis wavelengths. The colder-than-statistical E_T distributions are attributed to contributions from secondary fragmentation of energized CH_3CO^+ formed via channel I, which are attenuated by CH_3CHO^+ isomerization at shorter wavelengths. Fragmentation via channels II and IV results in qualitatively similar outcomes, with evidence of isotropic statistical components at low-E_T and anisotropic components due to excited state dynamics at higher E_T.

3.2 Introduction

Molecules, radicals, and ions are ubiquitous in interstellar space, with several neutral complex organic molecules (COMs) having been observed.[1] Depending on the interstellar environment, COMs have the potential to be ionized *via* charge transfer reactions or cosmic radiation.[2] The ultraviolet and vacuum ultraviolet (UV and VUV) radiation fields produced by surrounding stars have the potential to both rapidly ionize and dissociate these molecules.[3] One such COM that could be relevant in interstellar space is acetaldehyde cation,

CH_3CHO^+, whose neutral counterpart has been detected in numerous interstellar environments.[4–9] The photochemistry of CH_3CHO^+ is consequently of fundamental interest and potential astrochemical relevance.

The photofragmentation dynamics of molecular cations has attracted attention over the last few decades, with velocity-map imaging proving to be a particularly effective tool for detailed examination. Most studies have used resonance-enhanced multiphoton ionization (REMPI) to state-selectively prepare cations, with absorption of an additional photon of the same wavelength inducing fragmentation. Ashfold and co-workers have used this approach to examine the photochemistry of the cations of diatomic halogens and interhalogens,[10–12] alkyl halides,[13] and first-row hydrides.[14,15] Suits and co-workers have examined the photochemistry of several aldehyde,[16–18] amine,[19,20] and alkene cations;[21,22] their work on cation photofragmentation using imaging techniques has been summarized in a mini-review.[23] Single-photon VUV ionization at 118 nm has also been used to prepare acetone cations, with photofragmentation induced by the residual 355 nm radiation used in VUV generation.[24] From a mass spectrometry perspective, polyatomic ions are thought primarily to fragment statistically, according to the quasi-equilibrium theory in which the energy is assumed to be completely randomized among internal degrees of freedom prior to fragmentaion.[25,26] Examples demonstrating the involvement of excited states in the fragmentation of molecular cations are few.[13,15,16,19]

Information about the electronic states and energy-dependent fragmentation of CH_3CHO^+ comes largely from photoelectron spectroscopy and photoelectron/photoion coincidence (PEPICO) measurements. He I and threshold photoelectron spectra of acetaldehyde show an

intense, sharp 0-0 band near 10.29 eV,[27–31] indicative of ionization from the non-bonding n_O (10a′) orbital. Production of vibrationally excited ions is limited to single quanta in the CH_3 deformation/CC stretch (ν_7) and CH bend (ν_6) modes. Several diffuse bands corresponding to various excited states of the cation are observed at higher photoelectron kinetic energies. Only the Ã band at ~13.1 eV shows vibrational structure, with progressions in the CO stretch (ν_4) and CCO bend (ν_{10}) that are consistent with the ejection of an electron from the $\pi_{C=O}$ (2a″) bonding orbital. The B̃ and C̃ bands at ~13.9 eV and 15.2 eV are assigned to ionization from the π_{CH_3} (9a′) and σ_{C-C} (8a′) orbitals, respectively. A summary of the band assignments, characters, and excitation energies as reported in the most recent work by Yencha *et al*.[31] can be found in Table 3.1.

Table 3.1 Summary of CH_3CHO^+ electronic states and ejected electron characters. Experimental vertical ionization energies (IE) are taken from the photoelectron spectroscopy work of Yencha *et al*.[31] and calculated values are at the EOM-CC(2,3)/cc-pVTZ level. Threshold wavelengths for excitation are relative to the ground state of the ion.

State	Character	Expt. IE [Calc. IE]/ eV	λ / nm
$\tilde{X}^2A'$	n_O (10a′)	10.228 [10.574]	
$\tilde{A}^2A''$	$\pi_{C=O}$ (2a′)	13.09 [13.651]	403
$\tilde{B}^2A'$	π_{CH_3} (9a′)	13.93 [14.818]	292
$\tilde{C}^2A'$	σ_{C-C} (8a′)	15.20 [15.606]	246
$\tilde{D}^2A'$	π_{CH_3} (1a″)	15.5 [16.095]	225

PEPICO measurements have mapped out breakdown curves showing the fragmentation as a function of VUV wavelength, up to excitation energies ~7 eV above the ionization energy.[29,30]

Four major fragmentation channels have been identified in the PEPICO studies:

$$CH_3CHO^+ \rightarrow C_2H_3O^+ + H \qquad \text{I}$$

$$CH_3CHO^+ \rightarrow HCO^+ + CH_3 \qquad \text{II}$$

$$CH_3CHO^+ \rightarrow CH_3^+ + HCO \qquad \text{III}$$

$$CH_3CHO^+ \rightarrow CH_4^+ + CO \qquad \text{IV}$$

Thermodynamic threshold energies and appearance energies for fragmentation channels I–IV are compiled in Table 3.2 and illustrated in Figure 3-1. In general, appearance energies are slightly greater than the thermodynamic thresholds. From the onset of the $\tilde{A}^2A''$ band,

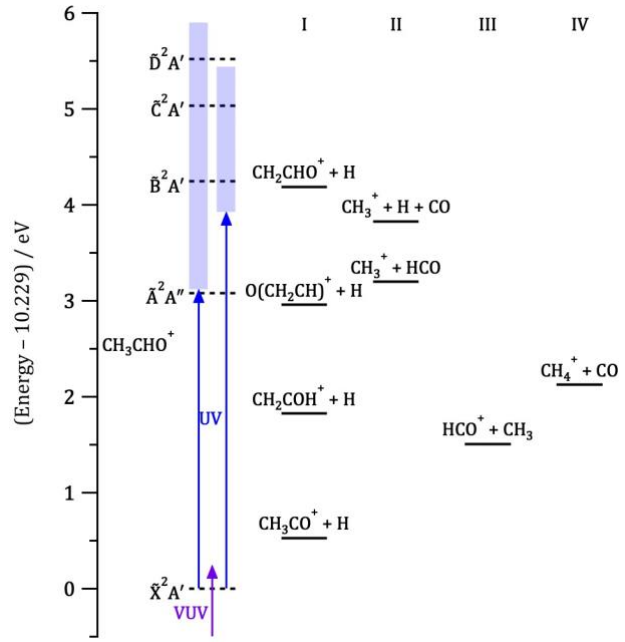

Figure 3-1 Schematic energy diagram for acetaldehyde cation photolysis. The shaded blue regions represent the photolysis wavelengths used for photofragment ion yield spectra (390–210 nm) and for ion images (316–228 nm). Excited state vertical excitation energies (dashed) are from EOM-CC(2,3)/cc-pVTZ calculations.

channels I and II are thought to proceed on the ground state following internal conversion.[29,30] Channel III products have an appearance energy of 14.1 eV, near the onset of the B̃ band in the photoelectron spectrum.[29,30] Johnson *et al*. suggested that CH_3^+ production resulted from secondary fragmentation of $C_2H_3O^+$, based upon the observation that the $C_2H_3O^+$ translational energy distributions deviated from a simple statistical model when an excess energy > 3.6 eV was reached.[30] Channel IV products CH_4^+ + CO were observed at photon energies greater than 13 eV in the PEPICO studies of Johnson *et al*.[30] and were associated with dissociation on the Ã $^2A''$ surface. Bombach *et al.*[29] did not observe CH_4^+ formation, however. Photoionization mass spectrometry (PIMS) measurements by Jochims *et al*.[32] identified hydrogen scrambling in the fragments from partially-deuterated isotopologues CD_3CHO and CH_3CDO following excitation using wavelength-tunable

Table 3.2 Dissociation energies (D_0), appearance energies (AE), and threshold wavelengths(λ_{th}) for various fragment ions.[32] D_0 values are calculated from 0 K thermodynamic data obtained from the Active Thermochemical Tables (ATcT).[47] Uncertainties are < 8 meV. Appearance energies, AE and ΔAE, are from Jochims *et al*.[32] Also shown in parentheses are ΔD_0 and ΔAE, the dissociation and appearance energies relative to the zero-point level of CH_3CHO^+.

Ion	D_0 (ΔD_0)/ eV	λ_{th} / nm	AE (ΔAE) / eV	λ_{th} / nm
$C_2H_3O^+$	10.758 (0.528)	2348	10.90 (0.67)	1850
HCO^+	11.739 (1.510)	821	12.03 (1.80)	689
CH_4^+	12.356 (2.126)	583	12.61 (2.38)	521
CH_3^+	13.429 (3.200)	387	14.08 (3.85)	322
CO^+	13.751 (3.521)	352	–	–

synchrotron radiation, consistent with statistical dissociation on the ground state surface. Substantial fragmentation and hydrogen scrambling has also been observed in 2+1 REMPI spectroscopy via the 3s Rydberg state at wavelengths near 360 nm.[33–35] It was concluded that dissociation resulted from excitation of the ion to the $\tilde{B}^2A'$state. Using the same REMPI transition, Lee *et al*.[16] used velocity-map ion imaging to detect the CH_3CO^+, HCO^+, and CH_4^+ ionic fragments, measuring their translational energy and angular distributions. The observations were generally consistent with excitation to the $\tilde{B}^2A'$ state, with dissociation occurring on the ground state surface. The CH_3CO^+ angular distributions required higher order Legendre polynomial terms, indicating that the ionization process resulted in spatial alignment of the CH_3CHO^+ cations prior to dissociation.

In this paper, we present the results of velocity-map ion imaging experiments characterizing the wavelength-dependent photofragmentation dynamics of the acetaldehyde cation, CH_3CHO^+. Production of CH_3CHO^+ by single-photon VUV ionization allows photolysis of the cation to be probed over a broad range of excitation wavelengths, unlike studies that use REMPI to prepare the parent cation, which are restricted by the resonant step. Photofragment ion yield spectra have been recorded over the wavelength range 390–210 nm and branching fractions for the major products $C_2H_3O^+$, HCO^+, CH_3^+, and CH_4^+ have been determined. Ion images characterizing the photodissociation dynamics have been measured between 228 nm and 316 nm. The images show evidence of both statistical and dynamical fragmentation mechanisms. Comparisons are drawn with previous one-color measurements of CH_3CHO^+ fragmentation using both direct single-photon VUV ionization and REMPI techniques.

3.3 Experimental and Computational Methods

The experimental methods were identical to those used in our recent studies of the UV photochemistry of acetaldehyde and acetone,[36,37] combining photofragment ion yield (PHOFY) spectroscopy and velocity-map ion imaging using VUV ionization to detect products. In these experiments, the time ordering of the UV and VUV laser pulses was simply reversed such that acetaldehyde cations are first formed by the VUV ionization pulse and subsequently dissociated by the UV photolysis pulse. Briefly, a molecular beam of CH_3CHO seeded in Ar carrier gas (~30%) was intersected perpendicularly by counter-propagating ionization and photolysis beams. CH_3CHO^+ was prepared by single-photon VUV ionization at a wavelength of 118.2 nm (10.49 eV), which was generated by frequency tripling the 3rd harmonic of a Nd:YAG laser in a static Xe/Ar gas mixture.[38] A tunable mid-band optical parametric oscillator (OPO) pumped by a Nd:YAG laser (Continuum Horizon II and Surelite EX) generated UV pulses over the wavelength range of 390–210 nm with a linewidth of ~7 cm^{-1}. The time delay between the ionization and photolysis laser pulses was held at ~60 ns. The wavelength-dependent UV pulse energies were continuously monitored with an energy meter and ranged between 1–2 mJ. A stack of velocity-mapping electrodes accelerated ionic photofragments towards a position sensitive detector that comprised a fast-gated microchannel plate/phosphor screen assembly (Photonis) and CCD camera (Basler), while the total phosphorescence was collected with a silicon photomultiplier. Custom-written data acquisition software (National Instruments, LabVIEW) performed real-time centroiding and event-counting. Images were recorded using conventional velocity-map ion imaging, and analyzed using the polar onion-peeling approach.[39]

Ab initio electronic structure calculations were performed using QChem.[40] All excited state energies were calculated using the ionization potential variant of EOM-CC(2,3) from the restricted Hartree-Fock neutral singlet reference.[41] EOM-CC(2,3) includes single, double, and triple excitations for high-accuracy characterization of excited states. All oscillator strengths were calculated using the excitation energy variant of EOM-CCSD.[42] For all calculations, Dunning's cc-pVTZ basis set was employed.[43] The geometry of neutral acetaldehyde was calculated at the CCSD(T) level of theory.[44,45] All calculations were performed in the frozen core approximation.

3.4 Results

Time-of-flight mass spectra recorded with VUV only, UV only, and both VUV+UV pulses present are shown in Figure 3-2. Single-photon ionization at 118.2 nm yields a mass spectrum dominated by a single intense peak at 6.18 μs that corresponds to the acetaldehyde cation, CH_3CHO^+. Introduction of the UV beam after VUV ionization results in dissociation of CH_3CHO^+, as evidenced by a depletion of the m/z = 44 signal and the appearance of several new features at shorter flight times. The major ionic fragment is HCO^+ at a flight time of 5.06 μs, while additional features in the mass spectrum at 3.68 μs, 3.80 μs, and 6.12 μs are assigned to CH_3^+, CH_4^+, and $C_2H_3O^+$, respectively. The 308 nm UV beam produces a small non-resonant background signal that appears primarily at the parent mass. One-color background signals of similar relative magnitude were observed across the 210–400 nm UV wavelength range.

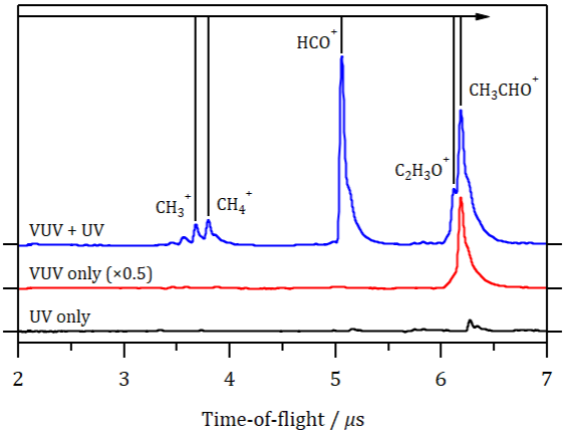

Figure 3-2 One-color and two-color time-of-flight mass spectra of CH_3CHO: (black) 308 nm UV photolysis pulse only; (red) 118.2 nm VUV ionization pulse only; (blue) both VUV + UV pulses. The time delay between the VUV and UV pulses was ~120 ns.

A well-known problem encountered when working with acetaldehyde expansions is cluster formation.[36,46] Acetaldehyde dimers, trimers, and larger clusters are also observable in the mass spectrum following ionization at 118.2 nm. Ion imaging measurements of CH_3 fragments produced by photolysis of the neutral molecule provide a more discriminating diagnostic; under cluster-free conditions, the image at 308 nm appears as a clean, isotropic ring at speeds of ~1700 m s^{-1}, while photolysis of clusters results in higher ion counts near the center. Cluster contributions were minimized by operating early in the gas expansion, albeit at the cost of smaller signal magnitudes and likely slightly poorer cooling.

3.4.1 Photofragment Yield Spectroscopy

Two-color VUV+UV time-of-flight mass spectra were recorded as the photolysis laser wavelength was scanned over the range 390–210 nm, corresponding to an excitation energy range of 3.18–5.90 eV and converted into the PHOFY spectra shown in Figure 3-3(a). The

excitation energy range is equivalent to 13.41–16.13 eV relative to the ground state of neutral CH_3CHO. PHOFY spectra were obtained by integrating the CH_3^+, CH_4^+, and HCO^+ and $C_2H_3O^+$ peaks in the mass spectra after subtraction of the one-color background signals. The spectra were subsequently normalized to correct for the reproducible wavelength dependence of the photolysis laser fluence. The ~300 ns phosphorescence lifetime of the detector, coupled with the short time delay between the laser pulses resulted in significant overlap of the one-color VUV-only parent ion signal at m/z = 44 and that of the two-color VUV+UV $C_2H_3O^+$ product signal at m/z = 43. Consequently, the $C_2H_3O^+$ yield spectrum is noisier than the others.

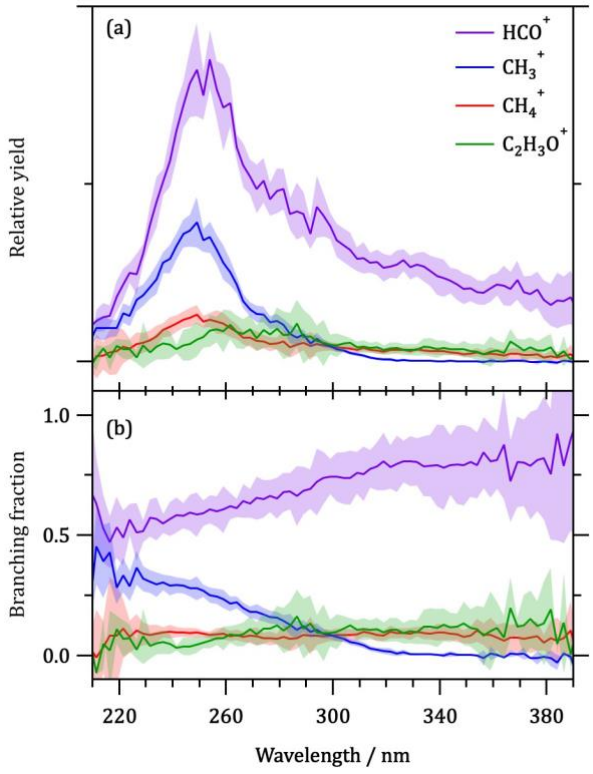

Figure 3-3 (a) CH_3CHO^+ PHOFY spectra recorded detecting $C_2H_3O^+$ (green), HCO^+ (purple), CH_4^+ (red), and CH_3^+ (blue); (b) branching fractions for each ionic photofragment.

CH_3^+ ions are observed only at $\lambda < 317$ nm, broadly consistent with the appearance energy (AE) for CH_3^+ of 14.08 eV (or 3.85 eV above the CH_3CHO^+ ground state, implying a threshold wavelength of 322 nm) determined in one-color photoelectron spectroscopy/PEPICO measurements.[32] In contrast, channel I, II, and IV ions have lower AEs (see Table 3.2) and are observed across the complete range of wavelengths spanned by the PHOFY spectra.[32] Despite the variation among the AEs, the spectra are remarkably similar, with maximum ion yields observed at 249 nm (4.98 eV). The 249 nm feature is most distinct in the CH_3^+ PHOFY spectrum, where it is accompanied by a shoulder at 289 nm (4.29 eV); the other fragment ion yields share these features. Features in the total PHOFY spectra, obtained by summing over all fragments, appear at wavelengths similar to those observed in photoelectron spectroscopy, as shown in Figure 3-4, although with very different relative intensities.

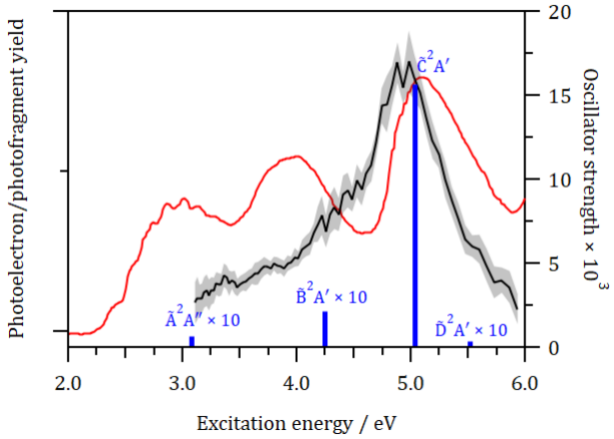

Figure 3-4 Total photofragment ion yield (black), photoelectron spectrum measured by Cvitaš *et al.*[28] (red), and oscillator strengths from EOM-CC(2,3)/cc-pVTZ calculations vs. vertical excitation energies (blue). Excitation energies are measured relative to the ground state of the CH_3CHO^+ cation; the photoelectron spectrum has been shifted by –10.23 eV.

The fragment ion yields can be used directly to determine the wavelength-dependent branching fractions shown in Figure 3-3(b), which is analogous to the breakdown curves presented in the PEPICO studies.[29,30] At $\lambda > 317$ nm, HCO^+ accounts for a fractional yield of ~0.8, with the remainder split equally between $C_2H_3O^+$ and CH_4^+. At $\lambda < 317$ nm the CH_3^+ channel opens and the subsequent increase in its branching fraction is mirrored by a decline in that of HCO^+, which reaches ~0.4 at 210 nm. The branching fractions for the minor CH_4^+ and $C_2H_3O^+$ channels remain effectively constant at ~0.1 across the photolysis wavelength range. The branching fractions are in good agreement with the 2+1 REMPI results of Lee *et al.*,[16] who reported fractional yields of 0.12, 0.73, and 0.15 for $C_2H_3O^+$, HCO^+, and CH_4^+ ions, respectively, at the REMPI wavelength of 363 nm. Averaged over the 346–371 nm range where the branching fractions are wavelength-independent, we find 0.12±0.03, 0.80±0.04, 0.08±0.04 for the same fragment ions (the CH_3^+ yield is zero at $\lambda > 317$ nm). At shorter wavelengths, the observed branching is broadly in agreement with the breakdown curve reported by Johnson *et al*.[30]

3.4.2 Ion Imaging

Ion images of CH_3^+, CH_4^+, HCO^+, and $C_2H_3O^+$ photofragments were collected at eleven photolysis wavelengths in the range 316–228 nm, corresponding to excitation energies spanning the range 3.92–5.44 eV (or 14.15–15.67 eV relative the ground state of neutral CH_3CHO). Representative ion images of the four major ionic photofragments resulting from photolysis of CH_3CHO^+ at photolysis wavelengths (316 nm, 276 nm, and 236 nm) are shown in Figure 3-5. The images are wavelength-dependent to varying degrees and characteristic of each ion; they will be discussed in turn below. Speed and angular distributions were

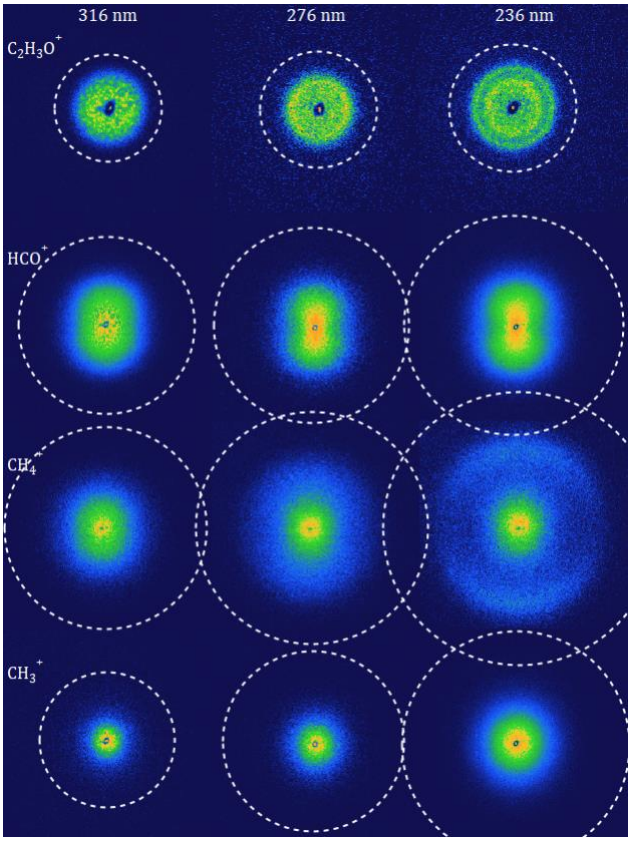

Figure 3-5 $C_2H_3O^+$, HCO^+, CH_4^+, and CH_3^+ ion images (top to bottom) following photolysis of CH_3CHO^+ at 316 nm, 276 nm, and 236 nm (left to right). Dashed circles represent the maximum possible speeds for each ionic fragment assuming the neutral co-fragments given in reactions I–IV. The $C_2H_3O^+$ images on the top row have been magnified by a factor of two to more clearly show the structure.

extracted from the ion images using the polar onion-peeling algorithm.[39] Speed distributions were converted into total translational energy distributions, $P(E_T)$, using the appropriate Jacobian transformation and the equation

$$E_T = \frac{1}{2} m_{ion} (1 + \frac{m_{ion}}{m_{neutral}}) v_{ion}^2$$

where m_{ion} and $m_{neutral}$ are the masses of the observed ion and undetected neutral fragment,

respectively. The total E_T distributions are the average of those obtained from at least three independently-measured ion images at each photolysis wavelength.

By conservation of energy, E_T is given by

$$E_T = E_{AVL} - E_{INT,fragments} + E_{INT,parent}$$

where the available energy, $E_{AVL} = h\nu - D_0$, is the difference between the photolysis photon energy and the dissociation energy for formation of the detected product ion and corresponding neutral co-fragment.[47] $E_{INT,fragments}$ represents their combined internal energies. The final term, $E_{INT,parent}$, is the internal energy of the parent cation prior to photolysis, which is small due to rotational cooling in the supersonic expansion and the highly vertical ionization step. High-resolution threshold photoelectron spectroscopy measurements[28] show that the parent cations are formed predominantly (71%) in the zero-point level. Around 20% are formed with one quantum of excitation in the ν_7 (CH_3 deformation) mode with the remainder distributed in ν_6 and ν_9 (CH bend and CC stretch vibrational modes, respectively). Consequently, CH_3CHO^+ is formed relatively cold with an average internal energy of $\langle E_{INT,parent} \rangle = 350$ cm^{-1}. Angular distributions were fit to the usual expression:

$$I(\theta) \propto 1 + \beta_2 P_2(\cos\theta) + \beta_4 P_4(\cos\theta) + \cdots$$

where the β_n are anisotropy parameters and the P_n are Legendre polynomials. No terms beyond second order were significantly different from zero and the angular distributions can be characterized by a single anisotropy parameter, β (= β_2).

Channel I: $C_2H_3O^+ + H$

The lowest energy product channel is H-atom loss, with a dissociation energy D_0 of only 0.528 eV and a minimum AE for m/z = 43 ions of 0.67 eV if the ionic co-fragment is assumed to be acetylium (CH_3CO^+). Several higher energy $C_2H_3O^+$ isomers are also energetically accessible (see Figure 3-1). The lowest two energy isomers are 1-hydroxyvinylium (CH_2CHO^+) and oxiranylium ($O[CH_2CH]^+$) with energies of 1.296 eV and 2.431 eV relative to acetylium, respectively.[47] However, these isomers cannot be distinguished directly in these measurements. Despite the relatively large values of E_{AVL}, the unfavorable mass ratio between the $C_2H_3O^+$ ion and the H-atom co-fragment restricts the maximum allowed speeds (v_{max} ~590–710 m s^{-1}) and the ion images are small. The representative $C_2H_3O^+$ ion images shown in Figure 3-5 have been magnified by a factor of two relative to the others to show the ring structure more clearly. At longer wavelengths (λ > 252 nm), a single ring is observed, which increases in radius as the available energy increases. The most probable speeds, however, remain significantly less than v_{max}, indicating internal excitation of $C_2H_3O^+$ as $E_{INT,H}$ is necessarily zero. A second, smaller ring is evident at λ ≤ 252 nm (see the 236 nm ion image in Figure 3-5) and three rings can be distinguished at the shortest photolysis wavelength of 228 nm. The $C_2H_3O^+$ angular distributions are isotropic at all photolysis wavelengths, in contrast to the one-color REMPI study of Lee *et al.*, where anisotropy parameters up to β_6 were non-zero.[16]

The E_T distributions are decomposed by fitting to one, two, or three Gaussian functions. Each component can be characterized by the average translational energy, $\langle E_T \rangle$, and the standard deviation, σ_{E_T}. The latter parameter is characteristic of each component and insensitive to

photolysis wavelength. The fastest component is present at all λ, has an approximately constant $\langle E_T \rangle$ of ~1.1 eV between 316 nm and 284 nm, beyond which it increases linearly with E_{AVL}, reaching 2.24 eV. It also has the largest $P(E_T)$ spread, with σ_{E_T} = 0.83±0.08 eV. The distributions become clearly bimodal at λ ≤ 252 nm and the second, slower component has $\langle E_T \rangle$ values that increase linearly with E_{AVL} over the range 0.73–2.24 eV. It is also narrower, with σ_{E_T} = 0.52±0.03 eV. The third and slowest component, which is observed only at the shortest photolysis wavelength of 228 nm, has $\langle E_T \rangle$ = 0.65 eV and σ_{E_T} = 0.37 eV. In contrast to the other product channels discussed below, for which the undetected neutral fragment has internal degrees of freedom, the E_T distributions for the H-atom loss channel can be converted unambiguously into $C_2H_3O^+$ internal energy distributions using $E_{INT} = E_{AVL} - E_T$.

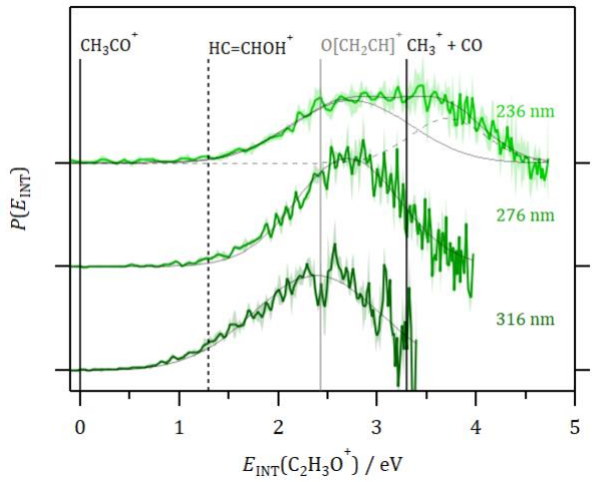

Figure 3-6 $C_2H_3O^+$ E_{INT} distributions at 316 nm, 276 nm, and 236 nm. Vertical lines are the energetic thresholds for formation of CH_3CO^+ isomers 1-hydroxyvinylium (dashed black) and vinoxyium (solid gray), along with secondary dissociation of $CH_3CO^+ \rightarrow CH_3^+ + CO$ (solid black). Total fits are shown (solid black) along with individual components of the 236 nm E_{INT} distribution (solid and dashed black). The dashed component corresponds to formation of the 1-hydroxyvinylium isomer.

The $C_2H_3O^+$ E_{INT} distributions obtained at 316 nm, 276 nm, and 236 nm are shown in Figure 3-6. The conversion from E_T to E_{INT} assumes production of the lowest energy $C_2H_3O^+$ isomer, acetylium, CH_3CO^+; the relative energies of other higher-energy $C_2H_3O^+$ isomers are also indicated. Values of E_{INT} > 3.30 eV are sufficient for CH_3CO^+ to undergo secondary dissociation to CH_3^+ + CO. As can be seen in Figure 3-6, the $P(E_{INT})$ distributions extend slightly beyond this value at 276 nm, while the secondary component in the 236 nm data lies entirely beyond this threshold.

Channel II: $HCO^+ + CH_3$

The major fragmentation channel producing formyl cations and neutral methyl radicals is the second lowest energy pathway, with D_0 = 1.510 eV and AE = 1.80 eV. E_{AVL} ranges from 2.41–3.93 eV. Representative ion images are shown in Figure 3-5. The maximum ion count density occurs near the image centers and declines to zero at speeds around half of v_{max} (2.34–2.99 km s^{-1}), indicating preferential partitioning of E_{AVL} into internal degrees of freedom of the HCO^+ and CH_3 fragments. The corresponding E_T distributions, shown in Figure 3-7(a), peak near zero with modest $\langle E_T \rangle$ values of 0.24–0.34 eV. The fraction of the available energy partitioned into translation, f_T, increases linearly with E_{AVL} from 0.06 to 0.14. The images are anisotropic at all wavelengths, with similar E_T-dependent anisotropy parameters, $\beta(E_T)$, that increase near-linearly from zero to +0.8 at the maximum observed E_T of ~1 eV, as shown in Figure 3-7(b). Lee *et al*. have obtained similarly anisotropic images, in one-color measurements at 363 nm that used REMPI to prepare the parent cation.[16]

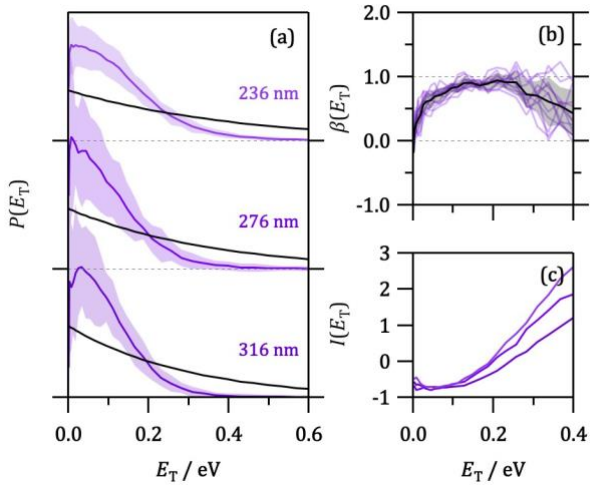

Figure 3-7 (a) HCO^+ total translational energy distributions at 316 nm, 276 nm, and 236 nm; (b) $\beta(E_T)$ are shown for all photolysis wavelengths (316 – 228 nm) along with their average (black); (c) linear surprisal plots showing two distinct gradients.

Channel III: CH_3^+ + HCO

The thermodynamic threshold for formation of CH_3^+ + HCO is 3.20 eV, limiting E_{AVL} to the range 0.72–2.24 eV. CH_3^+ ion images (representative examples are shown in Figure 3-5) are isotropic and dominated by large ion counts near the center. The radial distributions are curtailed at speeds significantly lower than v_{max} (2.47–4.35 km s^{-1}) and increase only slightly as the photolysis wavelength is decreased. The E_T distributions shown in Figure 3-8(a) peak at zero and drop off rapidly, appearing characteristic of statistical unimolecular dissociation on a surface without a barrier. As E_{AVL} increases, the distributions broaden slightly and the small values of $\langle E_T \rangle$ vary over the range 0.06–0.16 eV. The fraction of E_{AVL} partitioned into translation is independent of photolysis wavelength, with an average value of f_T = 0.068±0.008.

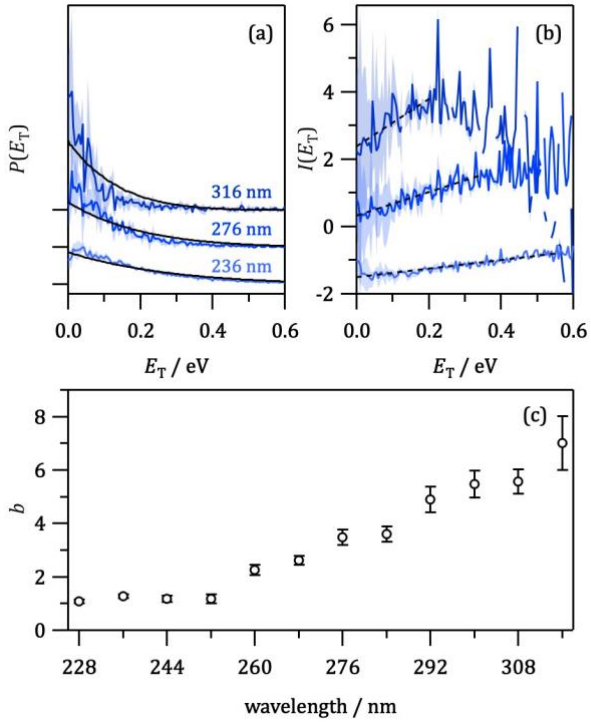

Figure 3-8 (a) CH_3^+ total translational energy distributions and phase space theory calculations (black) at selected photolysis wavelengths of 316 nm, 276 nm, and 236 nm; (b) linear surprisal plots; (c) variation of surprisal parameter, *b*, with available energy.

Channel IV: CH_4^+ + CO

The dissociation energy for channel IV is D_0 = 2.13 eV and E_{AVL} spans the range 1.80–3.31 eV. Ion images of CH_4^+ fragments have isotropic features at the image centers that are similar to those observed for CH_3^+ but are accompanied by a faster, anisotropic component that is distinct at photolysis wavelengths λ ≤ 300 nm, as shown in Figure 3-5. The most probable speeds of the fast component increase with excitation energy from 1.5 km s^{-1} to 3.0 km s^{-1}, but these speeds are still significantly smaller than the v_{max} determined by conservation of energy and momentum which span the range 3.7–5.0 km s^{-1}. The E_T distributions in Figure

3-9(a) clearly show the two components at shorter wavelengths. The slow components peak near zero at all wavelengths, and like CH_3^+, appear to indicate statistical barrierless dissociation. The slow and fast E_T components can be distinguished at $\lambda \leq 300$ nm by fits using Gumbel and Gaussian functions, respectively. $\langle E_T \rangle$ values for the anisotropic fast component increase from 0.40 eV at 300 nm to 1.20 eV at 228 nm; f_T also increases from 0.20 to 0.36. The spread in the fast component, which is characterized by the standard deviation of the Gaussian fit, increases from 0.18 eV at 300 nm before reaching a plateau at ~0.3 eV at $\lambda \leq 268$ nm. The fast component is anisotropic, with maximum intensity found at the poles, parallel to the laser polarization axis. At shorter wavelengths, where the two components are distinct, the anisotropy parameter for the fast component reaches a value of $\beta \approx +1$, indicating that CH_4^+ is formed promptly with recoil velocities that are preferentially parallel to the polarization of the UV photolysis laser. Smaller values of β at longer wavelengths are

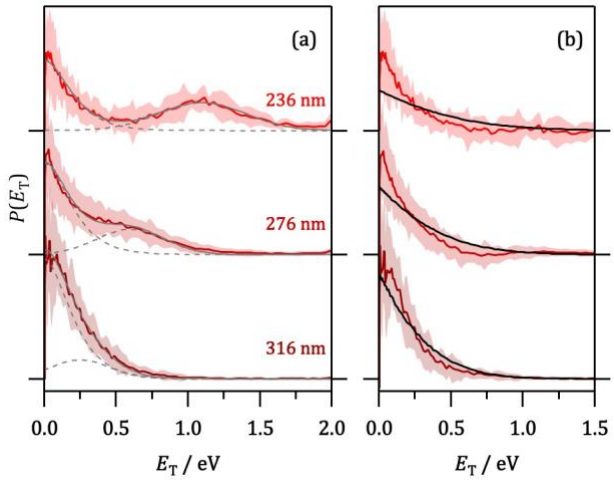

Figure 3-9 (a) CH_4^+ total translational energy distributions at selected photolysis wavelengths of 316 nm, 276 nm, and 236 nm along with total fits (solid gray) and individual fits (dashed gray); (b) Isolated slow component after subtraction of the fast component shown alongside PST calculations (solid black).

due to significant overlap with the isotropic slow component.

3.5 Discussion

Figure 3-4 shows the total photofragment ion yield spectrum, summed over all detected fragments, alongside the photoelectron spectrum measured by Cvitaš *et al*.[28] Ionization energy EOM-CC(2,3)/cc-pVTZ calculations reliably predict the energies of the bands observed in the photoelectron spectrum. The dominant feature in the PHOFY spectrum coincides approximately with the C̃ band in the photoelectron spectroscopy measurements at an excitation energy of approximately 4.9 eV (~250 nm in the PHOFY spectra shown in Figure 3-3) above the ground state of the CH_3CHO^+ cation. It is accompanied by a shoulder at 4.3 eV (~290 nm), and a tail that extends beyond the range of the measurements. Also shown in Figure 3-4 are the vertical excitation energies and corresponding oscillator strengths from EOM-CC/cc-pVTZ calculations. The first excited state $\tilde{A}^2A''$ has a vertical excitation energy of 3.08 eV and an oscillator strength of only 6.5×10^{-5}. The $\tilde{B}^2A'$ state at 4.24 eV has a slightly greater oscillator strength of 2.1×10^{-4} while that of the $\tilde{C}^2A'$ state at 5.03 eV is significantly larger at 1.6×10^{-2}. Consequently, the dominant feature in the PHOFY spectrum is assigned to a transition to the $\tilde{C}^2A'$ state while the weaker shoulder and signal observed to longer wavelengths are due to excitation to the $\tilde{B}^2A'$ and A^2A'' states. It seems likely that the excitation wavelength range used for the ion imaging measurements (316–228 nm) primarily accesses the $\tilde{C}^2A'$ state of CH_3CHO^+.

The differences in the photofragment yield and photoelectron spectra shown in Figure 3-4 can be readily justified. The photoelectron spectroscopy and PEPICO measurements used

thermal samples of acetaldehyde and involve single photon ionization, with subsequent fragmentation. Consequently, the observed fragment yields represent the product of the VUV photoionization cross-section with the fragmentation quantum yields. In contrast, VUV ionization near threshold first produces internally cold ions, which are subsequently fragmented by the UV pulse to yield the PHOFY spectra. That is, in the current measurements, the wavelength-dependent photofragment yields represent the equivalent fragmentation quantum yields, but now modified by the absorption cross sections for spectroscopic transitions of the ion.

The observation of CH_3^+ signal onset at $\lambda \approx 317$ nm (3.91 eV) implies an AE of 14.12 eV, a value that is in excellent agreement with previous PIMS and PEPICO measurements.[29,30,32] As has been commented on previously,[30,32] the CH_3^+ AE coincides closely with the adiabatic excitation energy required to access the B^2A' state, which is 0.71 eV higher than the thermodynamic threshold. However, the total translational energy distributions observed for CH_3^+ peak very close to zero and appear to be consistent with statistical and barrierless unimolecular dissociation on the $\tilde{X}^2A'$ surface following internal conversion. It seems likely that the increase in CH_3^+ yield at $\lambda < 317$ nm is due to the increase in the absorption cross section coincident with the energy threshold being reached, rather than dissociation occurring specifically on the $\tilde{B}^2A'$ surface or, as is more likely, the $\tilde{C}^2A'$ surface. As the CH_3^+ E_T distributions appear statistical, we model them using phase space theory (PST).[48,49] The PST calculations use theoretical spectroscopic constants calculated at the MP2/aug-cc-pVTZ level;[50] CH_3^+ is treated as an oblate symmetric top and HCO as a near-prolate symmetric top. The normalized E_T distributions calculated using PST are shown alongside the experimental

measurements in Figure 3-8 for a subset of the photolysis wavelengths used. In general, the experimental E_T distributions are close to statistical. The deviation from statistical behavior can be characterized using a linear surprisal analysis, in which the surprisal is evaluated as a function of the translational energy

$$I(E_T) = -\ln[P(E_T)/P°(E_T)] = a + bE_T$$

where $P(E_T)$ is the experimental distribution and $P°(E_T)$ is the statistical prior distribution, here obtained from the PST calculations. Figure 3-8 shows plots of the surprisal as a function of the translational energy. The plots are linear, with positive gradients ($b > 0$) indicating that the experimental distributions are somewhat colder than statistical. The gradients initially decrease monotonically as the available energy increases, meaning the experimental distributions become increasingly statistical, before reaching a constant value of ~1 at photolysis wavelengths less than 260 nm.

CH_3^+ E_T distributions that are colder than statistical are consistent with some fraction being formed by secondary dissociation of internally excited CH_3CO^+ formed by the H-atom loss pathway:

$$CH_3CHO^+ \rightarrow CH_3CO^+ + H \rightarrow CH_3^+ + CO + H \qquad \text{III}'$$

The triple fragmentation channel III′ can occur for CH_3CO^+ primary fragments with E_{INT} > 3.30 eV; that is, it is energetically accessible at all wavelengths used in the ion imaging experiments. Kable and co-workers have modelled triple fragmentation in the photochemistry of neutral acetaldehyde using sequential applications of PST to model the primary and secondary dissociation steps.[51] E_T distributions arising from triple

fragmentation pathways are universally colder than the statistical distributions obtained for a two-body fragmentation pathway leading to the same products. Johnson *et al*. measured $\langle E_T \rangle$ values for CH_3CO^+ fragments over a range of excess energies in PEPICO experiments and found a marked increase in the gradient above 3.6 eV (equivalent to a photolysis wavelengths of $\lambda < 344$ nm).[30] The observed increase in $\langle E_T \rangle$ was attributed to loss of the low-E_T (high-E_{INT}) component due to secondary dissociation. A similar increase in $\langle E_T \rangle$ values for $C_2H_3O^+$ is observed obtained in the current work (discussed in more detail below) at $E_{AVL} > 3.8$ eV, which is entirely consistent with the threshold for triple fragmentation via channel III′.

Triple fragmentation pathways are strongly entropically favored and tend to become increasingly dominant as the available energy is increased beyond the threshold.[51] However, the CH_3^+ surprisal analysis suggests the opposite trend. Namely, the experimental E_T distributions for channel III deviate most from the two-body fragmentation PST distributions at low excitation energies and become increasingly statistical as E_{AVL} increases. This observation suggests that the triple fragmentation channel III′ contributes most to the observed E_T distributions at the longest photolysis wavelengths, becoming less important at shorter wavelengths. The inflexion point in the plot of the surprisal parameter b against wavelength at $\lambda \leq 260$ nm ($E_{AVL} = 4.24$ eV) shown in Figure 3-8(c) coincides with the clear onset of bimodality in the $C_2H_3O^+$ E_{INT} distributions. While this may be coincidental, it will be argued below that the low-E_T components are due to H-atom loss from higher-energy CH_3CHO^+ isomers. As none of the other possible $C_2H_3O^+$ isomers can readily dissociate to form CH_3^+, we suggest that isomerization becomes increasingly competitive with

dissociation to form CH_3CO^+ + H and consequently the three-body fragmentation channel III′ is attenuated.

Barriers of 2.9–3.1 eV have been identified for keto-enol tautomerization $CH_3CHO^+ \rightarrow CH_2CHOH^+$ on the lowest cationic surface.[52,53] Tautomerization is therefore possible at all excitation wavelengths. As shown in Figure 3-6, the $C_2H_3O^+$ E_{INT} distribution is unimodal at photolysis wavelengths $\lambda > 260$ nm. The small E_T release is consistent with dissociation over a small barrier, most probably on the ground state following internal conversion, leading to CH_3CO^+ + H. Most of the available energy is partitioned into internal degrees of freedom of the cation fragment and even at the longest excitation wavelength, E_{AVL} is sufficient for secondary dissociation to CH_3^+ + CO (channel III′). As E_{AVL} increases, the E_{INT} distribution increasingly extends beyond the dissociation threshold for channel III′, becoming clearly bimodal at $\lambda \leq 260$ nm ($E_{AVL} \geq 4.24$ eV). $C_2H_3O^+$ fragments with $E_{INT} > 3.30$ eV are attributed to fragment isomers other than CH_3CO^+ that are formed by H-atom loss following parent isomerization. Figure 3-6 shows the energies of the two lowest-lying isomers of acetaldehyde cation, vinyl alcohol and oxirane cations. H-atom loss from these species is expected to form primarily 1-hydroxyvinylium and/or oxiranylium cations, with a high degree of internal excitation but insufficient energy to undergo secondary dissociation. We assign the features in the E_{INT} distributions energy order – the secondary component evident at $\lambda \leq 260$ nm is attributed to $C_2H_3O^+$ fragments resulting from H-atom loss from vinyl alcohol cation and the tertiary component that is observed at 228 nm is attributed to H-atom loss from oxirane cation. Isomerization appears to become increasingly competitive with CH_3CHO^+ dissociation as E_{AVL} increases, leading to a concomitant reduction in the amount of

secondary dissociation of CH_3CO^+ and hence the variation in the linear surprisal parameter with photolysis wavelength.

Another possible origin for the low-E_T components is formation of electronically excited CH_3CO^+. However, the lowest lying triplet and singlet states of CH_3CO^+ lie at 5.18 and 6.17 eV (239 and 201 nm) above the parent cation ground state, respectively.[54] We conclude that the appearance of the second feature at $\lambda \leq 260$ nm is not consistent with formation of electronically excited CH_3CO^+.

The fragmentation dynamics observed for channel IV are particularly intriguing. First, we note that CH_4^+ is observed at all excitation wavelengths. In contrast, Johnson *et al.*[30] were unable to observe CH_4^+ once the excitation energy was sufficient to excite on the $\tilde{B}$ band and they attributed CH_4^+ production specifically to photochemistry of the $\tilde{A}^2A''$ state. The presence of two distinct components in the E_T distributions at short wavelengths, seen in Figure 3-9(a), indicates formation of CH_4^+ *via* two pathways. The translationally fast component is anisotropic, with $\beta \approx +1$ at 236 nm while the slow component that peaks near zero is isotropic. Extrapolating from shorter wavelengths suggests that these two features are heavily overlapped at $\lambda > 292$ nm and the E_T-averaged anisotropy of $\langle\beta\rangle \approx +0.3$ at 316 nm is consistent with contributions from both components. The values for the anisotropy parameter are in reasonable agreement with observations made by Lee *et al.*[16] who reported $\beta = 0.5 \pm 0.1$ for CH_4^+ at 363 nm, where the fast and slow components are unresolved. The anisotropy of the fast component is clearly inconsistent with excitation to the $\tilde{A}^2A''$ state.

The isotropic slow component appears to be consistent with a largely statistical dissociation

on the ground state surface with little or no barrier.[55] The E_T distributions were modeled using PST as previously using both calculated and experimental spectroscopic data.[50,56] The normalized PST distributions are shown alongside experimental data in Figure 3-9(b). In general, the experimental E_T distributions appear close to statistical, but a linear surprisal analysis produces a wavelength independent surprisal parameter with an average value of $\langle b \rangle$ = 2.4±0.1. A positive surprisal parameter again indicates that the experimental E_T distributions are colder than statistical, as was the case for CH_3^+. While the colder-than-statistical E_T distributions for CH_3^+ were attributed to contributions from secondary dissociation of internally excited CH_3CO^+ formed in channel I, there are no simple (and barrierless) bond cleavage pathways that lead to the molecular cation CH_4^+. As in neutral acetaldehyde, a significant barrier might be expected for decomposition to form molecular products on the ground state, and consequently more substantial release of the available energy as translation. One possible explanation for low E_T fragments with high internal energy that has been suggested by Lee *et al.*[16] for CH_4^+ production is roaming. Highly internally excited CH_4 is produced by roaming mechanisms involving intramolecular reaction of nascent radical products CH_3 + HCO in the photodissociation of neutral acetaldehyde.[57] In the photochemistry of the acetaldehyde cation, however, either 'radical' may carry the charge and two intramolecular reactions could plausibly lead to formation of CH_4^+ + CO. One is long range proton transfer between CH_3 + HCO^+ and the second is H-atom abstraction reaction CH_3^+ + HCO. The current experiments cannot distinguish between these possibilities, and we acknowledge that a roaming mechanism is highly speculative. Improved characterization of the fragment internal energy distributions or, better,

correlated product state measurements and theoretical support are essential.

The effect of roaming dynamics in the photochemistry of ions is an interesting question that has been little explored to date. Roaming in ion-molecule reactions has been discussed recently by Mauguière *et al*.[58–60] from the perspective of a phase space interpretation of the dynamics. An example of roaming, albeit before the term roaming was coined, in an ionic system highlighted by Mauguière *et al*.[58] (and earlier by Klippenstein *et al*.[61]) is the decomposition of metastable protonated propylamine to form propyl radicals and ammonium cations studied by Audier and Morton.[62] It is quite possible that the presence of long-range attractive ion-dipole or ion-induced dipole interactions between the charged and neutral 'radical' products means roaming may be a general phenomenon in the fragmentation of ionic species.

The observation of anisotropic angular distributions for the translationally fast CH_4^+ fragments implies prompt dissociation, which is surprising for the molecular fragment. The positive anisotropy parameter is consistent with initial excitation being predominantly to the $\tilde{C}^2A'$ (or $\tilde{B}^2A'$) state. The modest translational energy release also indicates that the separating fragments experience some degree of repulsion during the dissociation, which most probably involves passage over a barrier. In neutral acetaldehyde, a high barrier on the S_0 surface can lead to the molecular products CH_4 + CO. A similar, albeit smaller, barrier on the cation $\tilde{X}^2A'$ (or D_0) surface would account for the translational energy release. However, the observed anisotropy requires that the transition state be reached in less than a rotational period. One possibility is that internal conversion occurs *via* a conical intersection between the $\tilde{B}^2A'$ or $\tilde{C}^2A'$ surfaces and the $\tilde{X}^2A'$ surface that is close to the

molecular transition state in configuration space. After internal conversion, the system is able to dissociate promptly. *Ab initio* calculations characterizing these regions of the cation potential energy surface are highly desirable. Formation of electronically excited CH_4^+ is possible, with the Ã state lying only 0.41 eV above the CH_4^+ ground state.[63] The electronic energy is a small fraction of E_{AVL} for channel IV, however, and would result into only a marginal decrease in f_T if the Ã state were formed. The current measurements are unable to distinguish between ground and excited state CH_4^+.

Finally, the experimental E_T distributions for the most abundant fragment HCO^+ shown in Figure 3-7(a) peak near zero and agree with the results of the PEPICO measurements of Johnson *et al.*,[30] and the ion imaging study by Lee *et al*.[16] While this appears to be broadly consistent with a statistical unimolecular dissociation mechanism, two pieces of experimental evidence suggest that this is not the complete story. First, the ion images shown in Figure 3-5 are clearly anisotropic, which is indicative of prompt, i.e. non-statistical, dissociation. Second, the anisotropy is highly E_T-dependent, increasing from zero to ~+1 as shown in Figure 3-7(b), which suggests that there may be two unresolved components in the E_T distributions. The presence of two components is supported by a linear surprisal analysis, shown in Figure 3-7(c). PST distributions calculated using both calculated and experimental spectroscopic constants taken from the literature[50,51] clearly do not reproduce the experimental data. The surprisal however clearly contains two linear components; the gradient is zero at low E_T and non-zero at higher E_T. We conclude that the observed E_T distributions for HCO^+ contain two unresolved components, one isotropic and statistical and the other anisotropic, with modest portioning of E_{AVL} into translation. The relative

contribution of each component is E_T-dependent and pulls the value of β to higher or lower values. The HCO^+ observations therefore appear to be very similar to those observed at longer photolysis wavelengths for CH_4^+, with the only major difference being that the 'fast' anisotropic component for the former remains heavily overlapped with the slow statistical components. The statistical component is likely formed by dissociation on the $\tilde{X}^2A'$ surface following internal conversion as suggested by previous studies.[29,30] The provenance of the anisotropic component is more difficult to discern. While the positive anisotropy is consistent with a prompt dissociation following excitation to the $\tilde{B}^2A'$ and the $\tilde{C}^2A'$ states, a remarkably small fraction of the available energy is partitioned into translation.

Direct fragmentation of polyatomic cations on electronically excited states is a relatively unusual occurrence. In mass spectrometric applications, ion fragmentation is often assumed to proceed statistically as described by the quasi-equilibrium theory (QET), in which dissociation depends only on total energy rather than the nature of the excitation.[25,26] Excited state dynamics in polyatomic cations was recently observed by Gichuhi *et al.*,[19] who used velocity map imaging to detect $HCNH^+$ fragments formed after excitation of ethylamine cations ($CH_3CH_2NH_2^+$) at 233 nm. Two components were also observed in the E_T distributions: a dominant slow component peaking at $E_T \approx 0$ and a minor fast component. The anisotropy parameter β also increased linearly with photofragment speed, as observed in our measurements of CH_4^+ and HCO^+.

3.6 Conclusion

Velocity-map ion imaging and photofragment yield spectroscopy have been used to study the photofragmentation dynamics of internally cold CH_3CHO^+ cations, produced in a molecular beam by single-photon VUV ionization at 118 nm. The total fragment ion yield reaches a maximum at ~250 nm, corresponding to excitation to the $\tilde{C}^2A'$ state. A weaker shoulder attributed to the $\tilde{B}^2A'$ state is observed at ~290 nm. At $\lambda > 317$ nm, fragmentation via channel II to form $HCO^+ + CH_3$ dominates; at $\lambda < 317$ nm channel III forming $CH_3^+ + HCO$ opens and the fractional yield of channel II decreases. Ion imaging measurements detecting $C_2H_3O^+$, HCO^+, CH_3^+ and CH_4^+ show fragment-specific and wavelength-dependent dissociation mechanisms. The photochemistry and fragmentation dynamics of polyatomic ions appears to be particularly rich, involving isomerization, statistical and dynamical dissociation, and multiple pathways to products. State-specific detection of fragments would provide useful additional experimental data to obtain further insights but are likely to be confounded by neutral dissociation products; complementary theoretical work to better characterize the ionic potential energy surfaces will be essential.

3.7 Acknowledgements

This material is based upon work supported by the National Science Foundation under Grant No. CHE-1566064. Acknowledgment is made to the Donors of the American Chemical Society Petroleum Research Fund for partial support of this research. L.M.M. would like to thank the Zuckerman STEM Leadership Program for support.

3.8 References

1 T. J. Millar, Astrochemistry, *Plasma Sources Sci. Technol.*, 2015, **24**, 043001.
2 S. Petrie and D. K. Bohme, Ions in space, *Mass Spectrom. Rev.*, 2007, **26**, 258–280.
3 R. C. Henry, The Local Interstellar Ultraviolet Radiation Field, *Astrophys. J.*, 2002, **570**, 697–707.
4 G. A. Blake, C. R. Masson, T. G. Phillips and E. C. Sutton, The rotational emission-line spectrum of Orion A between 247 and 263 GHz, *Astrophys. J. Suppl. Ser.*, 1986, **60**, 357.
5 S. Cazaux, A. G. G. M. Tielens, C. Ceccarelli, A. Castets, V. Wakelam, E. Caux, B. Parise and D. Teyssier, The Hot Core around the Low-Mass Protostar IRAS 16293-2422: Scoundrels Rule!, *Astrophys. J.*, 2003, **593**, L51–L55.
6 A. A. Jaber, C. Ceccarelli, C. Kahane and E. Caux, The Census of Complex Organic Molecules in the Solar-type Protostar IRAS16293-2422, *Astrophys. J.*, 2014, **791**, 29-.
7 M. A. Requena-Torres, J. Martín-Pintado, A. Rodríguez-Franco, S. Martín, N. J. Rodríguez-Fernández and P. de Vicente, Organic molecules in the Galactic center: Hot core chemistry without hot cores, *Astron. Astrophys.*, 2006, **455**, 971–985.
8 B. E. Turner, R. Terzieva and E. Herbst, The Physics and Chemistry of Small Translucent Molecular Clouds. XII. More Complex Species Explainable by Gas-Phase Processes, *Astrophys. J.*, 1999, **518**, 699–732.
9 J. Crovisier, D. Bockelée-Morvan, P. Colom, N. Biver, D. Despois and D. C. Lis, The composition of ices in comet C/1995 O1 (Hale-Bopp) from radio spectroscopy, *Astron. Astrophys.*, 2004, **418**, 1141–1157.
10 O. P. J. Vieuxmaire, M. G. D. Nix, J. A. J. Fitzpatrick, M. Beckert, R. N. Dixon and M. N. R. Ashfold, Predissociation of state selected Br_2^+ cations, *Phys. Chem. Chem. Phys.*, 2004, **6**, 543–554.
11 O. P. J. Vieuxmaire, N. H. Nahler, J. R. Jones, R. N. Dixon and M. N. R. Ashfold, Photodissociation of state selected $BrCl^+$ cations: branching ratios and angular anisotropies of the Br^+ product forming channels, *Mol. Phys.*, 2005, **103**, 2437–2452.
12 O. P. J. Vieuxmaire, N. H. Nahler, R. N. Dixon and M. N. R. Ashfold, Multiphoton dissociation dynamics of BrCl and the $BrCl^+$ cation, *Phys. Chem. Chem. Phys.*, 2007, **9**, 5531–5541.
13 S. H. Gardiner, T. N. V. Karsili, M. L. Lipciuc, E. Wilman, M. N. R. Ashfold and C. Vallance, Fragmentation dynamics of the ethyl bromide and ethyl iodide cations: a velocity-map imaging study, *Phys. Chem. Chem. Phys.*, 2014, **16**, 2167–2178.
14 A. D. Webb, N. H. Nahler and M. N. R. Ashfold, Imaging Studies of the Photodissociation of NH_3^+ and ND_3^+ Cations, *J. Phys. Chem. A*, 2009, **113**, 3773–3778.
15 A. G. Sage, T. A. A. Oliver, R. N. Dixon and M. N. R. Ashfold, Velocity map imaging studies of the photodissociation of H_2O^+ cations, *Mol. Phys.*, 2010, **108**, 945–955.
16 S. K. Lee, R. Silva, M. H. Kim, L. Shen and A. G. Suits, Photodissociation of Spatially Aligned Acetaldehyde Cations, *J. Phys. Chem. A*, 2007, **111**, 6741–6745.
17 M. H. Kim, L. Shen, H. Tao, T. J. Martinez and A. G. Suits, Conformationally Controlled Chemistry: Excited-State Dynamics Dictate Ground-State Reaction, *Science*, 2007, **315**, 1561–1565.

18 L. Shen, P. C. Singh, M. Kim, B. Zhang and A. G. Suits, Ion and Electron Imaging Study of Isobutanal Photoionization Dynamics, *J. Phys. Chem. A*, 2009, **113**, 68–74.
19 W. K. Gichuhi, A. M. Mebel and A. G. Suits, UV Photodissociation of Ethylamine Cation: A Combined Experimental and Theoretical Investigation, *J. Phys. Chem. A*, 2010, **114**, 13296–13302.
20 P. C. Singh, L. Shen, J. Zhou, H. B. Schlegel and A. G. Suits, Photodissociation Dynamics of Methylamine Cation and Its Relevance to Titan's Ionosphere, *Astrophys. J.*, 2010, **710**, 112.
21 M. H. Kim, B. D. Leskiw and A. G. Suits, Vibrationally Mediated Photodissociation of Ethylene Cation by Reflectron Multimass Velocity Map Imaging, *J. Phys. Chem. A*, 2005, **109**, 7839–7842.
22 M. H. Kim, B. D. Leskiw, L. Shen and A. G. Suits, Vibrationally Mediated Photodissociation of $C_2H_4S^+$, *J. Phys. Chem. A*, 2007, **111**, 7472–7480.
23 P. C. Singh, L. Shen, M. H. Kim and A. G. Suits, Photodissociation and photoelectron imaging of molecular ions: probing multisurface and multichannel dynamics, *Chem. Sci.*, 2010, **1**, 552–560.
24 W. M. Jackson and D. Xu, Photodissociation of the acetone cation at 355 nm using the velocity imaging technique, *J. Chem. Phys.*, 2000, **113**, 3651–3657.
25 J. . Lorquet, Landmarks in the theory of mass spectra, *Int. J. Mass Spectrom.*, 2000, **200**, 43–56.
26 C. Lifshitz, Intramolecular energy redistribution in polyatomic ions, *J. Phys. Chem.*, 1983, **87**, 2304–2313.
27 D. Chadwick and A. Katrib, Photoelectron spectra of acetaldehyde and acetyl halides, *J. Electron Spectrosc. Relat. Phenom.*, 1974, **3**, 39–52.
28 T. Cvitaš, H. Güsten and L. Klasinc, Deuterium shifts in the high resolution photoelectron spectra of acetaldehyde, *J. Chem. Phys.*, 1976, **64**, 2549–2551.
29 R. Bombach, J.-P. Stadelmann and J. Vogt, The fragmentation and isomerization of internal energy selected acetaldehyde molecular cations, *Chem. Phys.*, 1981, **60**, 293–299.
30 K. Johnson, I. Powis and C. J. Danby, A photoelectron—photoion coincidence study of acetaldehyde and ethylene oxide molecular ions, *Chem. Phys.*, 1982, **70**, 329–343.
31 A. J. Yencha, M. R. F. Siggel-King, G. C. King, A. E. R. Malins and M. Eypper, Threshold photoelectron spectroscopy of acetaldehyde and acrolein, *J. Electron Spectrosc. Relat. Phenom.*, 2013, **187**, 65–71.
32 H. W. Jochims, W. Lohr and H. Baumgärtel, Photoionization mass spectrometry studies of deuterated acetaldehydes CH_3CDO and CD_3CHO, *Chem. Phys. Lett.*, 1978, **54**, 594–596.
33 G. J. Fisanick, T. S. E. Iv, B. A. Heath and M. B. Robin, Multiphoton ionization mass spectroscopy of acetaldehyde, *J. Chem. Phys.*, 1980, **72**, 5571–5580.
34 T. S. Eichelberger IV and G. J. Fisanick, Multiphoton ionization spectroscopy of the 3s Rydberg state in the deuterated acetaldehydes, *J. Chem. Phys.*, 1981, **74**, 5962–5970.
35 S. K. Shin, B. Kim, J. G. Haldeman and S.-J. Han, State-Selected Photodissociation of Acetaldehyde Molecular Ion: Hydrogen Scrambling and the Product Branching Ratio, *J. Phys. Chem.*, 1996, **100**, 8280–8284.

36 B. W. Toulson, K. M. Kapnas, D. A. Fishman and C. Murray, Competing pathways in the near-UV photochemistry of acetaldehyde, *Phys. Chem. Chem. Phys.*, 2017, **19**, 14276–14288.
37 B. W. Toulson, D. A. Fishman and C. Murray, Photodissociation dynamics of acetone studied by time-resolved ion imaging and photofragment excitation spectroscopy, *Phys. Chem. Chem. Phys.*, 2018, **20**, 2457–2469.
38 A. H. Kung, J. F. Young and S. E. Harris, Generation of 1182-Å radiation in phase-matched mixtures of inert gases, *Appl. Phys. Lett.*, 1973, **22**, 301–302.
39 G. M. Roberts, J. L. Nixon, J. Lecointre, E. Wrede and J. R. R. Verlet, Toward real-time charged-particle image reconstruction using polar onion-peeling, *Rev. Sci. Instrum.*, 2009, **80**, 053104.
40 Y. Shao, Z. Gan, E. Epifanovsky, A. T. B. Gilbert, M. Wormit, J. Kussmann, A. W. Lange, A. Behn, J. Deng, X. Feng, D. Ghosh, M. Goldey, P. R. Horn, L. D. Jacobson, I. Kaliman, R. Z. Khaliullin, T. Kuś, A. Landau, J. Liu, E. I. Proynov, Y. M. Rhee, R. M. Richard, M. A. Rohrdanz, R. P. Steele, E. J. Sundstrom, H. L. W. III, P. M. Zimmerman, D. Zuev, B. Albrecht, E. Alguire, B. Austin, G. J. O. Beran, Y. A. Bernard, E. Berquist, K. Brandhorst, K. B. Bravaya, S. T. Brown, D. Casanova, C.-M. Chang, Y. Chen, S. H. Chien, K. D. Closser, D. L. Crittenden, M. Diedenhofen, R. A. D. Jr, H. Do, A. D. Dutoi, R. G. Edgar, S. Fatehi, L. Fusti-Molnar, A. Ghysels, A. Golubeva-Zadorozhnaya, J. Gomes, M. W. D. Hanson-Heine, P. H. P. Harbach, A. W. Hauser, E. G. Hohenstein, Z. C. Holden, T.-C. Jagau, H. Ji, B. Kaduk, K. Khistyaev, J. Kim, J. Kim, R. A. King, P. Klunzinger, D. Kosenkov, T. Kowalczyk, C. M. Krauter, K. U. Lao, A. D. Laurent, K. V. Lawler, S. V. Levchenko, C. Y. Lin, F. Liu, E. Livshits, R. C. Lochan, A. Luenser, P. Manohar, S. F. Manzer, S.-P. Mao, N. Mardirossian, A. V. Marenich, S. A. Maurer, N. J. Mayhall, E. Neuscamman, C. M. Oana, R. Olivares-Amaya, D. P. O'Neill, J. A. Parkhill, T. M. Perrine, R. Peverati, A. Prociuk, D. R. Rehn, E. Rosta, N. J. Russ, S. M. Sharada, S. Sharma, D. W. Small, A. Sodt, T. Stein, D. Stück, Y.-C. Su, A. J. W. Thom, T. Tsuchimochi, V. Vanovschi, L. Vogt, O. Vydrov, T. Wang, M. A. Watson, J. Wenzel, A. White, C. F. Williams, J. Yang, S. Yeganeh, S. R. Yost, Z.-Q. You, I. Y. Zhang, X. Zhang, Y. Zhao, B. R. Brooks, G. K. L. Chan, D. M. Chipman, C. J. Cramer, W. A. G. III, M. S. Gordon, W. J. Hehre, A. Klamt, H. F. S. III, M. W. Schmidt, C. D. Sherrill, D. G. Truhlar, A. Warshel, X. Xu, A. Aspuru-Guzik, R. Baer, A. T. Bell, N. A. Besley, J.-D. Chai, A. Dreuw, B. D. Dunietz, T. R. Furlani, S. R. Gwaltney, C.-P. Hsu, Y. Jung, J. Kong, D. S. Lambrecht, W. Liang, C. Ochsenfeld, V. A. Rassolov, L. V. Slipchenko, J. E. Subotnik, T. V. Voorhis, J. M. Herbert, A. I. Krylov, P. M. W. Gill and M. Head-Gordon, Advances in molecular quantum chemistry contained in the Q-Chem 4 program package, *Mol. Phys.*, 2015, **113**, 184–215.
41 S. Hirata, M. Nooijen and R. J. Bartlett, High-order determinantal equation-of-motion coupled-cluster calculations for ionized and electron-attached states, *Chem. Phys. Lett.*, 2000, **328**, 459–468.
42 J. F. Stanton and R. J. Bartlett, The equation of motion coupled-cluster method. A systematic biorthogonal approach to molecular excitation energies, transition probabilities, and excited state properties, *J. Chem. Phys.*, 1993, **98**, 7029.
43 T. H. Dunning Jr., Gaussian basis sets for use in correlated molecular calculations. I. The atoms boron through neon and hydrogen, *J. Chem. Phys.*, 1989, **90**, 1007–1023.

44 K. Raghavachari, G. W. Trucks, J. A. Pople and M. Head-Gordon, A fifth-order perturbation comparison of electron correlation theories, *Chem. Phys. Lett.*, 1989, **157**, 479–483.

45 R. J. Bartlett, J. D. Watts, S. A. Kucharski and J. Noga, Non-iterative fifth-order triple and quadruple excitation energy corrections in correlated methods, *Chem. Phys. Lett.*, 1990, **165**, 513–522.

46 K. L. K. Lee, M. S. Quinn, A. T. Maccarone, K. Nauta, P. L. Houston, S. A. Reid, M. J. T. Jordan and S. H. Kable, Two roaming pathways in the photolysis of CH_3CHO between 328 and 308 nm, *Chem. Sci.*, 2014, **5**, 4633–4638.

47 B. Ruscic, Active Thermochemical Tables (ATcT) values based on ver. 1.122 of the Thermochemical Network; available at ATcT.anl.gov.

48 P. Pechukas and J. C. Light, On Detailed Balancing and Statistical Theories of Chemical Kinetics, *J. Chem. Phys.*, 1965, **42**, 3281–3291.

49 P. Pechukas, J. C. Light and C. Rankin, Statistical Theory of Chemical Kinetics : Application to Neutral-Atom–Molecule Reactions, *J. Chem. Phys.*, 1966, **44**, 794–805.

50 R. Johnson, 2002.

51 G. de Wit, B. R. Heazlewood, M. S. Quinn, A. T. Maccarone, K. Nauta, S. A. Reid, M. J. T. Jordan and S. H. Kable, Product state and speed distributions in photochemical triple fragmentations, *Faraday Discuss.*, 2012, **157**, 227–241.

52 F. Tureček and V. Hanuš, Mass spectra of ethenol and its deutero analogues, *Org. Mass Spectrom.*, 1984, **19**, 423–427.

53 G. Bouchoux, Keto-enol tautomers and distonic ions: The chemistry of [CnH2nO] radical cations. Part I, *Mass Spectrom. Rev.*, 1988, **7**, 1–39.

54 D. R. Yarkony and H. F. Schaefer, The acetyl cation and its geometrical isomers, *J. Chem. Phys.*, 1975, **63**, 4317–4328.

55 D. A. Blank, S. W. North, D. Stranges, A. G. Suits and Y. T. Lee, Unraveling the dissociation of dimethyl sulfoxide following absorption at 193 nm, *J. Chem. Phys.*, 1997, **106**, 539–550.

56 K. Huber, *Molecular spectra and molecular structure: iv. constants of diatomic molecules.*, Springer-Verlag, New York, 2013.

57 P. L. Houston and S. H. Kable, Photodissociation of acetaldehyde as a second example of the roaming mechanism, *Proc. Natl. Acad. Sci.*, 2006, **103**, 16079–16082.

58 F. A. L. Mauguière, P. Collins, Z. C. Kramer, B. K. Carpenter, G. S. Ezra, S. C. Farantos and S. Wiggins, Roaming: A Phase Space Perspective, *Annu. Rev. Phys. Chem.*, 2017, **68**, 499–524.

59 F. A. L. Mauguière, P. Collins, G. S. Ezra, S. C. Farantos and S. Wiggins, Multiple transition states and roaming in ion–molecule reactions: A phase space perspective, *Chem. Phys. Lett.*, 2014, **592**, 282–287.

60 F. A. L. Mauguière, P. Collins, G. S. Ezra, S. C. Farantos and S. Wiggins, Roaming dynamics in ion-molecule reactions: Phase space reaction pathways and geometrical interpretation, *J. Chem. Phys.*, 2014, **140**, 134112.

61 S. J. Klippenstein, Y. Georgievskii and L. B. Harding, Statistical Theory for the Kinetics and Dynamics of Roaming Reactions, *J. Phys. Chem. A*, 2011, **115**, 14370–14381.

62 H. E. Audier and T. H. Morton, Rearrangements in metastable ion decompositions of protonated propylamines, *Org. Mass Spectrom.*, 1993, **28**, 1218–1224.
63 A. W. Potts and W. C. Price, The Photoelectron Spectra of Methane, Silane, Germane and Stannane, *Proc. R. Soc. Math. Phys. Eng. Sci.*, 1972, **326**, 165–179.

4 Mode-Specific Vibrational Predissociation Dynamics of $(HCl)_2$ via the First Overtones of the Donor and Acceptor Stretches

Kapnas, K. M. and Murray, C. *in preparation.*

4.1 Abstract

The vibrational predissociation dynamics of the HCl dimer have been investigated following initial excitation of the H–Cl stretch via the acceptor ($2\nu_1$) and donor ($2\nu_2$) overtone modes. Velocity map imaging (VMI) and resonance-enhanced multi photon ionization (REMPI) techniques were used to determine pair-correlated and overall rotational product state distributions. Following vibrational excitation of the $2\nu_1$ and $2\nu_2$ stretching modes, HCl(v =1, J) and HCl(v =0, J) fragments were detected by 2+1 REMPI using various transitions. Fragment speed distributions were extracted from ion images obtained probing specific HCl product rovibrational levels to yield correlated product pair distributions – all product pairs comprise one vibrationally excited HCl and one vibrational ground state HCl. The correlated product pair distributions show a strong propensity to minimize translational energy release and are used to determine a dissociation energy of D_0 = 397±7 cm^{-1} for the dimer. The overtone predissociation dynamics lead to highly non-statistical product pair distributions and show clear dependence on the mode excited. Predissociation lifetimes are distinctly different, with τ_{VP} = 13±1 ns measured for $2\nu_1$ and < 6 ns for $2\nu_2$ excitation.

4.2 Introduction

Hydrogen-bonded clusters have received a great deal of attention due to their unusual vibrational predissociation behavior.[1–3] Hydrogen halide dimers in particular have served as prototypical systems for examining intermolecular forces and hydrogen bonding. In these simple systems, energy transfer following mode-specific vibrational excitation is inefficient, leading to remarkably long lifetimes and highly non-statistical product state distributions.[4] Detailed studies of dimer spectroscopy and vibrational predissociation dynamics are key to obtaining a better understanding of hydrogen-bonded networks in condensed phases and biological systems.

The hydrogen chloride dimer, $(HCl)_2$, is a relatively well-studied system, with its equilibrium structure and rovibrational spectrum having been thoroughly characterized. Ohashi and Pine[5] recorded the first rotationally resolved near-infrared spectrum of $(HCl)_2$ using a long pathlength cooled cell under low pressure conditions; they later determined D_0 = 431±22 cm^{-1} from IR transition intensities.[6] The near-IR spectrum of $(HCl)_2$ suggested that the HCl monomer units undergo a rapid interconversion tunneling motion. Greater insight into the $(HCl)_2$ tunneling dynamics was provided by far-infrared studies reported by both Blake *et al.*[7,8] and Mozzen-Ahmadi *et al.*[9,10] as well as coherent anti-Stokes Raman spectroscopy (CARS) studies by Furlan *et al.*,[11] with results estimating a large ground state tunneling splitting of ~14.9 cm^{-1} and a substantially smaller fundamental HCl stretch tunneling splitting of ~3.4 cm^{-1}. Schuder *et al.*[12–14] later refined rotational constants and interconversion tunneling frequencies for the "free" HCl stretch (ν_1) and "bound" HCl stretch (ν_2) of both HCl and DCl dimers using a jet-cooled sample and a diode laser based high-

resolution near-IR spectrometer. Combination bands of the van der Waals stretch (ν_4), geared bend (ν_5), and torsional (ν_6) modes have been reported and characterized by Fárník *et al.*[15,16] in the HCl stretch fundamental region using high-resolution near-IR spectroscopy. These experimental measurements have further been accompanied by extensive ab initio calculations of the $(HCl)_2$ potential energy surface.[17–24]

A handful of experimental studies have explored vibrational predissociation dynamics of the HCl dimer in the fundamental stretching region. Valentini and co-workers[25,26] used stimulated Raman excitation to excite the ν_1 and ν_2 modes and probed the resulting HCl monomer fragments using resonance-enhanced multiphoton ionization (REMPI). By displacing the pump and probe beams,[27] they were able to measure photofragment recoil velocities. A refined value of the dissociation energy of D_0 = 439±1 cm^{-1} was determined. Predissociation lifetimes were found to be in the range 16–46 ns, with the slower rates corresponding to excitation of the free HCl stretch, ν_1. The correlated HCl(v' = 0, J') + HCl(v'' = 0, J'') fragment rotational distributions showed a strong tendency to maximize the rotational excitation of the products. Similar results were observed by Vissers *et al.*[28] using a photofragment translational spectroscopy technique. Vibrational predissociation of the more strongly bound $(HF)_2$ dimer (D_0 = 1062±1 cm^{-1})[29] shows a stronger propensity for formation of high-J–low-J product pairs and has a shorter lifetime compared to $(HCl)_2$. In contrast, the product rotational distributions and longer lifetimes observed in $(HCl)_2$ vibrational predissociation indicate a far less rigid (or "floppier") structure, consistent with its larger tunneling splittings.[12,30] Vissers *et al.*[28] also performed six-dimensional quantum

calculations of predissociation lifetimes and product state distributions using the ES1–EL potential energy surface[17,18] that gave results that agreed qualitatively with experiments.

Despite the many spectroscopic studies of the fundamental region, the first overtone region has been neglected. Wittig *et al.* used IR cavity ring-down spectroscopy (CRDS) to record spectra of the $2\nu_1$ band of $(HCl)_2$.[31] Substantial quenching of the interconversion tunneling means that the heterodimers are distinguishable at the eigenstate level in the overtone spectrum. This phenomenon has also been observed for both first and second overtone excitation of $(HF)_2$ showing that vibrational excitation effectively suppresses tunneling.[30,32–34] Vibrational predissociation of $(HCl)_2$ following excitation in the overtone region has only been the (indirect) subject of a single study.[35] Liu *et al.* used high-*n* Rydberg H-atom time-of-flight spectroscopy to measure the total kinetic energy release resulting from vibrationally-mediated photodissociation of $(HCl)_2$ at 193 nm. The fastest moving H atoms observed at long IR-UV delays were attributed to photolysis of highly internally excited HCl(v = 0, J =20, 21) produced by vibrational predissociation. Such an efficient conversion of two quanta of vibrational excitation into monomer rotation was surprising but these interesting observations have yet to be explored further. Picconatto *et al*.[36] subsequently investigated the 193 nm photodissociation of "untagged" $(HCl)_2$. Without the IR excitation, HCl products were formed almost exclusively in v = 0 with very little rotational excitation - the most populated level was $J \approx 2$.[36]

Here, we present the results of infrared action spectroscopy and velocity-map ion imaging experiments characterizing the vibrational predissociation dynamics of $(HCl)_2$ in the HCl stretch overtone region at $\sim$5650 cm^{-1}. Low resolution infrared action spectroscopy using

2+1 REMPI to detect HCl predissociation products has been used to identify the $2\nu_1$ and $2\nu_2$ overtones and the $2\nu_2+\nu_4$ combination band of $(HCl)_2$. Ion images have been recorded for a range of HCl(v = 1, J) predissociation products following excitation on the $2\nu_1$ and $2\nu_2$ bands, yielding correlated product pair state distributions.

4.3 Experimental methods

Experiments were performed in a velocity-map imaging (VMI) mass spectrometer that has been described in detail previously.[37] Briefly, HCl dimers were prepared by supersonic expansion of 5% HCl in argon (Airgas) from a stagnation pressure of 2 atm using a pulsed valve (General Valve, Series 9) and skimmed (Beam Dynamics). The resulting molecular beam was intersected perpendicularly by counter-propagating IR pump and UV probe beams that served to vibrationally excite the dimers and detect predissociation products via 2+1 resonance-enhanced multiphoton ionization (REMPI). IR radiation was generated using an optical parametric oscillator system (Continuum Mirage 3000) pumped by a seeded Nd:YAG laser (Continuum Powerlite Precision 8000). While this laser can produce single-mode output, only the non-resonant oscillator (NRO) and optical parametric amplifier (OPA) stages were pumped in the current experiments, providing a spectral linewidth of 4 cm^{-1} (FWHM). Average pulse energies in the range 1.80–1.76 μm (5560–5680 cm^{-1}) were 10–13 mJ. The UV probe was generated by frequency doubling in a BBO crystal the visible output of an Nd:YAG-pumped dye laser (Continuum Surelite II–10, Quanta-Ray PDL-3) operating with Coumarin 480 or 500 dyes (Exciton). Various IR-enhanced HCl REMPI transitions were observed in the vicinity of the E–X(0,0) and V–X(10,0) bands between 239.7–240.8 nm and in the F–X(0,1) band between 250.0–251.1 nm. The probe laser produced UV pulses with a

linewidth of ~3 cm^{-1} and typical pulse energies of ~1 mJ. Both pump and probe laser beams were focused at the center of the ionization region of the mass spectrometer using f = 250 mm lenses and were held at a fixed time delay of 40 ns. Product ions were accelerated by a stack of velocity-mapping electrodes towards a position-sensitive 40 mm diameter microchannel plate/phosphor screen assembly (Photonis) and CCD camera (Basler). The resulting images were analyzed using the polar onion-peeling method.[38] IR action spectra of $(HCl)_2$ were recorded with the UV probe laser fixed on a background-free HCl REMPI transition and monitoring the magnitude of the m/z = 35 and 36 peaks ($^{35}Cl^+$ and $H^{35}Cl^+$) in the mass spectrum while scanning the IR pump wavelength. The IR wavelength was calibrated by monitoring depletion of selected $F^1\Delta_2$–$X^1\Sigma^+$(0,0) REMPI signals while scanning over the P(1), R(0) and R(1) rovibrational transitions of the first overtone band at 5647 cm^{-1}, 5688 cm^{-1}, and 5706 cm^{-1}, covering the null gap wherein the dimer bands lie.

4.4 Results and Analysis

Initial measurements to calibrate the IR OPO were performed by observing depletion of HCl 2+1 REMPI signals as the IR wavelength was scanned to identify rovibrational transitions (refer to experimental section) and then tuned to the acceptor HCl stretching frequency ($2\nu_1$) of the dimer at 5656 cm^{-1}, reported by Liu *et al.*[31] The broad bandwidth of the OPO facilitated tuning the IR wavelength to the resonance. With the IR laser fixed at this frequency, the UV probe laser was scanned over a section of the Q branch of the $E^1\Sigma^+$–$X^1\Sigma^+$(0,0) band. The appearance of several additional lines only when the IR pump laser precedes the UV probe laser confirms predissociation – the REMPI spectra will be discussed below. Spectroscopic assignment of the background-free REMPI transitions observed in IR+UV experiments is

complicated by uncertainties in the spectroscopic constants derived from jet-cooled low-J spectra used to accurately predict the frequencies of transitions from high-J levels. Further complication arises from the relatively poor wavelength reproducibility of the dye laser. Conclusive assignments are made possible, however, by analysis of the ion images, which characterize the speed/translational energy and definitively identify the co-fragments. Since all product pairs identified comprise one HCl(v = 0) and one HCl(v = 1), they are labelled as HCl(J_0, J_1), where the subscripts indicate the vibrational quantum number. The IR action spectroscopy, HCl product REMPI spectroscopy, and velocity-map ion images will be described below.

4.4.1 Infrared Action Spectroscopy

The IR action spectrum in the HCl stretch overtone region is shown in Figure 4-1. The spectrum was recorded by monitoring total m/z = 36 ($H^{35}Cl^+$) REMPI signal at a two-photon wavenumber of 83583 cm^{-1} while repeatedly scanning the IR laser over the range 5580–5700 cm^{-1}. The HCl product transition, which is labeled as peak C in Figure 4-2, was initially selected for being one of the strongest background-free lines in the IR+UV REMPI spectrum. With knowledge of the photofragment speeds obtained from ion imaging experiments discussed below, it could be conclusively established that this transition originates in the J_1 = 12 level. Although they will not be discussed further here, the relative magnitudes of the various bands in the spectrum depend on the HCl product quantum state probed, suggesting strongly mode-specific predissociation dynamics.

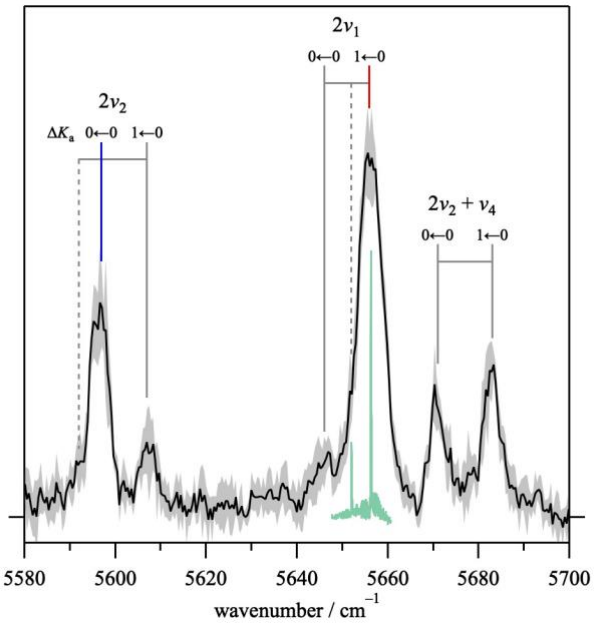

Figure 4-1 IR action spectrum of $(HCl)_2$ obtained probing $H^{35}Cl(J_1 = 12)$ predissociation products. Solid and dashed ladders indicate bands due to the $(H^{35}Cl)_2$ homodimer and the $H^{35}Cl–H^{37}Cl$ heterodimer, respectively. The blue line at 5597 cm^{-1} indicates the $2\nu_2$ transition used for imaging, the red line at 5656 cm^{-1} indicates the $2\nu_1$ transition. Also shown in green is the high-resolution cavity ring-down spectrum recorded by Liu *et al.*[31]

The strongest vibrational band in Figure 4-1 is observed at 5656 cm^{-1} and is assigned to the $2\nu_1$ $K_a = 1\leftarrow0$ sub-band of the $(H^{35}Cl)_2$ homodimer based on the CRDS spectrum of Liu *et al.*[31] The ~4 cm^{-1} bandwidth of the IR laser used in these measurements is significantly lower, preventing resolution of the underlying branch structure of the sub-bands. However, the equivalent $2\nu_1$ $K_a = 1\leftarrow0$ sub-band of the $H^{35}Cl–H^{37}Cl$ heterodimer can be discerned as an unresolved shoulder at longer wavelengths. Another weaker band is observed red shifted by ~10 cm^{-1} relative to the 5656 cm^{-1} band and is consistent with the energy spacings between the $K_a = 1\leftarrow0$ and $0\leftarrow0$ sub-bands reported for the $(HCl)_2$ fundamental.[12] A similar pair of bands are seen at 5597 cm^{-1} and 5607 cm^{-1}, albeit weaker. These bands are assigned

to the donor HCl stretching ($2\nu_2$) mode of the homodimer, with the peak spacing consistent with assignment to the K_a = 1←0 and 0←0 sub-bands. A weak shoulder to the red of the K_a = 0←0 sub-band at 5592 cm^{-1} is attributed to the heterodimer.

Scanning the IR laser further to the blue of the $2\nu_1$ transition resulted in the observation of two new features at 5671 and 5683 cm^{-1}. The shift of ~75 cm^{-1} from the $2\nu_2$ band is consistent with the frequency for ν_4 determined from high-resolution IR absorption spectroscopy of the $\nu_2+\nu_4$ combination band in the fundamental region by Fárník *et al*.[16] We have tentatively assigned these features to the K_a = 0←0 and 1←0 sub-bands of the $2\nu_2+\nu_4$ combination band based on the frequency shift. This assignment requires that the $2\nu_2+\nu_4$ combination band originate in the lower tunneling level; in contrast, the detailed spectroscopic analysis of Fárník *et al*. showed that the $\nu_2+\nu_4$ combination bands originated exclusively in the upper tunneling level.[16]

4.4.2 REMPI spectroscopy of HCl fragments

2+1 REMPI spectra of HCl were recorded over a section of the Q branch of the $E^1\Sigma^+$–$X^1\Sigma^+$(0,0) and the Q and P branches of the $F^1\Delta_2$–$X^1\Sigma^+$(0,1) bands (238.8–239.7 nm and 251.0–250.0 nm, respectively). The UV-only spectrum shown in the bottom panel of Figure 4-2 shows background HCl(J_0) lines that are readily assignable to the Q and O branch lines of the E–X(0,0) band and the S(0) transition of the V–X(0,0) band, based on PGOPHER[39] simulations using rotational constants reported by Green *et. al.*[40] Transitions originating in J = 0–2 are far more intense and indicate a molecular beam temperature of ~15 K. The small residual population in higher rotational levels J = 3–7 can be characterized by an approximate

rotational temperature of ~200 K. The F–X(0,1) region is free of any detectable signal from residual HCl monomer.

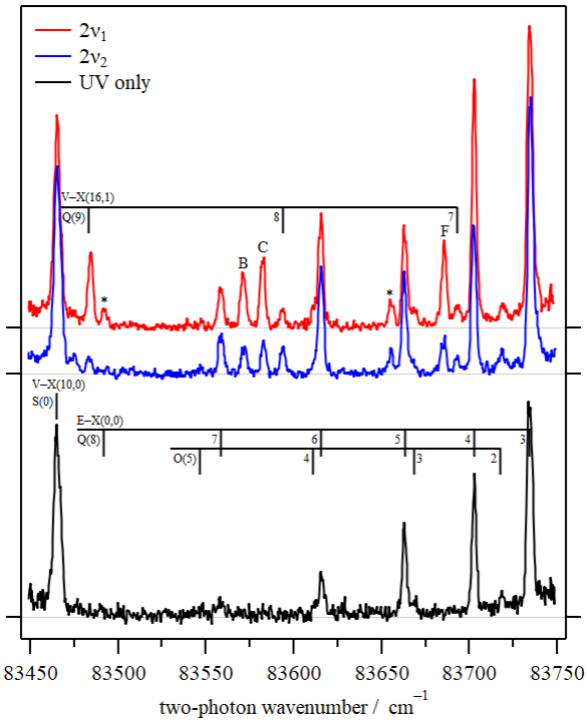

Figure 4-2 2+1 REMPI spectra of a section of the HCl $E^1\Sigma^+$–$X^1\Sigma^+$(0,0) Q-branch recorded on the m/z = 36 ($H^{35}Cl^+$) channel. The UV only spectrum (black) shows signal due to residual HCl monomer present in the molecular beam. The upper spectra were recorded with the IR pump tuned to either the $2\nu_1$ band at 5656 cm^{-1} (red) or the $2\nu_2$ band at 5597 cm^{-1} (blue). The IR+UV spectra contain additional spectral lines and show enhancement in some E–X(0,0) transitions. Assignments are made based on known HCl spectroscopy and analysis of speed distributions obtained from ion images. The transitions marked with asterisks have not been identified

IR+UV spectra of the E–X(0,0) Q branch region are shown in Figure 4-2, following excitation of the $2\nu_1$ K_a = 1←0 sub-band at 5656 cm^{-1} and the $2\nu_2$, K_a = 0←0 sub-band at 5697 cm^{-1} of the $(H^{35}Cl)_2$ homodimer. For convenience, these bands will be referred to simply as $2\nu_1$ and $2\nu_2$ hereafter, and we neglect any effects of pumping the dimer to different K_a levels. The

IR+UV REMPI spectra show clear enhancement in the E–X(0,0) Q(2)–Q(8) transitions. The degree of signal enhancement is clearly dependent on the vibrational mode excited. For example, the signal enhancements of the Q(3) and Q(7) lines are similar, while the Q(4) line shows marked enhancement after $2\nu_1$ excitation, but little change after $2\nu_2$ excitation. The Q(5) line is effectively unchanged. Seven additional lines are also observed in the IR+UV REMPI spectrum in this region. Three can be readily assigned to the Q(7), Q(8), and Q(9) transitions of the $V^1\Sigma^+$–$X^1\Sigma^+$(16,1) band based on simulations using published spectroscopic constants[40,41] and confirmed by the ion imaging results (see below). However, difficulty arose when attempting to assign peaks labeled B, C, and F in Figure 4-2 using simulations of previously characterized HCl REMPI spectra. Like all REMPI transitions in this region, fragmentation to form Cl^+ suggests that the lines labeled B, C, and F likely result from excitation to $^1\Sigma^+$ states.[40] Assignments for the quantum states in which these transitions originate can be found through analysis of the speed distributions derived from ion images, however. The assignments will be fully justified below, but here it will simply be asserted that peak B results from HCl(J_0 = 11); peak C probes HCl(J_1 = 12); and peak F arises from HCl(J_0 = 13) products.

Figure 4-3 shows 2+1 REMPI spectra of the $F^1\Delta_2$–$X^1\Sigma^+$(0,1) band obtained with the IR tuned to the $2\nu_1$ and $2\nu_2$ bands. The ion yields were much lower in this region and the spectra are noisier than those shown in Figure 4-2, despite more signal averaging. A strong, unresolved Q branch with a band head at J_1 = 14 is evident in the IR-induced spectra at 79960–79985 cm^{-1}. The cluster of peaks in the range 79700–79800 cm^{-1} are high-J transitions of the P branch. Small m/z = 35 (Cl^+) signals underlie the P(13), P(11) and low-J Q branch transitions

are attributed to overlapping transitions to an unidentified $^1\Sigma^+$ state.[40] In contrast, ionization via the $F^1\Delta_2$ state does not result in ion fragmentation. The relative intensities of the P branch lines are different following initial excitation of the $2\nu_1$ or $2\nu_2$ bands.

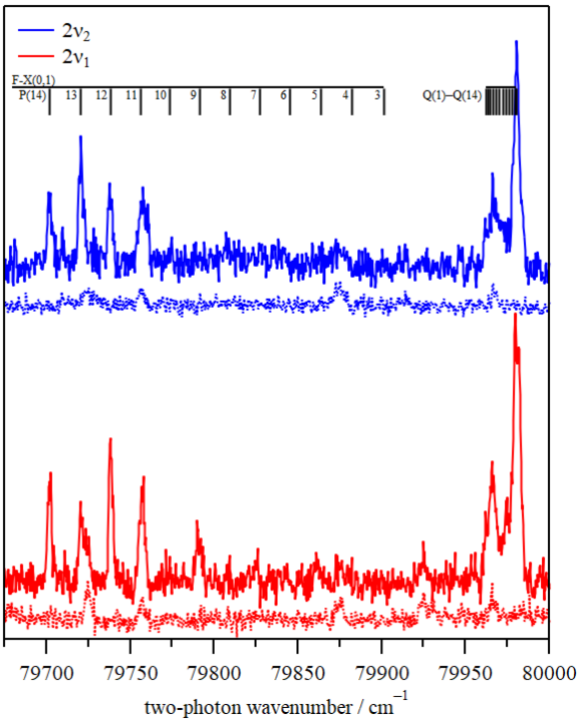

Figure 4-3 2+1 REMPI spectra of the HCl $F^1\Delta_2$–$X^1\Sigma^+$(0,1) band. No UV only signal was observed in this region. The spectra were recorded with the IR pump tuned to either the $2\nu_1$ band at 5656 cm^{-1} (red) or the $2\nu_2$ band at 5597 cm^{-1} (blue). Solid and dashed lines indicate signals recorded on m/z = 36 ($H^{35}Cl^+$) and m/z = 35 ($^{35}Cl^+$) channels. Fragmentation is indicative of excitation to a neighboring $^1\Sigma^+$ state. Assignments are made based on known HCl spectroscopy and analysis of speed distributions obtained from ion images.

4.4.3 Ion Imaging

Representative ion images obtained by monitoring HCl in the J_1 = 11–14 levels following initial excitation of the $2\nu_1$ and $2\nu_2$ modes of the HCl dimer are displayed in the upper portion

of Figure 4-4. The ion images display distinct isotropic rings and are characteristic of both the product quantum state probed and the IR excitation energy. Radial distributions are extracted from the ion images using the polar onion peeling approach and converted to velocity space using a pixel-to-speed conversion factor of 6.089 m s^{-1} $pixel^{-1}$. The conversion factor was determined using calibration images of S(^{1}D) obtained following photolysis of OCS at 235 nm and Cl($^2P_{3/2}$) obtained from Cl_2 photolysis at 355 nm; both calibration approaches yielded consistent results. The fragment recoil speed distributions are also

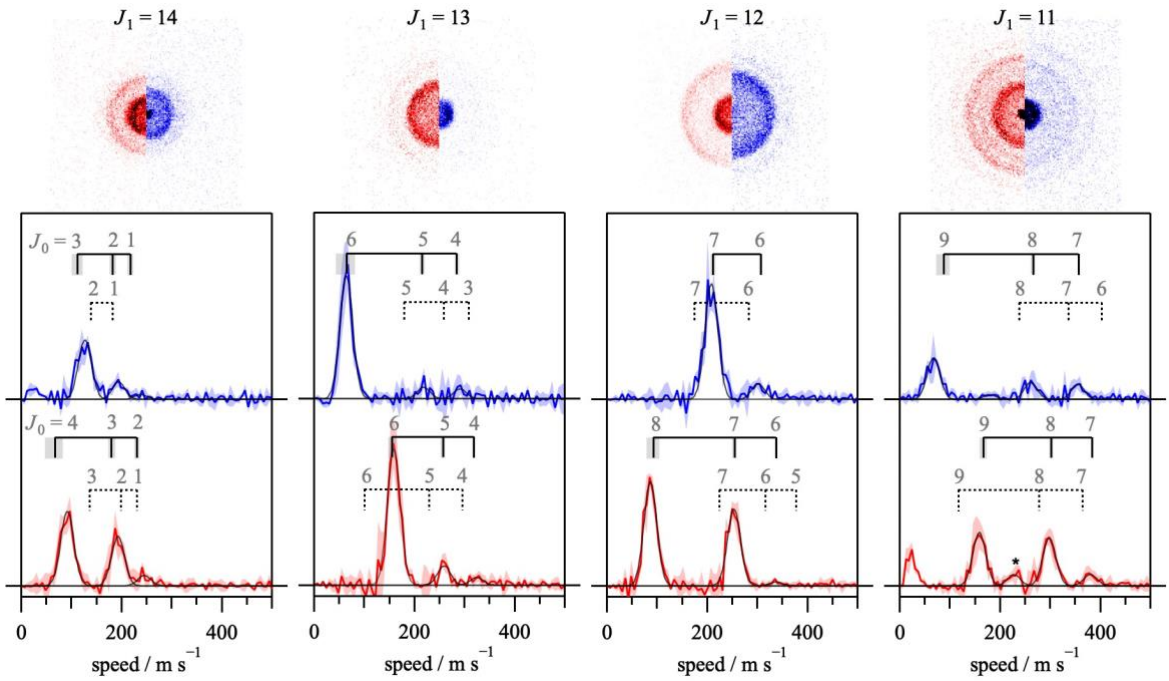

Figure 4-4 Ion images and normalized speed distributions obtained probing HCl(v = 1, J) predissociation products on the F–X(0,1) transition following predissociation of $(HCl)_2$ via the $2\nu_1$ (red) and $2\nu_2$ (blue) modes. Fits to Gaussian functions are shown in black. Vertical ladders mark the maximum speed calculated for formation of the partner fragment in the specified v = 0, J levels. Solid and dashed ladders represent speeds calculated using our experimental value of D_0 = 397±7 cm^{-1} and the previously reported value of D_0 = 439 cm^{-1}, respectively. Shaded regions represent 1σ standard deviations for speed distributions and calculated rotational states. Features marked with asterisks originate from overlapping REMPI transitions.

shown in Figure 4-4, below the respective ion images. Recoil speeds are modest with most discernable features, corresponding to formation of different quantum states of the undetected HCl(J_0), having speeds less than ~400 m s^{-1}. For the J_1 = 11–14 product levels, the co-fragment population distribution tends to be limited to fewer levels following $2\nu_2$ excitation than for $2\nu_1$ excitation.

The recoil speed distributions directly determine the correlated product pair distributions. Using energy conservation

$$h\nu_{IR} - D_0 = E_{V,R}(J_0, J_1) + E_T \quad (1)$$

where $h\nu_{IR}$ is the vibrational excitation energy, D_0 is the dimer dissociation energy, $E_{V,R}(J_0, J_1)$ is the rovibrational energy of the HCl(J_0, J_1) product pair, and E_T is the total translational energy. The rovibrational term values for HCl are known to sub-wavenumber precision[41,42] and state-selective REMPI detection precisely defines the contribution to $E_{V,R}(J_0, J_1)$ of the level probed. Consequently, the spacings between features in the speed distributions are related to the energy level spacings in the undetected HCl co-product. The upper limit uncertainty is the IR laser bandwidth (~4 cm^{-1}).

Dissociation energy of $(HCl)_2$. Previous measurements have determined D_0 values of 431±22 cm^{-1} and 439±1 cm^{-1} for $(HCl)_2$.[6,26] However, recoil speeds for different product pair combinations calculated using the more precisely determined of these D_0 values were incompatible with the observed speed distributions. The discrepancies between the observed and calculated recoil speeds shown in Figure 4-4 imply a significant error in the available energy following predissociation. While one potential cause of the discrepancy is

error in the pixel-to-speed calibration factor, we find that unreasonably large changes (>20%) would be necessary to achieve agreement. Any revised calibration factor would be inconsistent with both independent calibration measurements and the results of our previous ion imaging measurements. Another source of error is the IR photon energy. However, this was calibrated by REMPI depletion measurements that involved scanning the IR frequency over very well characterized HCl monomer rovibrational overtone transitions. The only remaining source of error arises from the previously reported values of D_0.

A non-linear least-squares fit was used to optimize the value D_0 by minimizing the root mean square differences between the calculated speed for each product pair in the distribution and the average speed of each feature. The speed distributions were fit to sums of Gaussian functions each with fixed FWHM of 30 m s^{-1} (~5 pixels), characteristic of the experimental resolution, and the amplitudes and average speeds (peak centers) allowed to float. The D_0 fit was repeated for a total of fourteen different speed distributions for which spectroscopic assignments of the probed level could be made with confidence. Specifically, transitions probing J_1 = 7–9 and J_1 = 11–14 following vibrational excitation of both $2\nu_1$ and $2\nu_2$ bands. The fits returned consistent values of D_0 with an average value of 397±7 cm^{-1} (1σ uncertainty). As can be seen in Figure 4-4, the new smaller value of D_0 reproduces all the features in the observed speed distributions. The discrepancy between the D_0 value obtained in this work and those determined previously will be discussed below.

Assignments of unidentified REMPI features. Using the new value of D_0, the identities of the levels probed by the unidentified REMPI lines labeled B, C, and F in Figure 4-2 can be determined. The observed features in the speed distributions are readily matched to

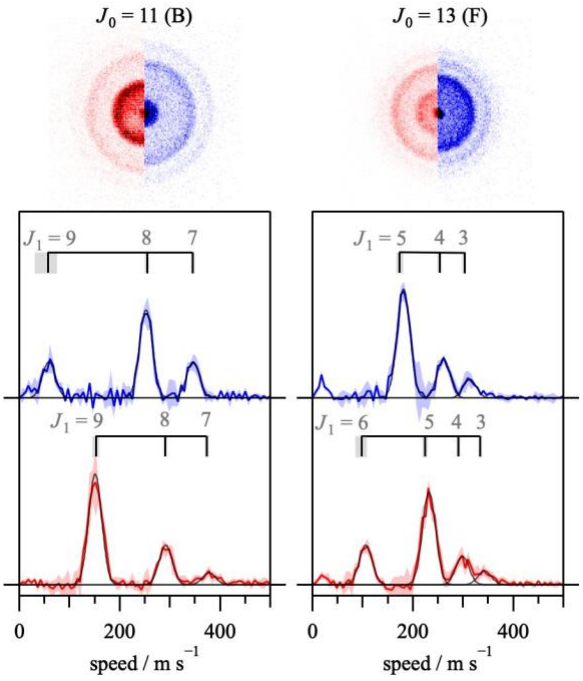

Figure 4-5 Ion images and normalized speed distributions of HCl product peaks B and F (shown in Figure 4-2) resulting from the predissociation of $(HCl)_2$ via the $2\nu_1$ (red) and $2\nu_2$ (blue) modes. Peaks B and F have been assigned to HCl(v =0, J =11) and HCl(v =0, J =13), respectively. See text for discussion. Horizontal ladders mark the maximum speed calculated using D_0 = 397±7 cm^{-1} for formation of the partner fragment in specified ν = 1, J levels. Shaded regions represent 1σ standard deviations for speed distributions and calculated rotational states.

energetically allowed co-fragment HCl(J_v) levels. Ion images obtained probing on lines B and F are shown in Figure 4-5 along with their respective speed distributions and co-fragment assignments. Line B can be conclusively assigned to a REMPI transition that originates in J_0 = 11 that is formed in conjunction with J_1 = 7–9. Similarly, feature F is definitively assigned to a transition probing J_0 = 13, with the speed distributions indicating co-fragments formed in J_1 = 3–6. Satisfactory reproduction of the speed distribution obtained probing peak C, which was used to measure the IR action spectrum shown in Figure 4-1, was obtained by assuming either J_0 = 20 or J_1 = 12 products. The rovibrational terms for these levels are 4489

cm^{-1} and 4480 cm^{-1}, respectively, and both assignments are consistent, within the precision of the imaging measurements, with HCl(J_0 = 6–8) co-products,. However, the speed distribution obtained from the line C ion image is the same as that obtained probing on the $F^1\Delta_2$–$X^1\Sigma^+$(0,1) P(12) transition shown in Figure 4-4 with regard to both peak heights and positions. Consequently, we favor the J_1 =12 assignment.

Correlated product pair and overall state distributions. The speed distributions derived from the ion images provide the rotational distribution of the co-fragment formed in conjunction with the particular level probed directly. Most of the 2+1 REMPI transitions used to acquire the ion images directly probe HCl products in v = 1, J levels and the speed distributions directly provide the state-correlated v = 0, J distributions. The bulk of the HCl(v = 1) rotational population distribution, $P(J_1)$, can be derived from the 2+1 REMPI spectra shown in Figure 4-2 and Figure 4-3. The V–X(16,1) spectrum can be used to determine the relative populations in the J_1 = 7–9 levels while the F–X(0,1) transition provides relative populations in J_1 = 8–14. Lines in the F–X(0,1) P branch and V–X(16,1) Q branch spectra were fit to Gaussian functions to determine the peak areas. The REMPI signal intensities were subsequently corrected for the relevant rotational line strength factors, calculated by PGOPHER, and any contributions from underlying or unresolved REMPI transitions. The relative F–X(0,1) and V–X(16,1) transition strengths are unknown, but the presence of common levels in each spectral region can be used to scale the populations derived from each spectrum. Transitions originating in J_1 = 9 are used following $2\nu_1$ excitation and J_1 = 8 following $2\nu_2$ excitation; in both cases the scaling factors are consistent. Populations corresponding to the levels probed on lines B and F, identified as transitions to an unknown

$^1\Sigma^+$ state and originating in $J_0 = 11$ and $J_0 = 13$, respectively, have been derived using Q branch $^1\Sigma^+$ line strengths factors.

The correlated product pair distributions obtained following excitation to $2\nu_1$ and $2\nu_2$ are shown as intensity plots in Figure 4-6 and Figure 4-7, respectively. In both plots, the distributions form bands that extend from high-J_1 and low-J_0 levels in the bottom right corner to low-J_1 and high-J_0 levels in the top left corner. Between these two limits, population is also measured in pairs comprising intermediate values of J_0 and J_1. The absence of population below the band indicates that pairs comprising lower degrees of rotational excitation (and consequently higher translational energy) are strongly disfavored. The region in the upper

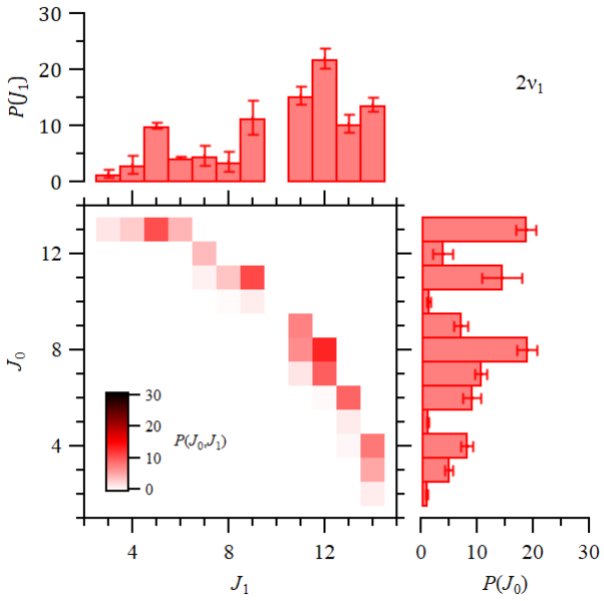

Figure 4-6 Correlated HCl(J_0, J_1) product pair population distributions after excitation of $(HCl)_2$ on the $2\nu_1$ band. The total population has been normalized to 100. Horizontal and vertical bars show the total rotational population distributions in $v = 0$ and $v = 1$, $P(J_0)$ and $P(J_1)$, respectively, after summation over all co-fragment levels. Error bars represent 1σ uncertainties.

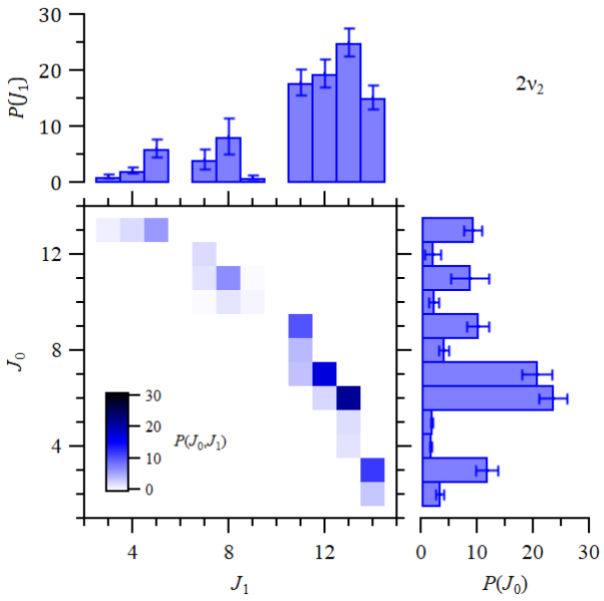

Figure 4-7 Correlated HCl(J_0, J_1) product pair population distributions after excitation of $(HCl)_2$ on the $2\nu_2$ band. The total population has been normalized to 100. Horizontal and vertical bars show the total rotational population distributions in v = 0 and v = 1, $P(J_0)$ and $P(J_1)$, respectively, after summation over all co-fragment levels. Error bars represent 1σ uncertainties.

right corner comprises energetically inaccessible product pairs. Predissociation of $2\nu_2$ results in a slight propensity for (low-J_0, high-J_1) pairs, as indicated by generally higher intensity in the bottom right corner, while $2\nu_1$ predissociation distributes population more evenly across the band. Summing horizontally or vertically gives the overall rotational distributions in v=0, $P(J_0)$ or v = 1, P(J_1) distributions, which are shown as bar charts. For $2\nu_1$, weak even/odd J alternation is observed for J_1 = 10–14. The somewhat broader distribution of populated J_0 and J_1 levels following excitation of the $2\nu_1$ mode is also seen in the bar charts. In contrast a narrower distribution is seen for $2\nu_2$, with fragments predominantly populating J_0 = 6, 7 and J_1 > 10 levels.

4.4.4 Time dependence

Vibrational predissociation lifetimes, τ_{VP}, of the $2\nu_1$ and $2\nu_2$ states have been determined by measuring dependence of the HCl REMPI signal as a function of time delay between the IR pump and UV probe pulses. The time resolution of the measurements is limited by the temporal profile of the laser pulses, which have FWHM of ~6 ns. Transient ion yields were measured for various background free transitions in the E–X (0,0) region. The resulting time-dependent profiles were fit to the product of a single exponential rise and Heaviside step function, convoluted with a Gaussian function to mimic the instrument resolution.[43] Excitation of the acceptor HCl stretch overtone $2\nu_1$ led to a time dependence – the vibrational predissociation lifetime is τ_{VP} = 13±1 ns (1σ uncertainty). In contrast, predissociation lifetime after excitation of the donor stretch $2\nu_2$ was shorter than the instrument resolution, leading to an upper limit of τ_{VP} < 6 ns. No discernible *J* dependence was observed.

4.5 Discussion

Overtone spectrum of $(HCl)_2$. The overtone region of $(HCl)_2$ has been the subject of far less attention than the fundamental, with only a cavity ring-down spectrum of Wittig and co-workers appearing in the literature.[31] Jensen *et al*.[44] performed calculations on a six-dimensional *ab initio* potential energy surface to predict band origins of 5643 cm^{-1} and 5609 cm^{-1} for the $2\nu_1$ and $2\nu_2$ modes, respectively, which are in reasonably good agreement with the experimental $2\nu_1$ and $2\nu_2$ band origins of 5656 cm^{-1} and 5697 cm^{-1}. The calculated transition dipole moments suggest the free stretch overtone, $2\nu_1$, is approximately three times stronger than the donor stretch overtone, $2\nu_2$.[44] The observed intensities in the IR

action spectrum shown in Figure 4-1 cannot be directly compared without taking into account the HCl product state distributions resulting from the vibrational predissociation. The IR action spectrum was obtained probing J_1 = 12 and analysis of the population distributions (Figure 4-6 and Figure 4-7) show that the J_1 = 12 populations are the same within error after excitation of $2\nu_1$ and $2\nu_2$ (22±2 and 19±3, respectively, expressed as percentages). Consequently, the factor of two difference in the $2\nu_1$ and $2\nu_2$ integrated peak areas can be related directly to the relative transition strengths, in good agreement with the calculations.

The highest frequency features in the IR action spectrum at 5671 cm^{-1} and 5683 cm^{-1} are assigned to the K_a = 0←0 and K_a = 1←0 sub-bands of the $2\nu_2+\nu_4$ combination band, based on frequencies reported by Fárník *et al.*[16] Four $\nu_2+\nu_n$ combination bands involving low frequency intermolecular modes of $(HCl)_2$ (plus isotopomeric equivalents) were observed in high-resolution spectra and assigned to the van der Waals stretch (ν_4) and geared bend motion (ν_5). Three out of four of the assignments were surprisingly based on transitions originating from the upper tunneling level (B^+), which lies ~15 cm^{-1} above the lower (A^+) level. Using a 3D quantum mechanical model, the authors calculated transition moments from the lower A^+ tunneling level to be 40 times weaker than corresponding transitions from the upper B^+ level, which was proposed to be a consequence of the extremely floppy nature of the dimer. In contrast, several of the equivalent combination bands were observed originating from both tunneling components for the more rigid HF dimer by Anderson *et al.,*[45] but the $\nu_2+\nu_4$ band was still only observed from the B^+ state. Interestingly, our $2\nu_2+\nu_4$ assignment only holds true if the transition originates from the lower tunneling state,

suggesting that the relative intensities of overtone transitions originating from the A^+ state are larger. Application of the model used by Fárník *et al.*[16] to predict vibrational transition moments may shed light on the effects that can arise from overtone excitation, although given the low spectral resolution of the current measurements, the effort seems unwarranted at present. Higher resolution spectroscopic measurements would certainly allow for definitive assignments of the additional features in the overtone region of the $(HCl)_2$ spectrum.

Revision of D_0. The bond dissociation energy of 395±7 cm^{-1} is ~40 cm^{-1} smaller than previously reported D_0 values. Pine and Howard[6] determined a value of D_0 = 431±22 cm^{-1} from measured temperature-dependent IR line-strengths. The value was later refined by Valentini and coworkers,[26,27] who used position-sensitive translational spectroscopy (POSTS) to directly measure the translational energy of HCl product pairs to obtain a more precise value of D_0 = 439±1 cm^{-1}. The POSTS method utilizes counterpropagating pulsed lasers (pump + probe) that are spatially separated by a known distance and fixed time delay.[46] By physically scanning the distance between the pump and probe beams over hundreds of μm, the fragment spatial distributions and ultimately recoil velocities are measured. Product translational energies are obtained from simulations of the POSTS data that require precise knowledge of the time delay and spatial coordinates. While temporal jitter of the laser beams and uncertainties in spatial alignment can lead to errors, the temporal jitter of < 1 ns and a claimed spatial uncertainty of ±2 μm would give rise to a small uncertainty in the speed of ~1 m s^{-1}, corresponding to the shortest time delay (0.8 μs) and smallest position (300 μm) reported by the authors. As in the velocity-map imaging

measurements, the experimental observable in POSTS is the recoil speed distribution. In the current measurements, D_0 is determined directly from the radii of features in the ion images and does not require precise knowledge of the time delay or spatial overlap between the two laser beams. As discussed earlier, potential sources of error in the VMI experiments arise from uncertainty in the calibration factor or the IR photon energy, neither of which are significant. The origin of the discrepancy is unclear and somewhat perplexing.

Correlated product-pair distributions. The ion imaging measurements identify 22 distinct product pairs resulting from $2\nu_1$ predissociation and 20 arising from predissociation of $2\nu_2$. In all of the pairs identified, one of the HCl monomers retains one quantum of vibrational excitation. In contrast, earlier experiments by Wittig and co-workers suggested the surprising result that vibrational predissociation of overtone excited $(HCl)_2$ led to the formation of highly rotationally excited HCl(J_0 = 20,21).[35] Formation of $J_0 \geq 15$ products requires that both HCl monomers must be in $v = 0$ by energy conservation (the maximum rotational level accessible for vibrationally excited HCl products is $J_1 = 14$). We find no conclusive evidence to support (J_0, J_0) pair formation following predissociation of the HCl dimer. While peak C in the 2+1 REMPI spectrum shown in Figure 4-2 was assigned to J_1 = 12, we note that the term value for this level is very close to that for J_0 = 20 (4480 cm^{-1} and 4489 cm^{-1}). Within the precision of our measurements, the latter assignment would be equally plausible, with the speed distribution indicating that the co-fragments are produced in the J_0 = 6, 7, and 8 levels. However, the relative magnitudes of the J_0 = 6, 7, 8 features are the same as those observed probing J_1 =12 on the known F–X(0,1) P(12) transition, and this remains our preferred assignment. Using REMPI to detect predissociation products directly

is a more straightforward approach than the earlier experiments, which detected H atoms produced by 193 nm photolysis of dimers, vibrationally excited dimers, and the monomer predissociation products.

The complete HCl(J_0, J_1) product pair correlation maps for $2\nu_1$ and $2\nu_2$ predissociation shown in Figure 4-6 and Figure 4-7 have qualitatively the same shape, with a noted propensity to minimize the translational energy. The propensity for low E_T is more apparent in Figure 4-8 where $P(J_0, J_1)$ is plotted as a function of E_T, as is the distinct mode-dependent product pair population distributions. For all product pairs, the fraction of the available energy partitioned into translation, $f_T = E_T/E_{AVL}$, is less than 0.12 and typically much smaller. In contrast, similar experiments exploring predissociation following excitation of ν_1 and ν_2 by

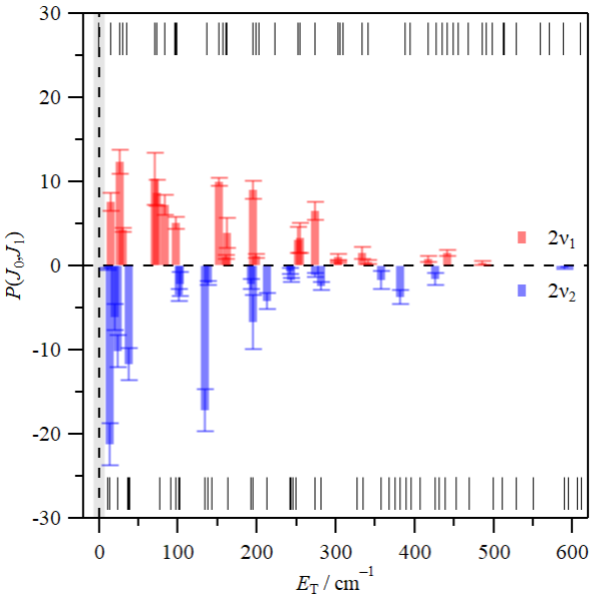

Figure 4-8 HCl(J_0, J_1) product pairs resulting from vibrational predissociation of $(HCl)_2$ after excitation on the $2\nu_1$ (red) and $2\nu_2$ (blue, inverted) bands plotted as a function of translational energy, E_T. Error bars represent 1σ uncertainties. Ladders indicate the expected E_T values for all possible HCl(J_0, J_1) product pairs.

Valentini and co-workers[25,26] found no mode dependence. The propensity for vibrational predissociation to result in product pairs with low E_T, and mode dependence can be quantified by a linear surprisal analysis. The surprisal, $I(E_T)$ characterizes the deviation from statistical behavior as a function of translational energy:

$$I(E_T) = -\ln\left[\frac{P(E_T)}{P°(E_T)}\right] = a + bE_T$$

where $P(E_T)$ is the experimental product state distribution and $P°(E_T)$ is the prior distribution. The prior distribution is calculated using

$$P°(E_T) \propto (2J_0 + 1)(2J_1 + 1)E_T^{1/2}$$

where $(2J_v+1)$ is the degeneracy of the J_0 or J_1 level. Figure 4-9 presents surprisal plots of the $2\nu_1$ and $2\nu_2$ distributions as a function of f_T. The data are reasonably linear and yield positive surprisal parameters of 50±5 ($2\nu_1$) and 40±8 ($2\nu_2$), confirming that the experimental product state distributions are highly non-statistical and show strong bias for energy disposal into rotational motion rather than translation. An equivalent analysis by Ni *et al.*[26] on HCl(J_0, J_0) distributions obtained following excitation in the fundamental region resulted in a surprisal parameter of 39±5 for both ν_1 and ν_2. The overtone predissociation results confirm that the dynamical bias against translation is equivalent to that observed in the fundamental region for excitation of the donor HCl stretch and even greater for the acceptor HCl stretch.

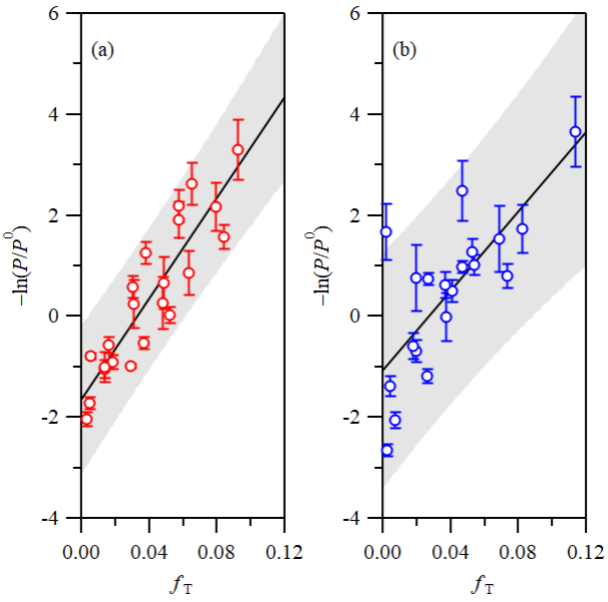

Figure 4-9 Linear surprisal plots for HCl(J_0, J_1) product pairs after excitation of the $2\nu_1$ (a, red) and $2\nu_2$ (b, blue) bands of $(HCl)_2$. Shaded regions represent 2σ prediction limits.

Further insight into the vibrational predissociation dynamics can be gained through simple models that are commonly used to describe the product rotational energy distributions. The probability of formation of $P(J_0, J_1)$ product pairs can be described in a similar manner using a simple momentum gap model as applied by Ni *et al.*:[26]

$$P(J_0, J_1) = \exp\left(-\mu v_{J_0,J_1}/a\right)$$

Here, μ is the reduced mass, v_{J_0,J_1} is the recoil velocity of the particular J_0, J_1 pair, and a is a normalization constant. Figure 4-10 presents a comparison of the experimental $P(J_0)$ and $P(J_1)$ distributions after $2\nu_1$ excitation along with the predictions of the momentum gap model. The agreement is remarkably good, with the relative populations in the majority of rotational levels being reasonably well described by the model. Figure 4-11 shows the

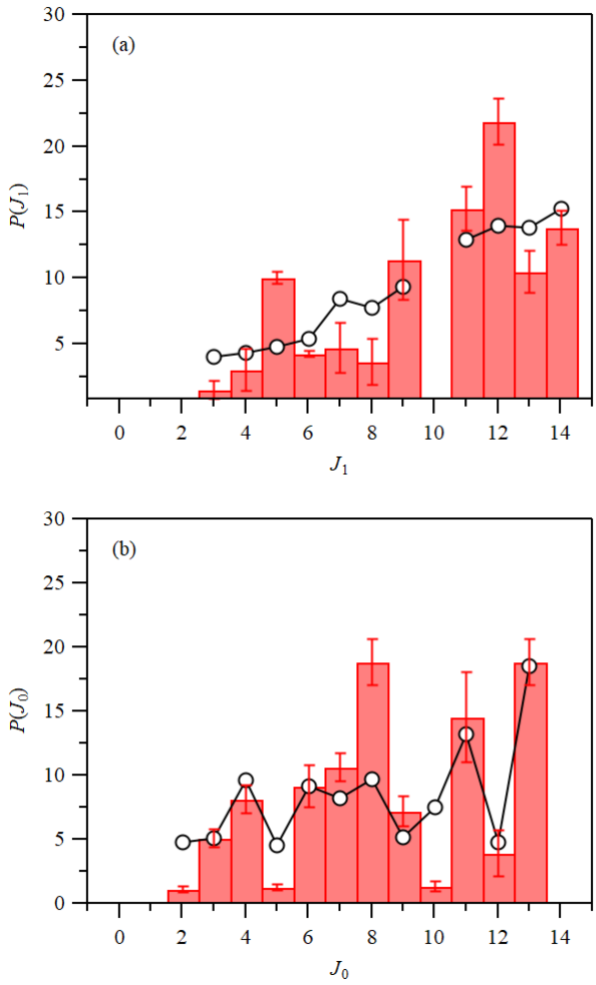

Figure 4-10 Comparison of predictions of the momentum gap model,[50] (black circles) with measured HCl product rotational distributions $P(J_v)$ for (a) $v = 1$ and (b) $v = 0$ (red bars) following predissociation of $(HCl)_2$ via the $2\nu_1$ mode.

analogous experimental and predicted rotational distributions for $2\nu_2$ excitation. In this case, the experimental data appear to deviate more from the model, which generally predicts broader $P(J_0)$ and $P(J_1)$ distributions. The experimental distributions display a slightly greater bias towards forming high-J_1 with high rotational energy ($J_1 > 10$) and J_0 with low to moderate rotational energy. While the momentum gap model appears to do a good job reproducing the observed product pair distributions, the agreement is somewhat superficial

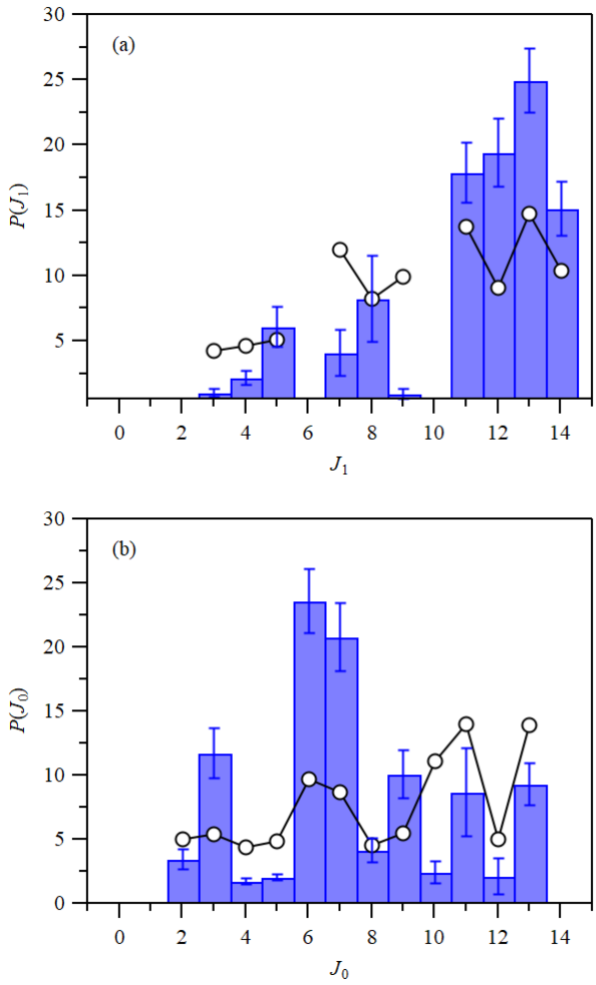

Figure 4-11 Comparison of predictions of the momentum gap model,[50] (black circles) with experimental HCl product rotational distributions $P(J_v)$ for (a) v = 1 and (b) v = 0 (blue bars) following predissociation of $(HCl)_2$ via the $2\nu_2$ mode.

as only (J_0,J_1) pairs that were observed experimentally are included in Figure 4-10 and Figure 4-11. As can be seen in Figure 4-8, many accessible product pairs that would result in modest E_T are not observed; the momentum gap law predicts significant population in such levels. Unsurprisingly for such a simple model, it lacks predictive power.

The differences observed in the rotational distributions following excitation of the overtone

versus fundamental modes may in part be due to the structure of the HCl dimer in the vibrationally excited levels. Large amplitude geared bending motion leads to interconversion of the donor and acceptor HCl molecules. The resulting tunneling splitting is quenched by vibrational excitation of either HCl stretching modes, decreasing from 15.5 cm^{-1} to 3.3 cm^{-1}.[12] Overtone excitation results in an even smaller tunneling splitting with values less than the 0.1 cm^{-1} uncertainty in the measurement,[31] indicating that interconversion is effectively quenched. The large amplitude geared bending motion is reduced and effectively causes the dimer structure to become more rigid, suggesting the HCl monomer likely to be vibrationally excited ($v = 1$) is the donor for $2\nu_2$ and the acceptor for $2\nu_1$. The tunneling splitting for overtone excited $(HCl)_2$ is comparable to the value of 0.22 cm^{-1} observed for $(HF)_2$ excited in the fundamental,[30] suggesting both dimers are similarly rigid and may exhibit similar vibrational predissociation dynamics.

Bohac *et al*. have measured the product pair distributions resulting from vibrational predissociation of $(HF)_2$ excited on the fundamental donor and acceptor HF stretch bands.[29] The resulting product pair distributions are highly non-statistical, favoring small E_T, but cannot be described by a linear surprisal analysis or the momentum gap model. The HF(J_0,J_0) distributions showed a propensity for formation of low-J_0–high-J_0 pairs while $J_0 \approx J_0$ pairs were suppressed. This observation was interpreted as being a result of impulsive dissociation in which the proton donor HF "pushes off" its partner. In this model of the dynamics, the donor HF experiences a larger torque and becomes the high-J_0 partner, while the acceptor HF experiences a small torque and becomes the low-J_0 fragment. Consequently, the rigid geometry restricts the distribution of product pairs. The impulsive description of

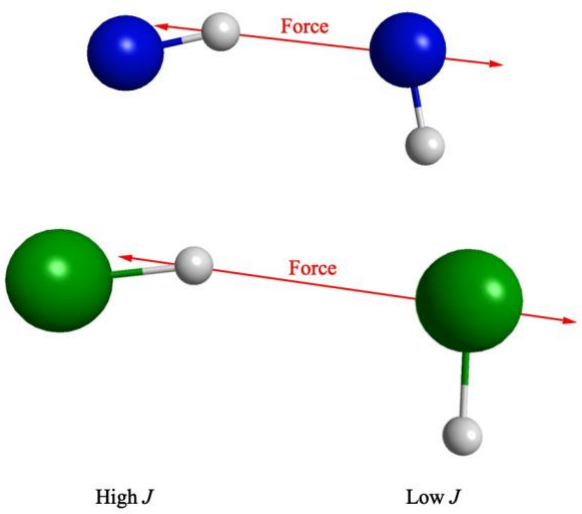

Figure 4-12 Equilibrium structures of $(HF)_2$ and $(HCl)_2$ and the impulsive forces acting on the fragments that would lead to correlated high-*J*–low-*J* rotational distributions. Geometries have been optimized at the MP2/cc-pVDZ level of theory.

the dynamics is illustrated in Figure 4-12, which shows the similarity of the $(HF)_2$ and $(HCl)_2$ equilibrium geometries, as optimized at the MP2/cc-pVDZ level of theory. Key geometrical parameters for the dimers are compiled in Table 4.1 for reference. This impulsive picture

Table 4.1 Geometries of the HX (X=Cl, F) dimers optimized at the MP2/cc-VDZ level of theory.

parameter	$(HCl)_2$	$(HF)_2$
R_{X-X} / Å	3.90	2.68
R_{H-X} / Å	1.29	0.92
$\angle_{HXX}$ / °	9.2	11.9
$\angle_{XXH}$ / °	90.0	99.7

cannot be used to describe the fundamental predissociation dynamics of $(HCl)_2$ due to rapid interconversion between the HCl monomer units prior to dissociation, resulting in a weaker propensity to form low-J_0–high-J_0 pairs and a lack of mode dependence.

To explore the propensity for formation of high-J–low-J product pairs, the populations are plotted against ΔJ_{pair}, the absolute difference between the rotational levels comprising the pair, in Figure 4-13 for the rotational distributions of $(HCl)_2$ and $(HF)_2$ (overtone and fundamental excitation, respectively). The $(HF)_2$ data are adapted from Bohac *et al.*,[29] and averaged over the rotational states associated with the ν_1 and ν_2 modes that were resolved in that study. A linear correlation analysis confirms a statistically significant (at the $\alpha = 0.05$

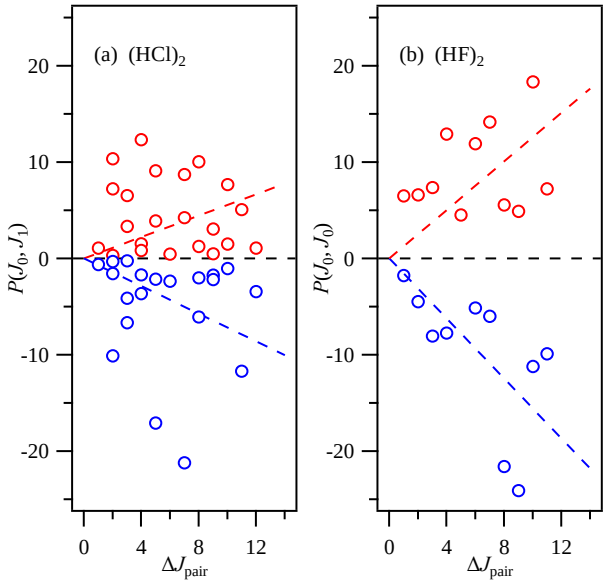

Figure 4-13 (a) Correlated HCl(J_0, J_1) product pair distributions plotted as a function of $\Delta J_{pair} = |J_1 - J_0|$ resulting from vibrational excitation of the (a) $2\nu_1$ (red) and $2\nu_2$ (blue, inverted) overtones of $(HCl)_2$. (b) Analogous HF(J_0, J_0) product pair distributions following excitation of the ν_1 (red) and ν_2 (blue, inverted) fundamentals of $(HF)_2$.[29] Dashed lines indicate linear fits to the data.

level) correlation between the population of given HF(J_0, J_0) pair and ΔJ_{pair}, with r values of 0.25 and 0.61 for ν_1 and ν_2 predissociation, respectively. Weak/moderate correlation mode dependence is observed for $(HF)_2$ following fundamental excitation. The dynamics associated with vibrational predissociation of $(HF)_2$ are somewhat mode dependent, with initial excitation of the ν_2 level leading to a stronger propensity for the formation of high-J_0–low-J_0 pairs than ν_1 excitation. The same linear correlation analysis of the $(HCl)_2$ predissociation data results in small positive and negative values of r (+0.13 and –0.13), suggesting a weak correlation/anticorrelation for $(HCl)_2$ predissociation via $2\nu_2$ and $2\nu_1$, respectively. However, performing the same statistical analysis, an analogous t-test suggests that these correlations are not statistically significant at the $\alpha = 0.05$ level with the available sample sizes of n =22 or 20. The statistical parameters are compiled in Table 4.2.

Table 4.2 Correlation parameters (r) and sample sizes (n) for the experimental data shown in Figure 4-13. Critical values of t ($t_{critical}$) were determined using the degrees of freedom (n–2) and reported at the $\alpha = 0.05$ level.[49]

	$(HCl)_2$		**$(HF)_2$**	
	$2\nu_1$	$2\nu_2$	ν_1	ν_2
r	-0.130	0.131	0.253	0.608
n	22	20	11	10
$t_{critical}$	±0.423	±0.444	±0.602	±0.632

The difference in dynamics between the HCl and HF dimers is surprising, since the tunneling constants suggest both dimers are rigid when $(HCl)_2$ is excited on the overtone bands. It is

not clear based on our results what role the rigidity of $(HCl)_2$ plays in the overtone predissociation dynamics.

From high-resolution spectroscopy studies,[47,48] it has been established through linewidth analysis that predissociation occurs at a much faster rate for vibration of the donor hydrogen than for the free HCl stretch due to its stronger coupling to the intermolecular van der Waals dissociation coordinate. This is further confirmed by the longer predissociation lifetime measured for $2\nu_1$ than for $2\nu_2$, with our measured overtone lifetimes of $\tau_{VP}(2\nu_1)$ = 13±1 ns and $\tau_{VP}(2\nu_2)$ < 6 ns being broadly comparable to the ν_1 and ν_2 lifetimes of $(HF)_2$ reported as 17±1 and 0.48±0.05 ns, respectively.[30] The $(HCl)_2$ predissociation lifetimes are substantially shorter for overtone excitation than for fundamental excitation, with $\tau_{VP}(\nu_1)$ ≥100 ns and $\tau_{VP}(\nu_2)$ = 31(7) ns.[12] This is consistent with observations made for $(HF)_2$, with overtone predissociation lifetimes being almost an order of magnitude shorter compared to lifetimes resulting from fundamental excitation.[30]

4.6 Conclusion

The vibrational predissociation dynamics of the HCl dimer after HCl stretch overtone excitation has been studied using velocity-map ion imaging. Low resolution IR action spectra of the HCl stretch overtone region show the acceptor ($2\nu_1$) and donor ($2\nu_2$) HCl stretch overtones, and a combination band involving the intermolecular van der Waals stretch mode ($2\nu_2+\nu_4$). 2+1 REMPI spectroscopy was used to detect HCl(v = 1, J) predissociation products via the $V^1\Sigma^+$–$X^1\Sigma^+$(16,1) and $F^1\Delta_2$–$X^1\Sigma^+$(0,1) transitions and HCl(v = 0, J) levels detected via an unidentified $^1\Sigma^+$ state, following IR excitation of both $2\nu_1$ and $2\nu_2$. Fragment speed

distributions derived from ion images were used to obtain correlated product pair distributions, $P(J_0, J_1)$; all product pairs identified comprise one vibrationally excited and one vibrational ground state HCl molecule. The measurements support a dimer dissociation energy of D_0 = 397±7 cm^{-1}, which is smaller than previously reported values. Detailed analysis of the pair-correlated rotational distributions suggests that the predissociation dynamics are vibrational mode-dependent. A strong propensity to minimize the translational energy release accompanies overtone predissociation, with f_T < 0.12 for all detected product pairs. The momentum gap model better predicts the HCl product rotational distributions in v =0 and v = 1 resulting from predissociation of $2\nu_2$ than $2\nu_1$. Mode specificity appears to be characteristic of overtone excitation and is distinct from the mode-independent predissociation dynamics observed following fundamental excitation of $(HCl)_2$.

4.7 Acknowledgements

This material is based upon work supported by the National Science Foundation under Grant No. CHE-1566064. Acknowledgment is made to the Donors of the American Chemical Society Petroleum Research Fund for support of this research.

4.8 References

1 P. E. S. Wormer and A. van der Avoird, Intermolecular Potentials, Internal Motions, and Spectra of van der Waals and Hydrogen-Bonded Complexes, *Chem. Rev.*, 2000, **100**, 4109–4144.

2 L. Oudejans and R. E. Miller, Photofragment Translational Spectroscopy of Weakly Bound Complexes: Probing the Interfragment Correlated Final State Distributions, *Annu. Rev. Phys. Chem.*, 2001, **52**, 607.

3 A. K. Samanta, Y. Wang, J. S. Mancini, J. M. Bowman and H. Reisler, Energetics and Predissociation Dynamics of Small Water, HCl, and Mixed HCl–Water Clusters, *Chem. Rev.*, 2016, **116**, 4913–4936.

4 H. Reisler, Photofragment Spectroscopy and Predissociation Dynamics of Weakly Bound Molecules, *Annual Review of Physical Chemistry*, 2009, **60**, 39–59.

5 N. Ohashi and A. S. Pine, High resolution spectrum of the HCl dimer, *J. Chem. Phys.*, 1984, **81**, 73–84.

6 A. S. Pine and B. J. Howard, Hydrogen bond energies of the HF and HCl dimers from absolute infrared intensities, *J. Chem. Phys.*, 1986, **84**, 590–596.

7 G. A. Blake, K. L. Busarow, R. C. Cohen, K. B. Laughlin, Y. T. Lee and R. J. Saykally, Tunable far-infrared laser spectroscopy of hydrogen bonds: The K_a =0(u)→1(g) rotation–tunneling spectrum of the HCl dimer, *J. Chem. Phys.*, 1988, **89**, 6577–6587.

8 G. A. Blake and R. E. Bumgarner, Direct measurement of the HCl dimer tunneling rate and Cl isotope dependence by far-infrared laser sideband spectroscopy of planar supersonic jets, *J. Chem. Phys.*, 1989, **91**, 7300–7301.

9 N. Moazzen-Ahmadi, A. R. W. McKellar and J. W. C. Johns, The far-infrared spectrum of the HCl dimer, *J. Mol. Spectrosc.*, 1989, **138**, 282–301.

10 N. Moazzen-Ahmadi, A. R. W. McKellar and J. W. C. Jonhs, Far-infrared observations of rotation-tunneling and torsional transitions in the HCl dimer, *Chem. Phys. Lett.*, 1988, **151**, 318–322.

11 A. Furlan, S. Wülfert and S. Leutwyler, Cars spectra of the HCl dimer in supersonic jets, *Chem. Phys. Lett.*, 1988, **153**, 291–295.

12 M. D. Schuder, C. M. Lovejoy, R. Lascola and D. J. Nesbitt, High resolution, jet-cooled infrared spectroscopy of $(HCl)_2$: Analysis of ν_1 and ν_2 HCl stretching fundamentals, interconversion tunneling, and mode-specific predissociation lifetimes, *J. Chem. Phys.*, 1993, **99**, 4346–4362.

13 M. D. Schuder and D. J. Nesbitt, High resolution near infrared spectroscopy of HCl–DCl and DCl–HCl: Relative binding energies, isomer interconversion rates, and mode specific vibrational predissociation, *J. Chem. Phys.*, 1994, **100**, 7250–7267.

14 M. D. Schuder, C. M. Lovejoy, D. D. Nelson and D. J. Nesbitt, Symmetry breaking in HCl and DCl dimers: A direct near-infrared measurement of interconversion tunneling rates, *J. Chem. Phys.*, 1989, **91**, 4418–4419.

15 M. Fárník, S. Davis and D. J. Nesbitt, Probing hydrogen bond potential surfaces for out-of-plane geometries: Near-infrared combination band torsional (ν_6) spectroscopy in $(HCl)_2$, *J. Chem. Phys.*, 2003, **118**, 10137–10148.

16 M. Fárník, S. Davis, M. D. Schuder and D. J. Nesbitt, Probing potential surfaces for hydrogen bonding: Near-infrared combination band spectroscopy of van der Waals stretch (ν_4) and geared bend (ν_5) vibrations in $(HCl)_2$, *J. Chem. Phys.*, 2002, **116**, 6132–6145.
17 M. J. Elrod and R. J. Saykally, Determination of the intermolecular potential energy surface for $(HCl)_2$ from vibration–rotation–tunneling spectra, *J. Chem. Phys.*, 1995, **103**, 933–949.
18 M. J. Elrod and R. J. Saykally, Vibration–rotation–tunneling dynamics calculations for the four-dimensional $(HCl)_2$ system: A test of approximate models, *J. Chem. Phys.*, 1995, **103**, 921–932.
19 Y. Qiu and Z. Bačić, Exact six-dimensional quantum calculations of the rovibrational levels of $(HCl)_2$, *J. Chem. Phys.*, 1997, **106**, 2158–2170.
20 Y. Qiu, J. Z. H. Zhang and Z. Bačić, Six-dimensional quantum calculations of vibration-rotation-tunneling levels of ν1 and ν2 HCl-stretching excited (HCl)2, *J. Chem. Phys.*, 1998, **108**, 4804–4816.
21 P. R. Bunker, V. C. Epa, P. Jensen and A. Karpfen, An analytical ab initio potential surface and the calculated tunneling energies for the HCl dimer, *J. Mol. Spectrosc.*, 1991, **146**, 200–219.
22 A. Karpfen, P. R. Bunker and P. Jensen, An ab initio study of the hydrogen chloride dimer: The potential energy surface and the characterization of the stationary points, *Chem. Phys.*, 1991, **149**, 299–309.
23 P. Jensen, M. D. Marshall, P. R. Bunker and A. Karpfen, An ab initio close-coupling calculation of the lower vibrational energies of the HCl dimer, *Chem. Phys. Lett.*, 1991, **180**, 594–600.
24 S. C. Althorpe, D. C. Clary and P. R. Bunker, Calculation of the far-infrared spectra for $(HF)_2$, $(HCl)_2$ and $(HBr)_2$, *Chem. Phys. Lett.*, 1991, **187**, 345–353.
25 J. Serafin, H. Ni and J. J. Valentini, Direct, spectroscopic measurement of the rotational state distribution of HCl fragments from the vibrational predissociation of ν_2=1 $(HCl)_2$ produced by stimulated Raman excitation, *J. Chem. Phys.*, 1994, **100**, 2385–2387.
26 H. Ni, J. M. Serafin and J. J. Valentini, Dynamics of the vibrational predissociation of HCl dimer, *J. Chem. Phys.*, 2000, **113**, 3055–3066.
27 H. Ni, J. M. Serafin and J. J. Valentini, State-resolved, three-dimensional product recoil velocity spectroscopy, *J. Chem. Phys.*, 1996, **104**, 2259–2270.
28 G. W. M. Vissers, L. Oudejans, R. E. Miller, G. C. Groenenboom and A. van der Avoird, Vibrational predissociation in the HCl dimer, *J. Chem. Phys.*, 2004, **120**, 9487–9498.
29 E. J. Bohac, M. D. Marshall and R. E. Miller, Initial state effects in the vibrational predissociation of hydrogen fluoride dimer, *J. Chem. Phys.*, 1992, **96**, 6681–6695.
30 M. A. Suhm, J. T. Farrell, A. McIlroy and D. J. Nesbitt, High resolution 1.3 μm overtone spectroscopy of HF dimer in a slit jet: K_a=0←0 and K_a=1←0 subbands of ν_{acc}=2←0, *J. Chem. Phys.*, 1992, **97**, 5341–5354.
31 K. Liu, M. Dulligan, I. Bezel, A. Kolessov and C. Wittig, Quenching of interconversion tunneling: The free HCl stretch first overtone of $(HCl)_2$, *J. Chem. Phys.*, 1998, **108**, 9614–9616.

32 H. Chang and W. Klemperer, The vibrational second overtones of HF dimer: A quartet, *J. Chem. Phys.*, 1994, **100**, 1–14.
33 H. Chang and W. Klemperer, State-specific vibrational predissociation and interconversion tunneling quenching at $3\nu_1$ and $3\nu_2$ of $(HF)_2$, *J. Chem. Phys.*, 1993, **98**, 9266–9278.
34 K. von Puttkamer and M. Quack, Vibrational spectra of $(HF)_2$, $(HF)_n$ and their D-isotopomers: Mode selective rearrangements and nonstatistical unimolecular decay, *Chem. Phys.*, 1989, **139**, 31–53.
35 K. Liu, A. Kolessov, J. W. Partin, I. Bezel and C. Wittig, Probing the Cl–HCl complex via bond-specific photodissociation of $(HCl)_2$, *Chem. Phys. Lett.*, 1999, **299**, 374–380.
36 C. A. Picconatto, H. Ni, A. Srivastava and J. J. Valentini, Quantum state distributions of HCl from the ultraviolet photodissociation of HCl dimer, *J. Chem. Phys.*, 2001, **114**, 7073–7080.
37 B. W. Toulson, J. P. Alaniz, J. G. Hill and C. Murray, Near-UV photodissociation dynamics of CH_2I_2, *Phys. Chem. Chem. Phys.*, 2016, **18**, 11091–11103.
38 G. M. Roberts, J. L. Nixon, J. Lecointre, E. Wrede and J. R. R. Verlet, Toward real-time charged-particle image reconstruction using polar onion-peeling, *Rev. Sci. Instrum.*, 2009, **80**, 053104.
39 *PGOPHER, a Program for Simulating Rotational Structure, C. M. Western, University of Bristol, http://pgopher.chm.bris.ac.uk*, PGOPHER, a Program for Simulating Rotational Structure, C. M. Western, University of Bristol, http://pgopher.chm.bris.ac.uk.
40 D. S. Green, G. A. Bickel and S. C. Wallace, (2 + 1) Resonance enhanced multiphoton ionization of hydrogen chloride in a pulsed supersonic jet: Vacuum wavenumbers of rotational lines with detailed band analysis for excited electronic states of $H^{35}Cl$, *J. Mol. Spectrosc.*, 1991, **150**, 388–469.
41 D. H. Rank, B. S. Rao and T. A. Wiggins, Molecular constants of HCl^{35}, *J. Mol. Spectrosc.*, 1965, **17**, 122–130.
42 D. U. Webb and N. K. Rao, Vibration rotation bands of heated hydrogen halides, *J. Mol. Spectrosc.*, 1968, **28**, 121–124.
43 B. W. Toulson, D. A. Fishman and C. Murray, Photodissociation dynamics of acetone studied by time-resolved ion imaging and photofragment excitation spectroscopy, *Phys. Chem. Chem. Phys.*, 2018, **20**, 2457–2469.
44 P. Jensen, P. R. Bunker, V. C. Epa and A. Karpfen, An ab initio calculation of the fundamental and overtone HCl stretching vibrations for the HCl dimer, *J. Mol. Spectrosc.*, 1992, **151**, 384–395.
45 D. T. Anderson, S. Davis and D. J. Nesbitt, Probing hydrogen bond potentials via combination band spectroscopy: A near infrared study of the geared bend/van der Waals stretch intermolecular modes in $(HF)_2$, *The Journal of Chemical Physics*, 1996, **104**, 6225–6243.
46 H. Ni, J. M. Serafin and J. J. Valentini, A simple method for measurement of the full three-dimensional velocity distribution of photofragments and reaction products, *Chemical Physics Letters*, 1995, **244**, 207–212.
47 D. J. Nesbitt, High-resolution infrared spectroscopy of weakly bound molecular complexes, *Chem. Rev.*, 1988, **88**, 843–870.

48 D. J. Nesbitt, High-Resolution, Direct Infrared Laser Absorption Spectroscopy in Slit Supersonic Jets: Intermolecular Forces and Unimolecular Vibrational Dynamics in Clusters, *Annu. Rev. Phys. Chem.*, 1994, **45**, 367–399.

5 Appendix: Wavelength Calibration using Photoacoustic Spectroscopy

Photoacoustic spectroscopy, based on the photoacoustic effect, has long been used as a way for detection of trace gases and sample characterization.[1–5] This technique requires a closed cell, a pulsed light source, a light-absorbing sample, and an acoustic detector (usually a microphone). The pulsed light, when incident upon the sample, is absorbed. The excited molecules undergo non-radiative relaxation processes, such as collision deactivation, leading to periodic warming of the sample. Thermal expansion of the emitted heat produces localized pressure waves, which in turn can be measured as an acoustic wave.[2]

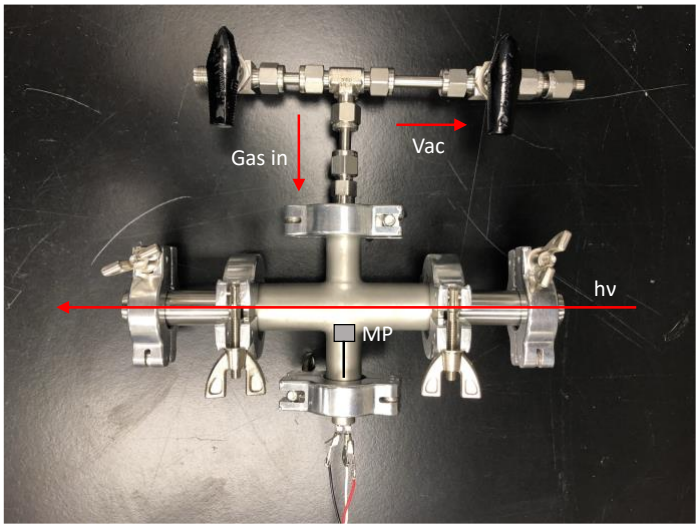

Figure 5-1 Photoacoustic setup using a microphone (MP).

A picture of the photoacoustic cell used for initial calibration of the IR laser is shown in Figure 5-1. The pulsed laser beam passes through two sapphire windows along the main axis of the cell with a pathlength of 18 cm. A small microphone (Knowles, EK-23132-000) is placed near to the beam path.

Figure 5-2 displays a schematic of the electronic connections used for powering the microphone outside of the cell. The circuit comprises a 9 V battery, 100 µF capacitor (C_1, for smoothing out discontinuities in the power supply), 0.1 µF ceramic monolithic capacitor (C_2, for limiting radio frequency interference), and a 100 kΩ potentiometer. The potentiometer is adjusted so that V_{in} matches the voltage rating of the microphone (1.3 V). The output signal of the microphone is connected to an oscilloscope using a BNC cable.

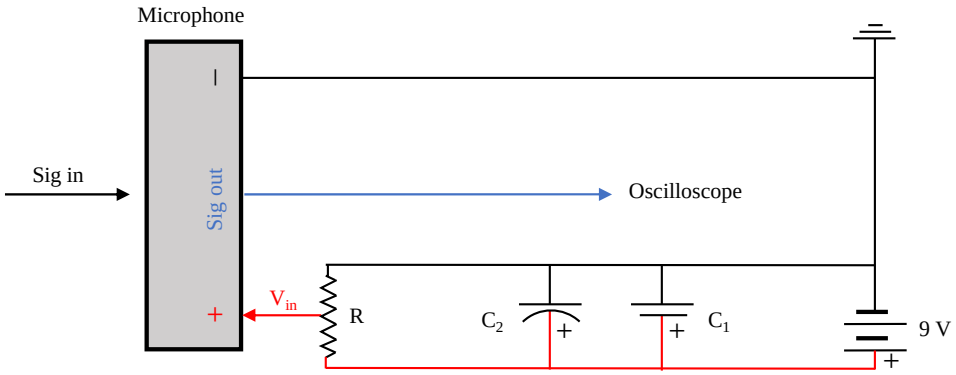

Figure 5-2 Microphone circuit schematic.

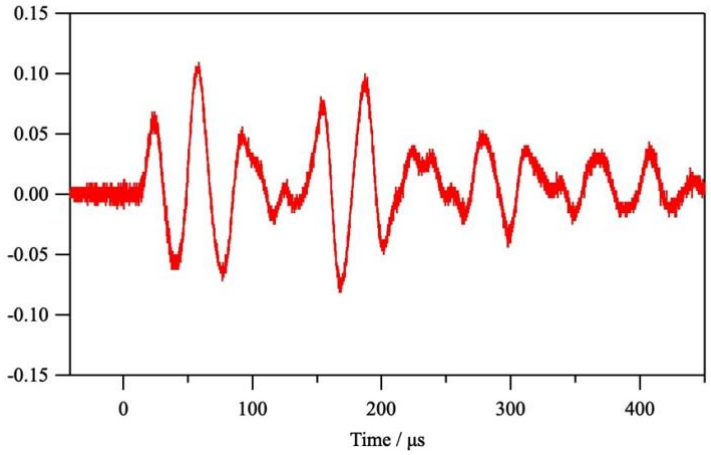

Figure 5-3 Raw photoacoustic signal following IR excitation of H_2O.

An example of the microphone output signal following IR excitation of H_2O vapor is shown in Figure 5-3. The signal is proportional to the absorption cross section of the molecule and a spectrum can be obtained by summing over both positive and negative components of the signal (I):

$$\int \sqrt{I^2}\, d\lambda$$

A sample IR absorption spectrum of H_2O vapor is shown in Figure 5-4. The spectrum was obtained using an unfocused IR laser beam (Continuum Mirage 3000) with pulse energies ~5 mJ and a spectral bandwidth of ~4 cm^{-1}. No signal amplification was needed before the oscilloscope. The photoacoustic cell was initially evacuated to ~10^{-2} torr and upon exposure to a room temperature sample of liquid H_2O, the resulting pressure inside the cell increased to ~23 torr.

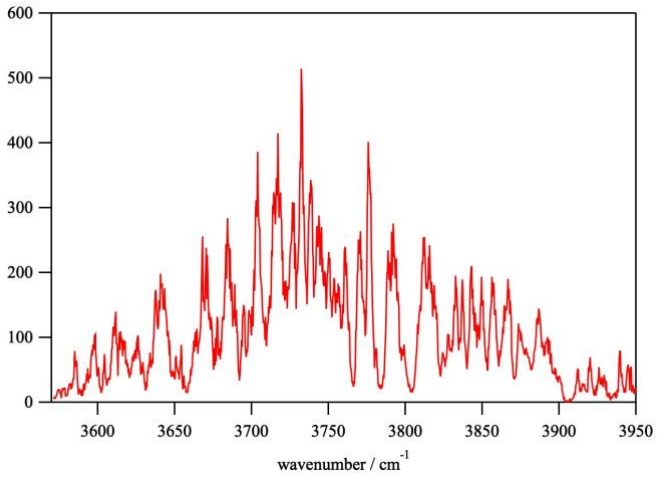

Figure 5-4 Calibrated IR absorption spectrum of room temperature H_2O vapor.

References

1 C. Haisch, Photoacoustic spectroscopy for analytical measurements, *Meas. Sci. Technol.*, 2011, **23**, 012001.

2 G. A. West, Photoacoustic spectroscopy, *Review of Scientific Instruments*, 1983, **54**, 797.

3 J. Hinderling, M. W. Sigrist and F. K. Kneubühl, Laser-photoacoustic spectroscopy of water-vapor continuum and line absorption in the 8 to 14 μm atmospheric window, *Infrared Physics*, 1987, **27**, 63–120.

4 A. Miklós, P. Hess and Z. Bozóki, Application of acoustic resonators in photoacoustic trace gas analysis and metrology, *Review of Scientific Instruments*, 2001, **72**, 1937–1955.

5 C. Haisch, P. Menzenbach, H. Bladt and R. Niessner, A Wide Spectral Range Photoacoustic Aerosol Absorption Spectrometer, *Anal. Chem.*, 2012, **84**, 8941–8945.